IMPACT-IONIZATION MASS SPECTROMETRY OF COSMIC DUST

Thesis by

Daniel E. Austin

Submitted in Partial Fulfillment of the Requirements for the Degree of

Doctor of Philosophy

California Institute of Technology

Pasadena, California

2003

(Defended November 5, 2002)

Acknowledgements

First of all, I thank Dave Dearden, Professor of Chemistry at Brigham Young University, and a former Caltech graduate student, for encouraging me to pursue graduate work at Caltech. The experiences I gained working with him, both as a research assistant and as a teaching assistant, proved invaluable during my stay here.

Numerous people at Caltech have contributed in some way to my research efforts. Foremost among these is my advisor, Jack Beauchamp, who successfully balances providing advice and supervision with the hands-off approach that is essential to developing creativity, resourcefulness, and drive in students. I also thank all the other Beauchamp group members who have helped me in so many ways: Dmitri Kossakovski, Sang-Won Lee, Jim Smith, Heather Cox, Ron Grimm, Ryan Julian, and Rob Hodyss. I joined Jack's group in part because of the very high caliber of students at that time. It seems I am leaving a group equally outstanding. There could be no finer collection of colleagues than this.

Minta Akin, an undergraduate Caltech student, has helped tremendously with the ice accelerator, and I thank her for all her work. Mike Roy, Guy Duremberg, and Ray Garcia, the chemistry department machinists, have been both helpful and patient with me as I've built numerous instrument parts. I hope I returned everything I borrowed from them. Thanks, gentlemen, for all your instruction and assistance. I also thank Priscilla Boon, the group secretary, and Dian Buchness, the graduate secretary, and the other support staff for taking care of so many small but necessary things over the years. I am also grateful for the many other people who have listened to me, told me what to

do, told me what not to do, reminded me of conferences, proofread papers, and put up with me in general.

Much of my work was done in collaboration with Tom Ahrens and his geophysics group. I am grateful to all of them, including Joe Atkins, Andy Shen, Ingrid Mann, Mike Long, and Sue Yamada.

A primary segment of my thesis research was conducted on the van de Graaff dust accelerator at Concordia College, Moorhead, Minnesota. While many other microparticle accelerators from the 1960's have long since been disassembled, the faculty at Concordia have carefully maintained this instrument in working condition. It is the only functional dust accelerator in the Western Hemisphere, and my research would have been much more complicated had it been necessary to go overseas for fast dust. I am grateful to Carl Bailey and Heidi Manning, both of the Concordia Physics faculty, for hosting my research visit, running the accelerator, and helping solve every problem that arose. I also thank Jim Farnsworth, an undergraduate physics student, who spent many days and evenings recording particle velocities in my lab notebook.

I am grateful to all who have contributed financially to my graduate work. NASA and NSF have supported the research. An NSF Graduate Research Fellowship and an ARCS Fellowship have contributed to my personal support.

Finally, I am eternally grateful for the greatest friends of all, my family. My grandfathers both attended Caltech; they and other relatives have been very supportive of all my efforts. My parents and sisters in particular have always encouraged me to do my best. I thank my wife, Lisa, who spent many nights putting the kids to bed alone

while I was having fun in the lab shooting lasers or small projectiles at things and calling it “work.”

Abstract

In situ characterization of cosmic dust grains typically involves impact-ionization time-of-flight mass spectrometry. Considering the performance and limitations of previous instruments, I designed and tested a novel, compact time-of-flight mass spectrometer for cosmic dust analysis. The instrument, Dustbuster, incorporates a large target area with a reflectron, simultaneously optimizing mass resolution, particle detection, and ion collection. Dust particles hit the 65-cm^2 target plate and are partially ionized by the impact. The resulting ions, with broad energy and angular distributions, are accelerated through the modified reflectron, focusing ions spatially and temporally to produce high-resolution spectra.

Initial performance tests of the Dustbuster used laser desorption ionization of embedded metal and mineral samples to simulate particle impacts. Mass resolution (mass/peakwidth) in these experiments ranged from 60 to 180, permitting resolution of isotopes. Subsequent experiments included hypervelocity microparticle impacts. Charged iron and copper microparticles, accelerated to 2-20 km/s in a 2 MV van de Graaff accelerator, impacted the Dustbuster. Mass resolution in these experiments ranged from 150 to 300 for iron and copper. Hydrogen, carbon, and oxygen ions appeared in many spectra. Field-induced emission of electrons immediately before impact is a possible cause of ion formation from species with high ionization potentials. The implications of this ionization effect are discussed in relation to interpretation of mass spectra from other *in situ* dust analyzers.

Another time-of-flight instrument, originally designed as an energy analyzer, shows promise as a high-resolution mass spectrometer for high-flux cosmic dust environments.

Ice is an important component of particulates ejected from comets and other icy bodies in the solar system. Due to limited experimental data on ice particle impacts, I built an ice particle source based on a vibrating orifice aerosol generator connected directly to vacuum. Ice particles produced in this manner can be electrostatically accelerated for impact ionization studies.

Hypervelocity impact vaporization may have played a key role in the mass extinction that occurred at the Cretaceous-Tertiary (K-T) boundary. In order to study the speciation of gases that may have been produced in such an asteroid impact, I designed a specialized orthogonal extraction mass spectrometer for future laboratory impact experiments.

Contents

List of Figures

List of Tables

Abbreviations and Acronyms

AU	Astronomical unit
CDA	Cosmic Dust Analyzer
CIDA	Cometary and Interstellar Dust Analyzer
GORID	Geostationary ORbit Impact Detector
IR	infrared
MCP	microchannel plate ion detector
m/z	mass to charge ratio
PIA	Particulate Impact Analyzer
PUMA	Russian acronym for 'dust impact mass analyzer'
SIMS	secondary ion mass spectrometry
UV	ultraviolet
VOAG	vibrating orifice aerosol generator

Chapter 1

Cosmic Dust and Impact-Ionization Mass Spectrometry

1.1 Cosmic dust

Scattered throughout the observable universe is a great diversity of microscopic particles, known collectively as cosmic dust. Cosmic dust is responsible for such phenomena as zodiacal light, comet tails, extinction of light from distant stars, the transfer of heavy elements from supernovae to emerging star systems, and perhaps even the abiotic synthesis of complex organic molecules [1, 2]. Cosmic dust grains fall into two classifications: interstellar dust and interplanetary dust.

Interstellar dust is generally defined as particulate matter that originates outside of the solar system. Interstellar dust grains are created during a variety of stellar phenomena including supernovae, red giants, and carbon-rich stars [3]. The chemical and isotopic properties of dust grains provide important information about the stellar processes taking place in the environments in which the grains were formed. Because the material making up the Earth and other planets was, at one time, interstellar dust, the chemical and isotopic properties of dust grains provide information about planetary formation processes. Interstellar dust may make up the difference between the observed

abundances of elements heavier than helium in the interstellar gas and the assumed cosmic abundances of the elements [4]. A significant fraction of the total galactic mass may be hidden in these optically invisible grains. Interstellar dust flows through the solar system with a speed of 26 km/s coming from the direction of 253° ecliptic longitude and 5° ecliptic latitude [3, 5]. Because cosmic dust grains are electrically charged by photoelectron emission, grains smaller than about 0.1 μm are deflected by the sun's magnetic field, and do not frequently penetrate the solar system [6-9]. Larger grains are frequently seen even as close to the sun as 1 AU [10]. In fact, about 30% of the micron-sized dust reaching the Earth is of interstellar origin [3]. A variety of pre-solar grains have been discovered and characterized from meteorites that have survived impact on the Earth [11], but the bulk composition of the interstellar dust remains unknown.

Interplanetary dust is defined as particulate matter originating within the solar system. This includes cometary debris, planetary rings, man-made debris (frequently encountered in Earth orbit), particles created during asteroid and meteor impacts, and various other local sources. Particles in the size range of 10-100 μm account for most of the light scattering in the zodiac [12]. Most interplanetary dust grains eventually assume quasi-stable orbits around the sun, although radiation pressure, charge and magnetic interactions, and gravitational resonances all complicate their trajectories and lifetimes. The dynamics, distributions, and possible sources of various dust populations within the solar system have been extensively studied [13, 14]. The elemental composition of most solar system dust grains is approximately chondritic, although individual particles may have disproportionate contributions from specific minerals such as magnesium silicates,

iron-nickel metal, sulfides, phosphides, or carbonates [15]. For a thorough review of cosmic dust see reference [16].

1.2 Methods for studying cosmic dust

Methods for studying interplanetary and interstellar dust include remote sensing, collection and analysis of dust grains that have survived impact on the Earth, capture and return of dust samples to Earth for study, and *in situ* analysis using instruments on spacecraft. Remote sensing techniques, such as analysis of zodiacal light [16], extinction of stellar emissions [17], and thermal emissions [18], are useful primarily for studying dynamics and distributions of dust populations. Dust grains collected from the Earth environment, including the upper atmosphere, polar ice, and deep-sea sediments, provide information about structure and composition, but these properties may have been altered by atmospheric heating, chemical reactions, or contamination [15]. Sample capture and return, such as that planned for the STARDUST comet fly-by [19], allows in-depth analysis of dust grains by Earth-based laboratories. However, sample return is limited to studying dust relatively close to the Earth, and the collection and delivery of samples poses numerous risks and uncertainties. Finally, dust may be studied directly by *in situ* instruments. Although limited by the low-power and low-mass requirements of space flight, *in situ* dust analyzers have proven useful for determining such properties as composition, mass, charge, distributions, and dynamics of dust at various locations within the solar system. The principal goals of *in situ* analysis are determination of the elemental and isotopic compositions of individual grains, and determination of the size

distributions of grains. These properties cannot be measured by astronomical observations, but they are essential to understanding the sources and evolution of any type of dust [3].

Dust grains, typically 0.1 to 10 μm, encounter spacecraft and *in situ* instruments at relative velocities of up to 80 km/s [20]. At such high velocities, the dust grain and a portion of the surface it hits are partially vaporized and ionized [21, 22]. The impact ionization process is illustrated in Figure 1.1. The shock wave produced by the impact creates both positive ions and free electrons in a dense, expanding plasma [23]. The electrons, which are more mobile than the ions, escape the expanding plasma cloud faster, resulting in a charge separation. The remaining cloud of atomic and/or molecular ions emerges from a region of high positive space charge. High-velocity dust impacts produce ions with large and varied initial kinetic energies, typically several eV [24, 25]. For a given element, the quantity of ions produced depends on the impact velocity, the density of the materials involved in the impact, and other factors. Impact ionization was originally observed by Friichtenicht [26]. Subsequent studies have evaluated the possibility of using the ions produced in a hypervelocity impact to measure the properties of cosmic dust grains [27, 28]. Chapter 4 contains a more detailed description of impact ionization, including the results of experiments, theoretical treatments, and other considerations.

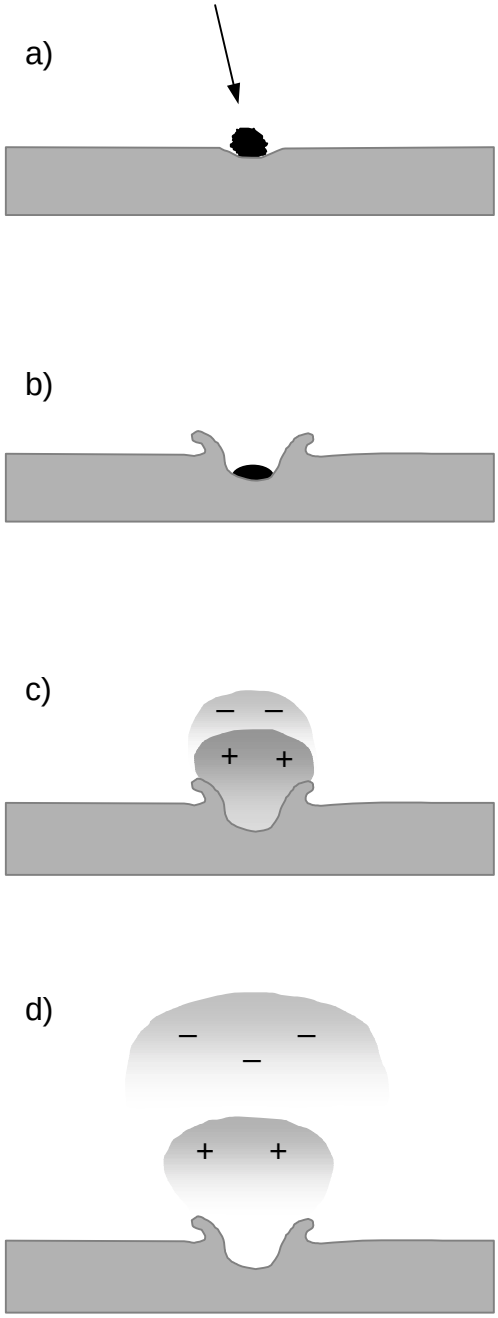

Figure 1.1. Impact ionization scenario: a) particle impacts, b) melting and formation of crater, c) formation of vapor and ions, and d) expansion of ion clouds (electrons and positive ions). Electrons leave more quickly due to higher mobility. Neutral species are also formed, but are not shown in this illustration.

1.3 Instrumentation for *in situ* analysis of cosmic dust

In situ dust detectors utilize impact ionization either by measuring the electrical current created on the target surface or on a nearby grid, or by time-of-flight mass spectrometric analysis of the resulting ions. Only the latter method provides information about the composition of the dust grain. Previous dust analyzers that measured the charge produced from impact include the Ulysses [29] and Galileo [30] dust detectors, and the GORID [14] dust detector. Previous impact ionization time-of-flight mass spectrometers for dust analysis include the Particulate Impact Analyzer (PIA) and the Dust Impact Mass Analyzer (PUMA) instruments used in the Halley comet fly-by [31], the Cassini Cosmic Dust Analyzer (CDA) [32], and the STARDUST Cometary and Interstellar Dust Analyzer (CIDA) [19].

The PIA and PUMA dust analyzers and the STARDUST CIDA were based on the same design, which is shown in Figure 1.2. Because impact-generated ions exhibit a wide range of initial kinetic energies, these mass spectrometers used reflectrons, originally described by Mamyrin [33], to compensate for the initial energy distribution of the ions. Figure 1.3 shows a diagram of a basic reflectron. Ions with greater initial kinetic energy penetrate farther into the reflectron, thus taking a longer path to the detector. The detector is located at the point where faster and slower ions meet (the space-focus plane). The use of a reflectron allowed mass resolution of around 200 for most spectra obtained with these instruments.

The PIA, PUMA, and CIDA mass spectrometers were each approximately 1 meter in length and 17 kilograms in mass. Also, the target plate dimensions on these

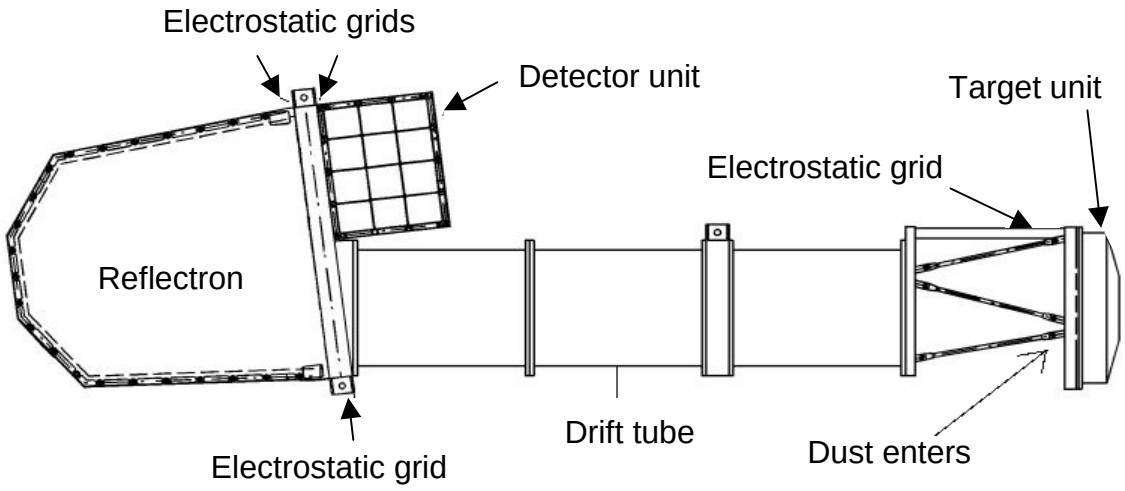

Figure 1.2. Design of PIA and PUMA dust analyzers. Instrument is approximately 120 cm long. STARDUST CIDA is nearly identical, but with larger impact target. Dust grains impact a rhodium target plate. Resulting ions are electrostatically extracted and accelerated through drift tube. Reflectron directs ions to detector and compensates for variations in initial kinetic energies of ions.

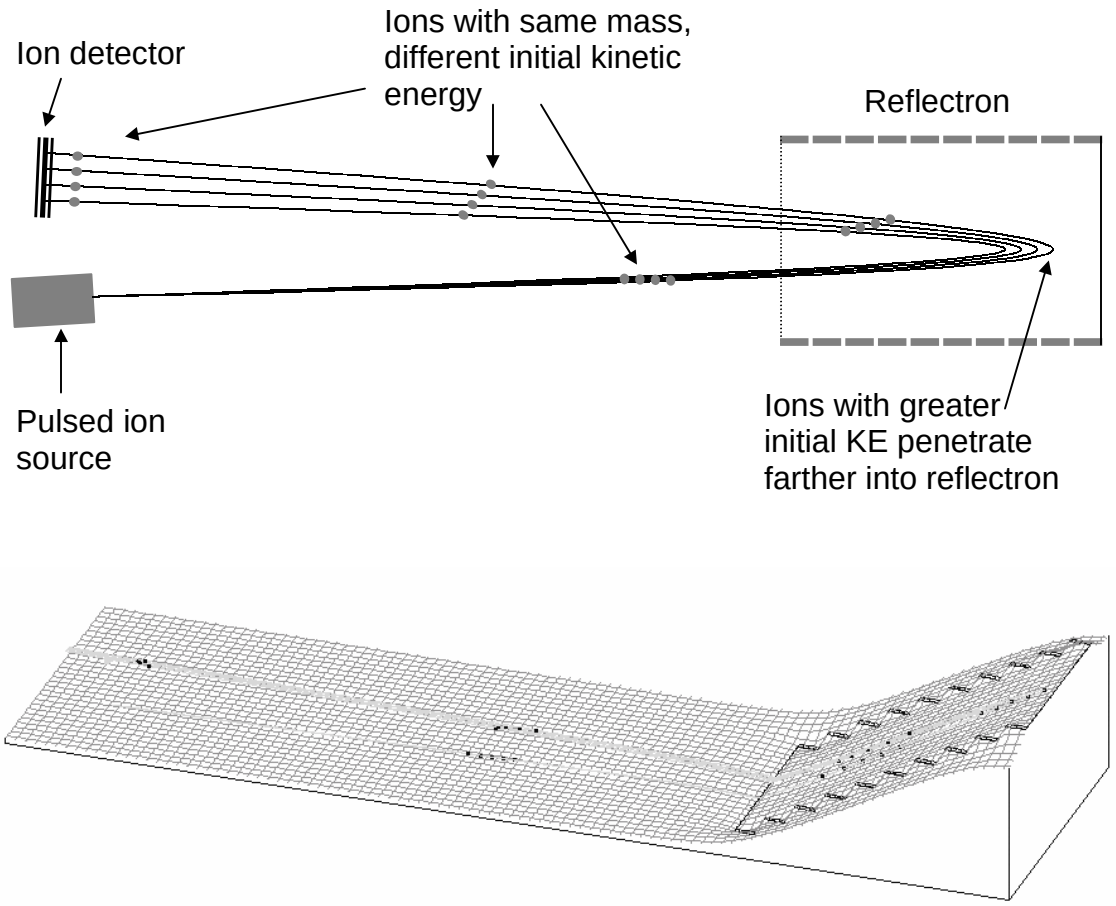

Figure 1.3. A typical reflectron. Ions of a given m/z are produced simultaneously by a source and accelerated to some voltage. Differences in the initial kinetic energies of ions result in spreading. Ions enter the reflectron. Ions with greater initial kinetic energy penetrate farther into the reflectron, resulting in a longer flight path to the ion detector. Detector is positioned at the space-focus plane, where ions arrive nearly simultaneously. The lower illustration shows the electrostatic potential surface of the reflectron setup.

instruments were small in relation to the overall instrument size (5 cm^2 for PIA and PUMA, 50 cm^2 for CIDA). Small target plates are useful for regions with high concentrations of dust, such as in the vicinity of a comet, but are less appropriate for regions with low concentrations of dust [32].

In regions where cosmic dust is sparse, a large active target area is needed in order to record a statistically significant number of impact events. The Cassini Cosmic Dust Analyzer, or CDA, was designed for regions of the solar system with low and medium concentrations of dust. Figure 1.4 shows a diagram of the CDA. It has a large impact surface, of which 200 cm^2 is used for mass spectrometry on impinging dust grains [34]. A reflectron was not included in this 17-kg instrument because of the difficulty of combining a reflectron with a large target area and the simultaneous operation of the impact plasma sensor [32]. Due to the lack of a reflectron, or other energy compensating device, mass resolution in the CDA is low (5-20 in many cases). Peak identification in some spectra is not possible.

Recently NASA has placed emphasis on developing smaller, lighter, lower-power spacecraft and instruments. Considering the limitations of previous instruments I have designed and built a compact impact-ionization time-of-flight mass spectrometer for *in situ* analysis of cosmic dust, suitable for use on future deep space missions. Named the Dustbuster, this time-of-flight mass spectrometer combines the best aspects of previous dust analyzers in a more compact design. The Dustbuster includes a reflectron, modified so that it corrects for initial ion energies and also focuses the ions from a large target area onto the ion detector. This modified reflectron allows mass spectra to be obtained from dust grains hitting a 65-cm^2 target, with sufficient mass

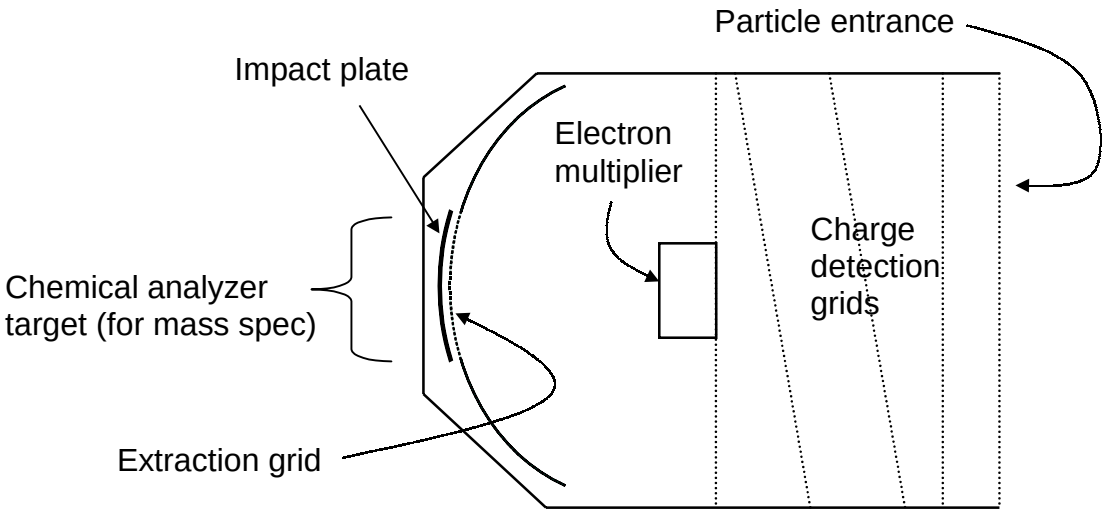

Figure 1.4. The Cassini Cosmic Dust Analyzer (CDA). Instrument is 0.4 m in diameter and has a mass of 17 kg. Charge detection grids measure charge, velocity, and direction of incoming dust. Time-of-flight mass spectrometer measurements are made only for those particles impacting the chemical analyzer target, located in the center of the impact plate.

resolution to measure isotopic distributions of most elements. The active target area is large compared to the instrument size, and of sufficient size to be useful for regions of the solar system with low dust concentrations. The Dustbuster, measuring only 10 cm in diameter and 20 cm in length, and weighing approximately 0.5 kg, is much smaller and lighter than previous dust mass spectrometers. The design of the Dustbuster is described in detail in Chapter 2.

1.4 References

1. Blake, G., *Class notes from Ch/Ge 128, Cosmochemistry, Caltech*. 2000.
2. Greenberg, J. M. and Caro, G. M. M., *Organics in space: from interstellar dust to comets.* Astrochemistry: from molecular clouds to planetary systems IAU symposia, 2000. **197**: p. 331-342.
3. Grun, E.; Landgraf, M.; Horanyi, M.; Kissel, J.; Krüger, H.; Srama, R.; Svedhem, H.; Withnell, P., *Techniques for galactic dust measurements in the heliosphere.* Journal of Geophysical Research, 2000. **105**(A5): p. 10403-10410.
4. Frisch, P. C., *The nearby interstellar medium.* Nature (London), 1981. **293**: p. 377-379.
5. Witte, M.; Rosenbauer, H.; Banaskiewicz, M.; Fahr, H., *The Ulysses neutral gas experiment: determination of the velocity and temperature of the neutral interstellar helium.* Advances in Space Research, 1993. **13**(6): p. 121-130.
6. Frisch, P. C., *Dust in the local interstellar wind.* Astrophysical Journal, 1999. **525**(1): p. 492-516.
7. Landgraf, M.; Baggaley, W. J.; Grun, E.; Krüger, H.; Linkert, G., *Aspects of the mass distribution of interstellar dust grains in the solar system from in situ measurements.* Journal of Geophysical Research, 2000. **105**(A5): p. 10343-10352.

8. Kimura, H. and Mann, I., *The electric charging of interstellar dust in the solar system and consequences for its dynamics.* Astrophysical Journal, 1998. **499**(454-462).

9. Landgraf, M.; Augustsson, K.; Grun, E.; Gustafson, B. A. S., *Deflection of the local interstellar dust flow by solar radiation pressure.* Science, 1999. **286**(5448): p. 2319-2322.

10. Grun, E.; Staubach, P.; Baguhl, M.; Hamilton, D. P.; Zook, H. A.; Dermott, S.; Gustafson, B. A.; Fechtig, H.; Kissel, J.; Linkert, D.; Linkert, G.; Srama, R.; Hanner, M. S.; Polanskey, C.; Horanyi, M.; Lindblad, B. A.; Mann, I.; McDonnell, J. A. M.; Morfill, G. E.; Schwehm, G., *South-north and radial traverses through the interplanetary dust cloud.* Icarus, 1997. **129**(2): p. 270-288.

11. Zinner, E., *Stellar nucleosynthesis and the isotopic composition of presolar grains from primitive meteorites.* Annual Review of Earth and Planetary Sciences, 1998. **26**: p. 147-188.

12. Grun, E., *Dust measurements in the outer solar system.* Asteroids, Comets, Meteors 1993 IAU Symposia, 1994. **160**: p. 367-380.

13. Mann, I. and Grun, E., *Dust particles beyond the asteroid belt—a study based on recent results of the Ulysses dust experiment.* Planetary and Space Science, 1995. **43**(6): p. 827-832.

14. Drolshagen, G.; Svedhem, H.; Grun, E.; Bunte, K. D., *Measurements of cosmic dust and micro-debris in GEO.* Advances in Space Research, 2001. **28**(9): p. 1325-1333.

15. Brownlee, D. E. *The elemental composition of interplanetary dust*. in *Physics, Chemistry, and Dynamics of Interplanetary Dust, 150th Colloquium of the International Astronomical Union*. 1995. Gainesville, Florida: Astronomical Society of the Pacific Conference Series, San Francisco.

16. Grun, E.; Gustafson, B. A.; Dermott, S.; Fechtig, H., eds. *Interplanetary Dust*. 2001, Springer: New York.

17. Mathis, J. S., *Interstellar dust and extinction.* Annual Reviews of Astronomy and Astrophysics, 1990. **28**: p. 37-70.

18. Mann, I. *Dust near the sun*. in *Physics, Chemistry, and Dynamics of Interplanetary Dust, 150th Colloquium of the International Astronomical Union*. 1995. Gainesville, Florida: Astronomical Society of the Pacific Conference Series, San Francisco.

19. Brownlee, D. E.; Burnett, D.; Clark, B.; Hanner, M. S.; Horz, F.; Kissel, J.; Newburn, R.; Sandford, S.; Sekanina, Z.; Tsou, P.; Zolensky, M. *STARDUST: comet and interstellar dust sample return mission*. in *Physics, Chemistry, and Dynamics of Interplanetary Dust,150th Colloquium of the International Astronomical Union*. 1995. Gainesville, Florida: Astronomical Society of the Pacific Conference Series, San Francisco.

20. Hornung, K.; Malama, Y. G.; Kestenboim, K. S., *Impact vaporization and ionization of cosmic dust particles.* Astrophysics and Space Science, 2000. **274**: p. 355-363.

21. Hornung, K.; Malama, Y. G.; Thoma, K., *Modeling of the very high velocity impact process with respect to in situ ionization measurements.* Advances in Space Research, 1996. **17**(12): p. (12)77-(12)86.

22. Hornung, K. and Kissel, J., *On shock wave impact ionization of dust particles.* Astronomy and Astrophysics, 1994. **291**: p. 324-336.

23. Hansen, D. O., *Mass analysis of ions produced by hypervelocity impact.* Applied Physics Letters, 1968. **13**(3): p. 89-91.

24. Ratcliff, P. R. and Allahdadi, F., *Characteristics of the plasma from a 94 km/s microparticle impact.* Advances in Space Research, 1996. **17**(12): p. (12)87-(12)91.

25. Abramov, V. I.; Bandura, D. R.; Ivanov, V. P.; Sysoev, A. A., *Energy and angular characteristics of ions emitted in the impact of accelerated dust particles on a target.* Sov. Tech. Phys. Lett., 1991. **17**(3): p. 194-195.

26. Friichtenicht, J. F., *Micrometeoroid simulation using nuclear accelerator techniques.* Nuclear Instruments and Methods, 1964. **28**: p. 70-78.

27. Friichtenicht, J. F.; Roy, N. L.; Becker, D. G. *The Cosmic Dust Analyzer: experimental evaluation of an impact ionization model*. in *International Astronomical Union Colloquium #13*. 1971. State University of New York, Albany, NY: Scientific and Technical Information Office, NASA, Washington, D.C.

28. Auer, S. and Sitte, K., *Detection technique for micrometeoroids using impact ionization.* Earth and Planetary Science Letters, 1968. **4**: p. 178-183.

29. Grun, E.; Fechtig, H.; Giese, R. H.; Kissel, J.; Linkert, D.; Maas, D.; McDonnell, J. A. M.; Morfill, G. E.; Schwehm, G.; Zook, H. A., *The Ulysses dust experiment.* Astronomy & Astrophysics, Supplement Series, 1992. **92**: p. 411-423.

30. Grun, E.; Fechtig, H.; Hanner, M. S.; Kissel, J.; Lindblad, B.-A.; Linkert, D.; Maas, D.; Morfill, G. E.; Zook, H. A., *The Galileo dust detector.* Space Science Reviews, 1992. **60**: p. 317-340.

31. Kissel, J.; Sagdeev, R. Z.; Bertaux, J. L.; Angarov, V. N.; Audouze, J.; Blamont, J. E.; Buchler, K.; Evlanov, E. N.; Fechtig, H.; Fomenkova, M. N.; von Hoerner, H.; Inogamov, N. A.; Khromov, V. N.; Knabe, W.; Krueger, F. R.; Langevin, Y.; Leonas, V. B.; Levasseur-Regourd, A. C.; Managadze, G. G.; Podkolzin, S. N.; Shapiro, V. D.; Tabaldyev, S. R.; Zubkov, B. V., *Composition of Comet Halley dust particles from Vega observations.* Nature (London), 1986. **321**: p. 280-282.

32. Ratcliff, P. R.; McDonnell, J. A. M.; Firth, J. G.; Grun, E., *The Cosmic Dust Analyzer.* J. British Interplanetary Soc., 1992. **45**(9): p. 375-380.

33. Mamyrin, B. A.; Karataev, V. I.; Shmikk, D. V.; Zagulin, V. A., *The mass-reflectron, a new nonmagnetic time-of-flight mass spectrometer with high resolution.* Sov. Phys. JETP, 1973. **37**: p. 45-47.

34. Srama, R. and Grun, E., *The dust sensor for Cassini.* Advances in Space Research, 1997. **20**(8): p. 1467-1470.

Chapter 2

The Dustbuster: A Compact Time-of-flight Mass Spectrometer for Cosmic Dust Analysis

2.1 Objectives in designing an improved cosmic dust mass spectrometer

Five goals defined my efforts to design an improved cosmic dust mass spectrometer. First, the instrument should have high mass resolution. Ideal resolution would be around 300 ($m/\Delta m$). This would allow for the identification of isotopes of any element even in less than ideal circumstances, assuming no interference. Second, the instrument should be lightweight, low-power, and otherwise physically suitable for inclusion on a spacecraft. Based on estimates from several proposed missions, our target mass was 1 kg or less, and target power was less than 3 W. Third, the instrument should have a large enough impact area that dust impacts would be reasonably frequent. A 50-cm^2 area sweeping out space at typical interplanetary cruising velocities would encounter interstellar dust at a rate of about one impact per week. For interstellar dust, and for interplanetary dust far away from its source, this impact area would be sufficient. Of course, for regions where dust is dense, such as a comet tail or planetary ring, a smaller impact plate is adequate. Finally, the instrument design should be adaptable to a variety of dust environments or proposed missions. It is a fact of life in dealing with the

space program that missions are sometimes changed or cancelled. In addition, competition for scientific payload space is tight, so proposing an instrument for several missions increases the chances that the instrument will fly.

The original name of this improved cosmic dust mass spectrometer was the Advanced Space Particle Analysis System, but at the suggestion of another student, it was given the appellation "Dustbuster." It was thought that a catchy name would make the instrument more memorable in presentations (especially to NASA mission planners). I beg the pardon of Black & Decker®, the makers of the Dustbuster™ portable vacuum cleaner, although I have been assured that trademark infringement is not an issue in this case.

The Dustbuster research was funded by NASA's Planetary Instrument Definition and Development Program (PIDDP). As such it was not my intention to engineer and build a flight-ready, fully certified instrument, with all subsystems assembled and ready for launch. Rather I have developed the instrument through simulations and laboratory experiments, with the goal being the production of a workable design and a good understanding of the design's potential. Hopefully the instrument design will find its eventual way into a flight proposal, then into the hands of capable engineers and machinists who will build it, and finally, off into space where it will sit and collect dust.

2.2 Early designs and obstacles

The original design concept was part of the original PIDDP proposal submitted to NASA in 1997. This design included a planar target plate, a reflectron, a drift tube

with Einzel lens, and an ion detector, as shown in Figure 2.1. It was originally proposed that the mass spectrometer be combined with both laser scattering equipment and piezoelectric transducers to measure the trajectories and sizes of incoming particles. However, both the laser scattering and piezoelectric segments of instrument development were abandoned early on due to limited resources.

Several early designs I developed included two reflectrons, similar to what is shown in Figures 2.2a and 2.2b. These designs had the advantage that the ion detector was completely shielded from any incident particles or radiation, and from any secondary emissions or ejecta. A second advantage to these designs was that the out-of-reflectron path length was folded, and could be made sufficiently long without substantially lengthening the whole instrument. The first reflectron could occupy the length of the wide section of the instrument, while the rear reflectron could be very short, perhaps only a few millimeters (nothing more than an ion mirror). However, kinetic energy focusing for ions traveling through two consecutive reflectrons is more complex, and the ion beam spreads out more due to increased space-charge effects.

A number of my early designs used either a dual-stage reflectron (such as those in Figures 2.2b and 2.2c) or a quadratic reflectron. The idea behind these attempts was to minimize the ion drift region, again minimizing the size of the instrument. A limitation with some of these designs was that the ion detector was too exposed and susceptible to damage by incoming particles. In addition, generating a quadratic reflectron with such a large area is rather difficult unless several grids are used, and each grid reduces the total ion transmission and instrument sensitivity.

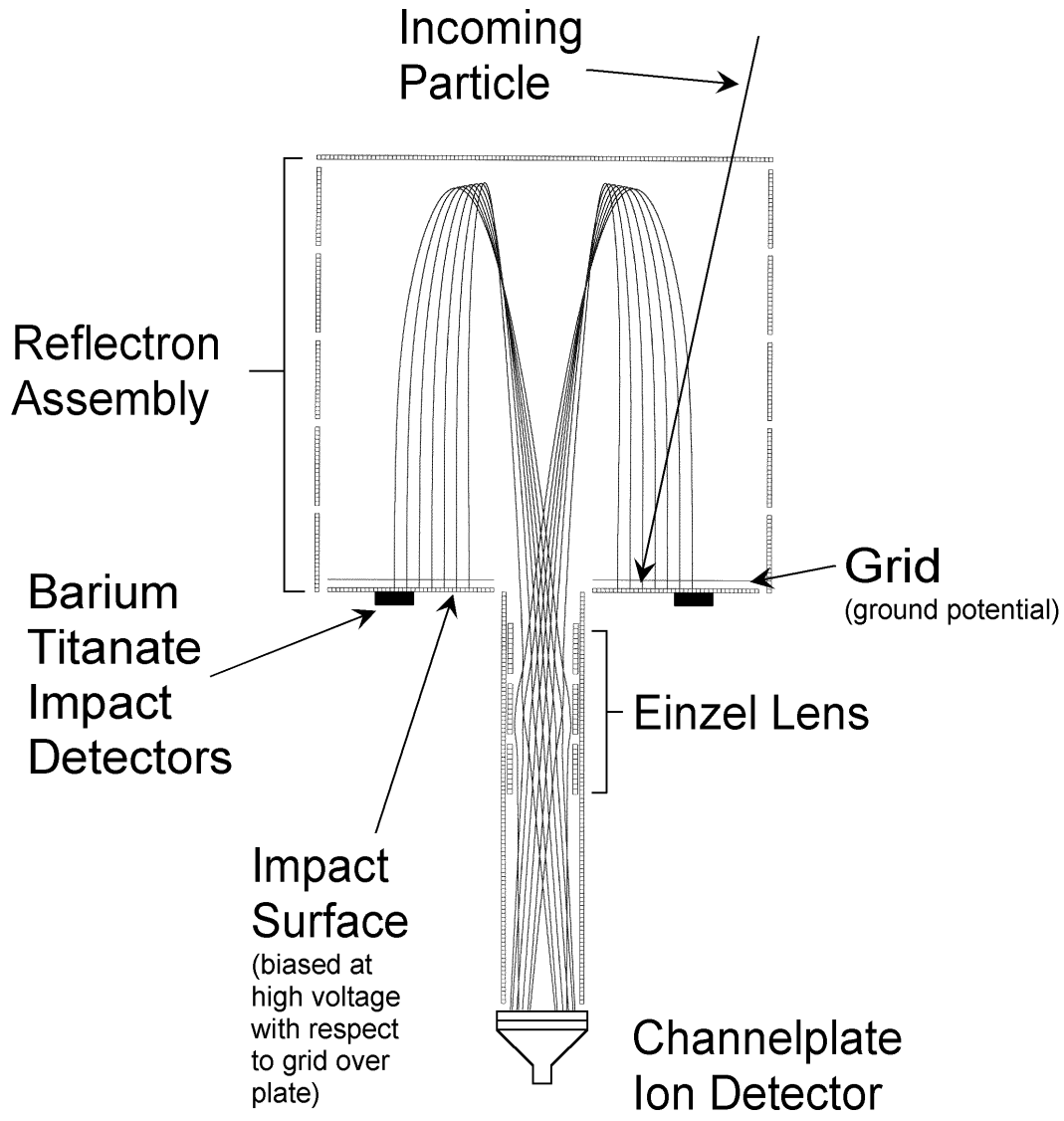

Figure 2.1. The original Dustbuster design (side view) as submitted to NASA in 1997 as part of the PIDDP proposal. Particles enter from the top and strike the biased impact surface. Ions formed by the impact are accelerated back down toward the front of the analyzer and redirected to the aperture in the center of the impact plate by appropriate potentials applied to the ring electrodes and entrance grid (which together comprise a reflectron). An Einzel lens near the entrance to the lower flight tube directs the ions to the channelplate detector.

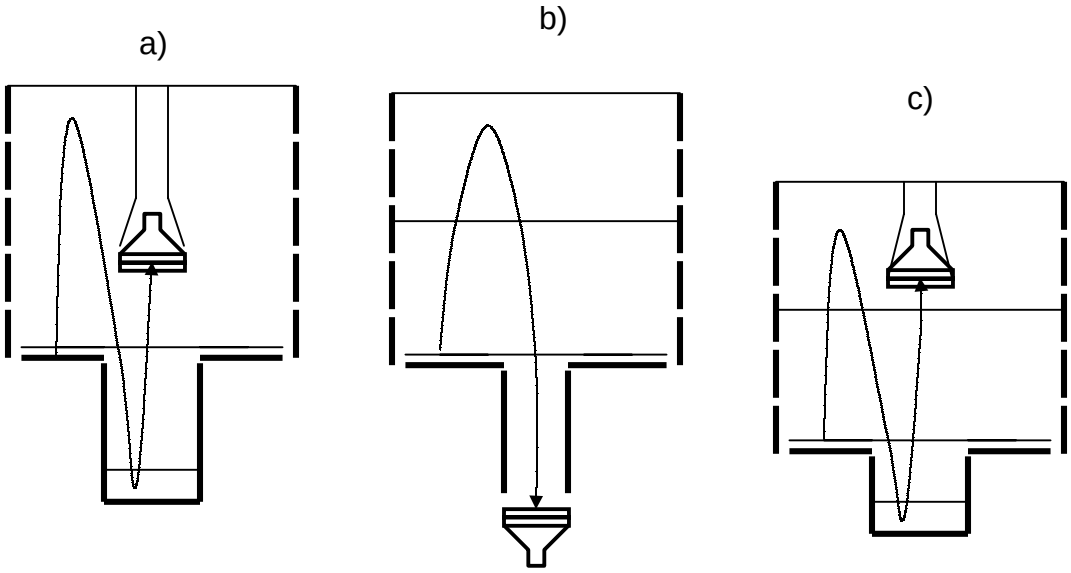

Figure 2.2. Several early Dustbuster designs: a) incorporating two reflectrons, b) with a dual-stage reflectron, and c) with both a dual-stage reflectron and second reflectron. General features are similar to those in Figures 2.1 and 2.3. Dust grains enter from the top of instrument in each case. Typical ion trajectories are shown.

These early designs revealed several limitations taken into consideration in later designs. One limitation is the difficulty of using a reflectron to focus ions originating from a large surface. Ion optics systems and methodologies typically use “point-like” ion sources, which are readily available for most laboratory experiments. In space, however, a large surface is needed to acquire a statistically significant number of dust impacts. Focusing ions from a large area is simple (for instance, the hemispherical impact plate of the Cassini Cosmic Dust Analyzer, in which all ions are focused into the center), but the simultaneous use of a reflectron introduces complications. However, because of the large initial kinetic energies of impact-generated ions, the reflectron is necessary in order to produce spectra with sufficient mass resolution to be useful.

A second limitation stems from the need to include a field-free drift region in a reflectron path. For a linear reflectron, the space-focus plane will be located approximately at the point in which ions will have spent equal amounts of time within and without the reflectron. Thus a drift region is essential to achieve high resolution in a linear reflectron system. For dual-stage and quadratic reflectrons, drift length requirements are different. Ions focused from a large area through a reflectron will retain transverse velocity through the drift tube. This transverse velocity component limits spatial focusing and makes difficult the use of both a small aperture at the reflectron exit and a small ion detector. An Einzel lens in the drift tube has limited power at resolving this problem. Einzel lenses are useful when ions originate at a point close to the optical axis, at some distance greater than the focal length of the lens. For close, off-axis ion sources, however, the aberrations of an Einzel lens become large, and transverse velocity components cannot be effectively corrected.

2.3 Working design

The instrument design which worked best in simulations, and which was constructed and used in subsequent experiments, is shown in Figure 2.3. The principal components are the impact plate, the reflectron region, the drift tube, and the ion detector.

Dust grains enter the instrument through the front grid, proceed through the extraction grid, and strike the impact plate, where they are partially ionized by the impact. The positive ions produced at the plate are accelerated to 4800 V by the grounded extraction grid, located 2-3 mm in front of the impact plate. Due to the close proximity of the extraction grid to the impact plate, the grid needs to have both high ion transmission and low field penetration in order to insure that most ions are extracted with minimum perturbation. At the same time, the grid needs to be sufficiently robust to withstand several dust impacts while retaining its shape or its tautness. Of course, ideal grids do not exist, but a grid suitable for laboratory experiments was a 70% transmission, 333 wire-per-inch electroformed nickel mesh manufactured by Buckbee-Mears St. Paul. A thicker, more expensive custom gold mesh may be more appropriate for a flight instrument.

The target plate itself is a 75-cm^2 disk which has an active area of 65 cm^2 for dust analysis. The target must be made out of a material with high density and high melting point in order to maximize the number of ions produced in a given dust impact event [1, 2]. Because a portion of the target plate is also ionized when a dust grain

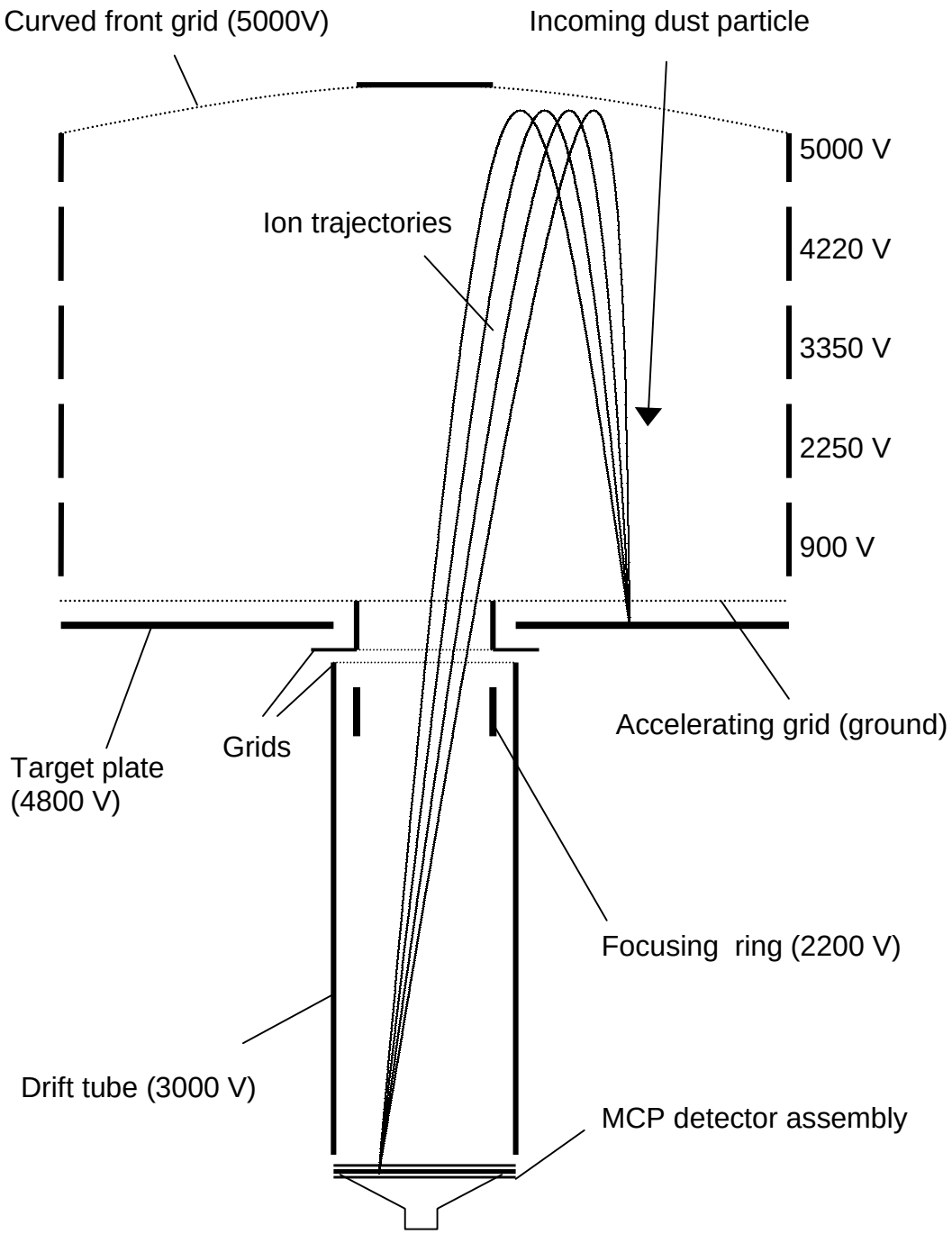

Figure 2.3. Design of the "working" version of the Dustbuster. Typical ion trajectories are shown. Particles partially ionize upon impact with the target plate. Ions are accelerated into the reflectron, then focused onto the microchannel plate detector at the bottom of the figure.

impacts, the target plate must be made out of a material with low cosmic abundance to avoid interference with the dust composition. Rhodium and silver [3, 4] have been used for target plates in previous instruments, and tantalum or gold would also likely work [5]. A copper plate was used in laser ionization experiments, and a tantalum plate was used for microparticle impact studies, both of which will be described in a later section. A target containing two metals might work best for a flight instrument since the mass spectra could be calibrated using ions of both elements from the target plate.

The reflectron region consists of five ring electrodes with voltages (with respect to the accelerator grid) of 5000 V, 4220 V, 3350 V, 2250 V, and 900 V, as shown in Figure 2.3. In a previous publication [6] the ring voltages were reported as 5000 V, 3710 V, 2950 V, 2160 V, and 960 V. The latter are the voltages used in preliminary experiments, and they produce similar results to the former set of voltages. Varying the voltages on the other rings can easily compensate for a 5% variation in the voltage of any one ring, so many possible combinations of ring voltages can work equally well. These reflectron rings provide a longitudinal potential gradient, just as a standard reflectron does, in order to compensate for the initial kinetic energies of the ions. The rings also provide a small radial (transverse) gradient, pushing the ions toward the center of the instrument. Ions originating from approximately 65 cm^2 of the target plate will be focused into the drift tube and onto the MCP detector. This modified reflectron design makes it possible simultaneously to optimize spatial focusing and energy focusing. In addition, any neutrals, liquid droplets, or solid ejecta fragments that might be produced [4, 7] during the impact will not reach the detector, simplifying spectra and preserving the life of the microchannel plates.

The front grid defines the end of the reflectron field. A result of the transverse potential gradient in the reflectron is that ions with initial velocity outward have a longer path through the reflectron than do ions with initial velocity inward. Curvature of the front grid compensates for this problem. The front grid curvature is actually one of the most crucial factors affecting mass resolution. Ion packets reaching the detector may be completely coplanar, but if the ion packet is not parallel to the ion detector, signals are significantly broadened. The angle of the front grid largely defines the angle of the ion packet at every subsequent point, and can be optimized to match the ion packet angle with the detector surface at that point. The front grid, which is kept at 5000 V, may have less than ideal field penetration, but should have high transmission in order to minimize blockage of incoming dust grains. With a difference of 200 V between the potential at which ions are formed and the front grid, ions will typically penetrate to within a few mm of the grid. This distance is far enough that small field inhomogeneities will not be important.

Ions leave the reflectron through the center of the instrument, pass through several grids, and enter the drift region. The intervening grids provide uniform electric fields in this area, although they are not strictly essential. Although drift tubes are normally grounded, the Dustbuster drift tube is kept at a high potential (3000 V). In general, when a time-of-flight mass spectrometer uses a reflectron, ions with different initial kinetic energies will reach the same plane or focal point after the ions have spent approximately equal amounts of time inside and out of the reflectron [8]. In this case, a grounded drift tube would need to be quite long, about three times the length of the reflectron. Increasing the potential of the drift tube moves the space-focus plane of the

reflectron closer. A high-potential drift tube considerably shortens and lightens the instrument, while sacrificing resolution only minimally. In simulations, resolution is limited mainly by other factors, so the shortened drift tube has little effect on the overall mass resolution. The Dustbuster drift tube is not completely field-free. A small ring electrode (2200 V) at the entrance of the drift tube aids in directing the ions toward the detector. The difference between the voltages of the focusing ring and the drift tube is crucial to obtaining high mass resolution. Just as the curvature of the front grid affects the angle at which ion packets strike the detector, the field imposed by the focusing ring also affects the ion packet angle. Thus it is possible to optimize this angle regardless of the curvature of the front grid, simply by varying the ring voltage. However, significant variations of the voltage of the focusing ring can affect the number of ions that reach the ion detector.

As ions leave the drift tube they are detected using the microchannel plate (MCP) detector. The MCP signal is then amplified and recorded. Despite the popularity and widespread use of MCPs in time-of-flight mass spectrometry, they are not the best detectors for the Dustbuster. Microsphere plate detectors or continuous dynode detectors would be more suitable for a flight instrument, and perhaps also for laboratory prototypes. These other detectors operate at higher pressures, are more robust, and may eliminate the need to have the whole instrument maintained in a sealed vacuum system before and during launch.

Figure 2.4 shows typical trajectories of ions originating from various locations on the target plate. Ions of a given *m/z* from a single dust impact will all have the same flight time, but the time will be slightly different from the flight time of ions of the same

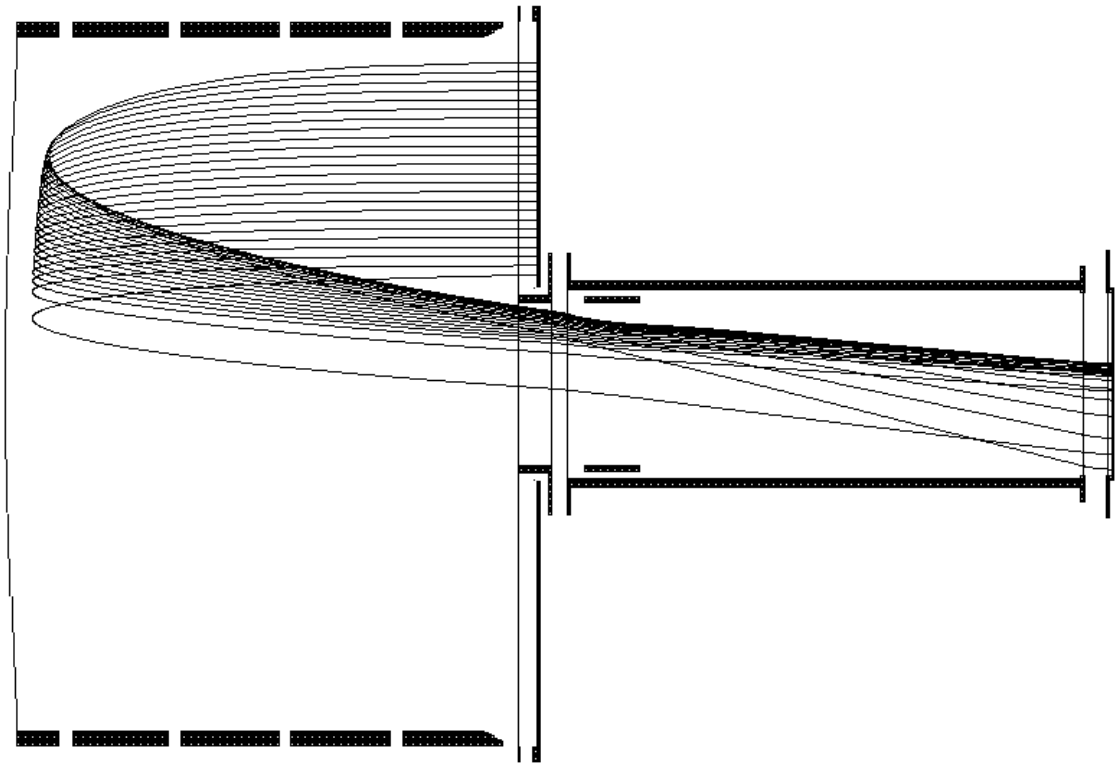

Figure 2.4. Simulation showing trajectories of ions originating from various locations on the Dustbuster target plate. Ions have initial kinetic energy of 40 eV normal to target plate.

m/z from a dust impact elsewhere on the target plate. This variation of flight times with location of dust impact will not present a problem because only one dust grain will strike the instrument at a time. However, the spectrum from each dust impact must be calibrated to compensate for this variation in flight time.

The voltages given in Figure 2.3 are for extraction and detection of positive ions produced during a particle impact. In theory, detection of negative species would simply involve changing the signs of all the voltages (and perhaps floating the detector). However, according to two studies, hypervelocity impacts of metal microparticles typically do not produce a useful abundance of negative ions [5, 9], although impacts of minerals may produce negative ions. If negative ions are produced, the large number of free electrons produced in the impact will interfere with the detection of the negative species unless the detector is able to recharge quickly, or unless the electrons are pulsed out of the way at some point along the flight path.

2.4 Computer simulations of Dustbuster performance

SIMION ion trajectory software [10], versions 6.0 and 7.0, were used extensively both in testing possible designs and in evaluating the working design. Although there is no satisfactory substitute for a good experiment, changing the shape of an electrode is much easier on the computer than in the machine shop.

In order to make full use of SIMION's capabilities, I wrote a spreadsheet to simulate the properties of positive ions emerging from an impact-generated plasma. Ions were assumed to originate from within a hemisphere of given radius corresponding

either to the dust particle size, or to the point in the plasma expansion at which ion-ion collisions dropped to a certain frequency. The center of the hemisphere was located on or slightly above the impact plate surface in each case. Ions were defined individually with randomly distributed positions within the hemisphere, and randomly distributed initial kinetic energies within a specified range. The number of ions in each simulation could be specified from 1 to 50,000. For most performance simulations, groups of 500 ions were defined to have initial kinetic energies with a Gaussian distribution centered at 40 ± 25 eV. Ion groups were designed to have an overall spatial distribution (particle density function) of isotopic, $\cos\theta$, or $\cos^2\theta$ about the normal to the target plate. These represent the energy and angular distributions of ions reported by Ratcliff and Alladhadi [11] for a 94 km/s impact, and have been used for simulations by other researchers in this field [12]. Impacts at lower velocities will produce ions with lower energies [13]. A variety of ion mass-to-charge ratios were used. The details of the ion definition spreadsheet are given in Appendix B.

In simulations with 40 eV ions, mass resolution ($m/\Delta m$) ranged from 100 to 400, with higher resolution for impacts closer to the axis of the instrument. Ion collection efficiency ranged from 15-35%, with most ion losses caused by the grids through which the ions passed. Also, many ions in simulations were unable to pass through the entrance to the drift tube, which also contributed significantly to the overall collection efficiency. Note that SIMION treats grids as having 100% transmission. Space-charge effects, other than those included in the ion definition spreadsheet, were not used in the trajectory calculations.

Figures 2.5, 2.6, and 2.7 show the trajectories of singly charged ^{56}Fe ions, with initial kinetic energy of 25 ± 7 eV and *cos* θ angular distribution. In Figure 2.5, the particle impact was located toward the center of the target plate (small radial distance from instrument axis). In Figure 2.6, the particle impact was located at an intermediate radial distance. In Figure 2.7 the particle impact was located toward the outside of the target plate. Ion packets are shown at various time intervals chosen for clarity and illustrative effect.

Figure 2.8 illustrates the effect of grid curvature on the orientation of the ion packet prior to impact on the ion detector. Figure 2.8a and Figure 2.8b show ions resulting from front grid curvatures of 0.8 m and 1.3 m radii, respectively. Figure 2.8c shows the result from a planar front grid. Figure 2.8d shows the result from an optimized grid curvature, although optimization of the ion packet angle can come from either grid curvature or from the voltage on the focusing ring.

2.5 Other instrument issues

One issue not yet addressed is that of detector protection. MCP detectors and other ion detectors are sensitive both to UV light and to impacts by dust grains (although the latter has not been tested). It is essential that the Dustbuster detector be protected from both. One obvious solution is to include a solid disk at the center of the front grid. Although this may eliminate most direct light and impacting particles, in order to completely block all direct paths to the detector the disk would need to be quite large. The resulting obstruction would significantly reduce the effective surface area of the

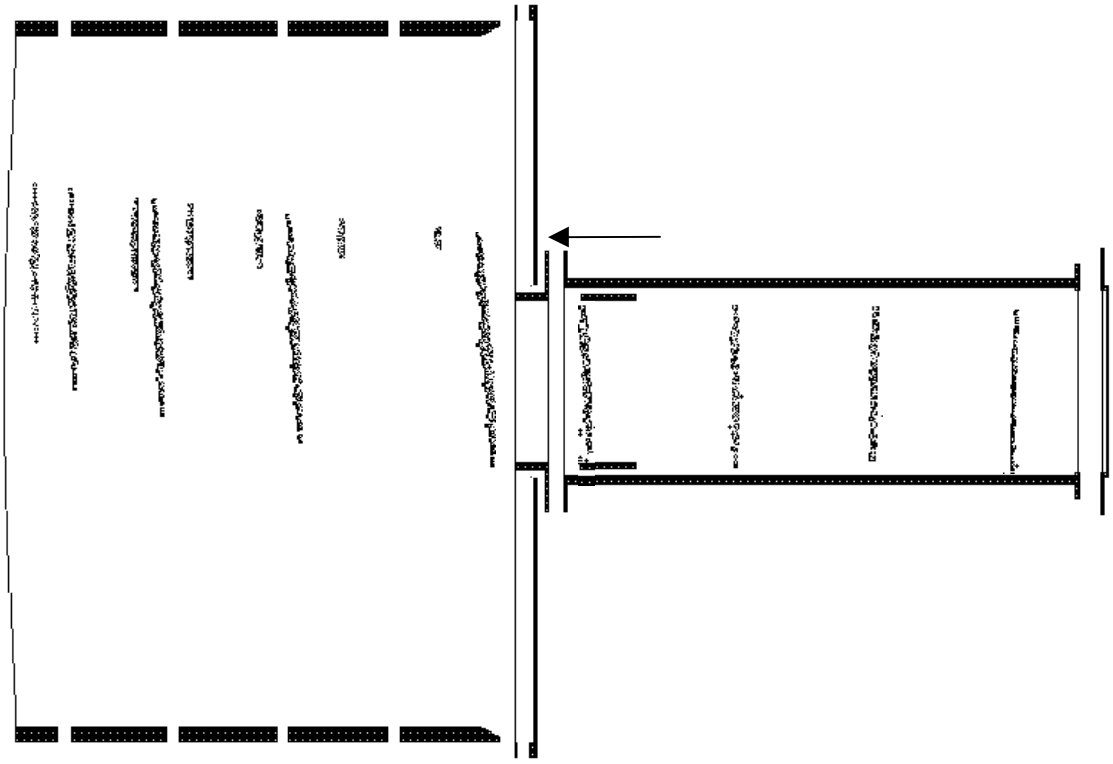

Figure 2.5. Trajectories of ions resulting from an impact near the center of the target plate (indicated with arrow). Simulated ions have initial kinetic energy of 25 +/- 7 eV with a cos θ distribution about the normal. Locations of ions at various time intervals are shown.

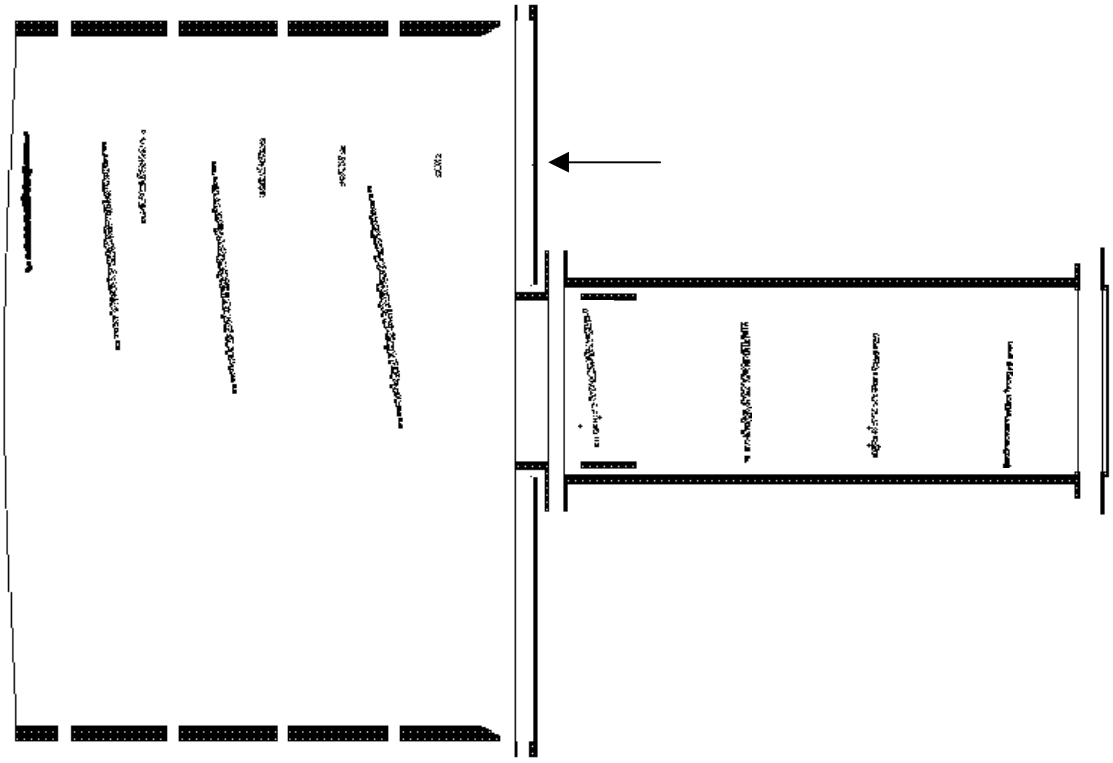

Figure 2.6. Trajectories of ions resulting from an impact at an intermediate radial distance on the target plate (indicated with arrow). Simulated ions have initial kinetic energy of 25 +/- 7 eV with a cos θ distribution about the normal. Locations of ions at various time intervals are shown.

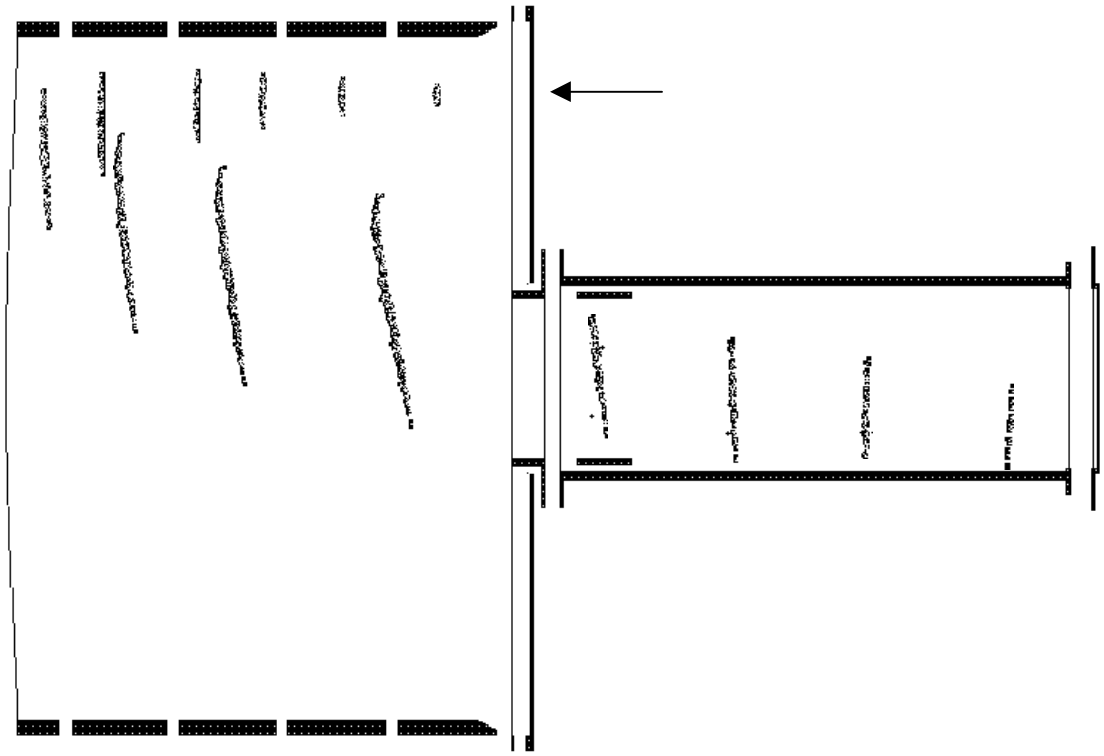

Figure 2.7. Trajectories of ions resulting from an impact near the outside of the target plate (indicated with arrow). Simulated ions have initial kinetic energy of 25 +/- 7 eV with a cos θ distribution about the normal. Locations of ions at various time intervals are shown.

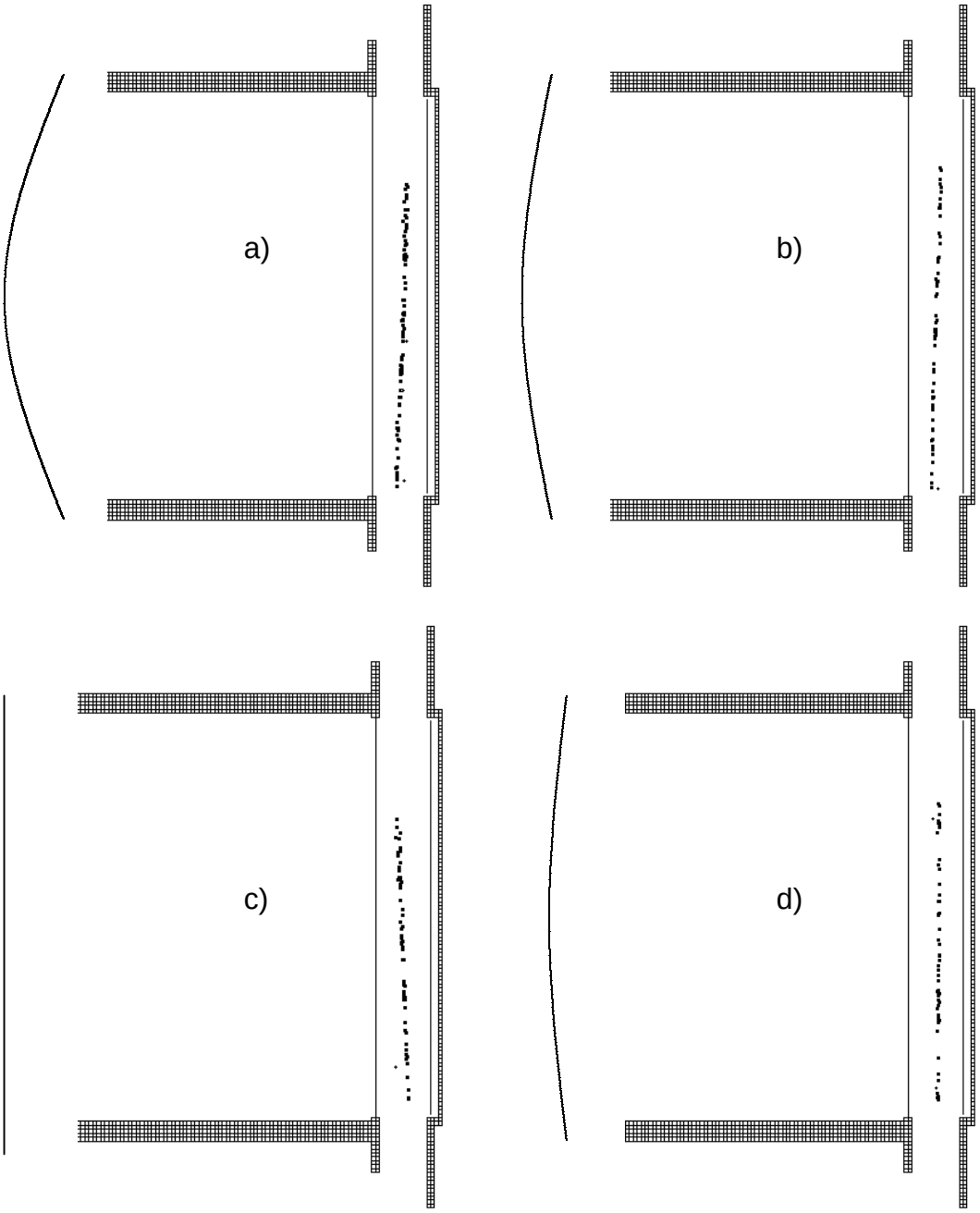

Figure 2.8. The effect of the curvature of the front grid on the mass resolution. Each frame shows simulations of typical ions reaching the detector. In a), b), and c), front grid curvatures are r = 0.8 m, r = 1.3 m, and r = ∞, respectively, and resulting ion packets are not parallel to ion detector. In d) curvature is optimized so that ion packet is parallel to ion detector, maximizing mass resolution.

impact target. Another method for protecting the detector is to use a narrower drift tube, or to include smaller apertures at both ends of the drift tube. The complication with this is that ions from the outer regions of the impact plate will have significant components of velocity perpendicular to the axis of the drift tube, and will tend to crash. This can be remedied somewhat with the ring electrode within the drift tube, which, depending on its voltage, can straighten out or scatter the ion trajectories. In any case, further work is needed on the question of detector protection.

As with any analytical instrument, sensitivity is an issue. Improvements in sensitivity can come from two directions: increasing the number of ions produced upon impact, and increasing the number of produced ions that reach the detector. Increasing ion yield of an impact can be achieved using a high-density material for the impact plate. Increasing the number of ions reaching the detector is a bit more complicated. Factors affecting total ion detection include the transmission of all grids through which the ions pass, truncation of the ion beam with apertures at the ends of the drift tube, and the general ion focusing ability of the system. However, increasing sensitivity brings benefit only to a certain point. Dust grain masses vary over several orders of magnitude. The instrument sensitivity is limited by the dynamic range, which is limited by the ion detector and electronics and centered on the range of signals produced from particles of interest. Thus the ideal sensitivity may be different depending on the range of dust particle sizes and impact velocities for a given type of dust.

2.6 Suitability for various missions

The Dusbtuster was originally designed with the hope that it would be included on the Pluto-Kuiper Express, a NASA mission to the outer solar system that was later cancelled. As such, the design was optimized with the mission objectives and limitations of the Pluto mission. Because of the severe power and mass limitations on such a spaceflight, particular attention was paid to minimizing these two properties of the Dustbuster. The low dust flux for this mission made the large impact plate essential. Also, little work was done on developing a system to protect the ion detector, since it was thought that there was relatively low risk of damaging particles and radiation based on the projected mission trajectory. Although information about the charges, masses, and velocities of particles encountered on the Pluto mission would be important, these parts of the Dustbuster had not yet been developed.

After the Pluto mission was cancelled, the engineering group and Project Manager for Deep Impact became interested in the Dustbuster. This NASA mission involved a comet rendezvous, ablation of the comet surface by a large projectile, and analysis of the resulting debris. This mission, in many respects, represented the exact opposite environment of Pluto: dust flux would be much higher, the potential for damage would be higher, and instrument mass and power were much less of a concern. The use of a low-transmission entrance grid (plate) solved these obstacles. Dust flux was reduced, but still high enough to obtain numerous samples in the few minutes the comet debris would pass by the spacecraft. The entrance plate could be designed in such a way that particles and light could be completely excluded from the detector, and no

one would complain about an instrument being lighter and lower-power than the payload limits. Measurements of particle velocity and trajectory would not be needed for the cometary debris, since the origin of particles would be known. Due to the lack of funding and other factors, the Dustbuster was not selected for Deep Impact. Interestingly, the Deep Impact spacecraft in its final form has no instrument designed to directly sample and measure the composition of the comet material, although this was identified as an important scientific objective.

We have considered trying to get the Dustbuster accepted on other missions, including Hew Horizons (the replacement Pluto mission), Solar Probe, and the recently proposed earth-orbiting dust observation satellite [14]. In terms of instrument design, minor modifications make the Dustbuster suitable for the different conditions of each mission.

2.7 Future design improvements

I have worked out several improvements to the Dustbuster subsequent to the most recent laboratory performance testing and publications. Foremost among these is a method to measure the mass and trajectory of incoming particles. In addition, small changes in the basic design geometry improve mass resolution.

The instrument originally proposed to NASA included systems to measure the velocity, angle, mass, and size of incoming dust grains. As the particle passed through several light “sheets,” the scattered light would be detected by a series of high-speed photodiodes. This information would provide the velocity and angle of the particle, and

perhaps also the size. Upon impact, piezoelectric transducers measured the impact energy, which would be used, together with the impact velocity, to determine the size of the particle. Other instruments, such as the Cassini Cosmic Dust Analyzer, uses a series of charge-sensitive grids to measure the charge and location of a particle [4]. From this information, the CDA determines the velocity and angle of the particle. The Dustbuster, as reported in recent publications, is not a standalone instrument: no method for measuring particle parameters was given. However, the Dustbuster can be outfitted with a set of components that will provide all this information and minimize instrument mass and size.

Passing a particle through a series of parallel grids wastes a great deal of space, and, depending on the geometry, reduces ion transmission. All essential information can be gathered using only two measurements of position and charge separated by sufficient time and space. However, both of these measurements do not necessarily have to be prior to impact, nor do they have to be the same type of measurement. For the Dustbuster, before the incoming particle passes through the front grid, five wires, arranged in a star, record the image current produced by the particle. The differences between the induced currents on the wires provide both the charge of the incoming particle and its location as it enters the Dustbuster. Although three wires are the minimum needed to specify unambiguously both magnitude and location of any charged particle in a plane, five wires increase the precision of the measurement. In addition, five wires provide a high level of redundancy: if one or two of the wires break or otherwise fail, the remaining three will still provide all the essential information about the particle. This provides the first set of measurements.

Upon impact of a particle with the target plate, a flash of light is given off, the intensity of which is proportional to the impact kinetic energy [15-17]. Surrounding the target plate are four photodiodes with wide-angle lenses. Similar to the charge-sensitive wires, these optical sensors provide the location and energy of the impact. Combining charge and optical data yields both the velocity and angular trajectory of the incident particle. Particle mass is calculated from velocity and kinetic energy. In addition, the light flash provides the zero point for the time-of-flight mass spectrum. The photodiodes are placed in a location that shields them from direct light that enters the instrument, although small amounts of scattered light may reach the detectors and limit sensitivity. Figure 2.9 shows the arrangement of the charge-sensitive wires and the photodiodes on the instrument, and Figure 2.10 shows an example of the signals that might be detected by this arrangement. This type of detection system does not markedly increase the size or mass of the instrument.

A second improvement is the use of a curved impact plate. A curved plate was examined as a possibility early on, but simulations of its performance proved difficult. Because of its discrete nature, SIMION is not able to realistically simulate the electric fields immediately above curved surfaces, even at the highest possible resolution. In addition, individually defining ions to originate at various locations on a “discrete-curved” surface is much more labor-intensive than individually defining them on a planar surface. Nevertheless, a concave impact surface will likely improve the instrument performance, if it is possible to mount a curved extraction grid above it. It is possible, however, that a curved impact plate will increase the risk of secondary impacts and secondary ionization.

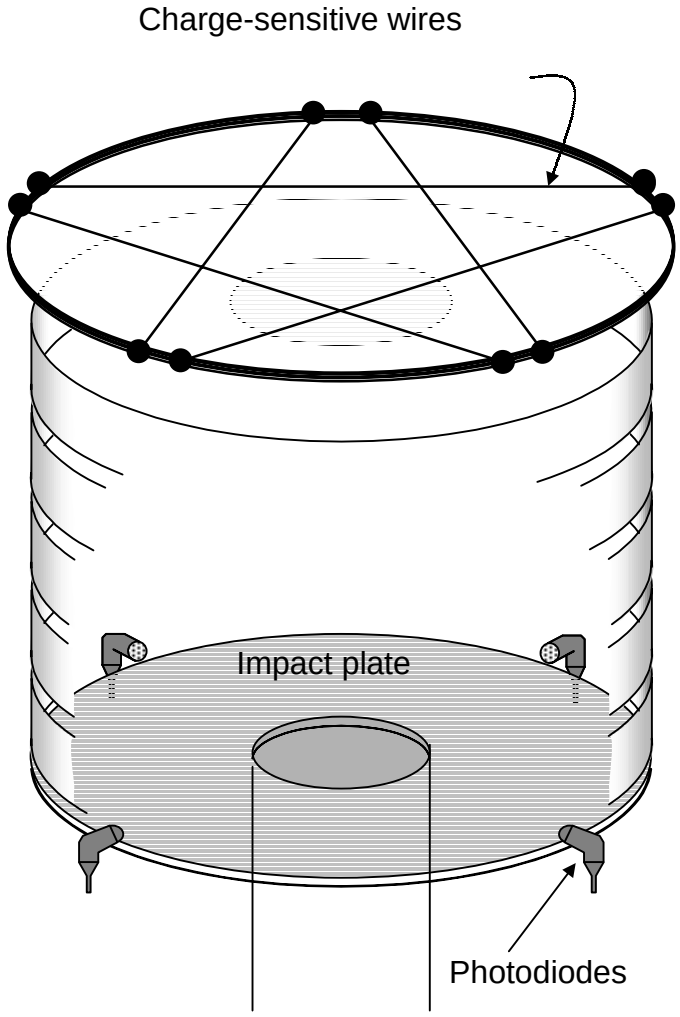

Figure 2.9. Charge-sensitive wires and photodiodes for determination of mass, velocity, charge, and trajectory of particles as they enter the Dustbuster.

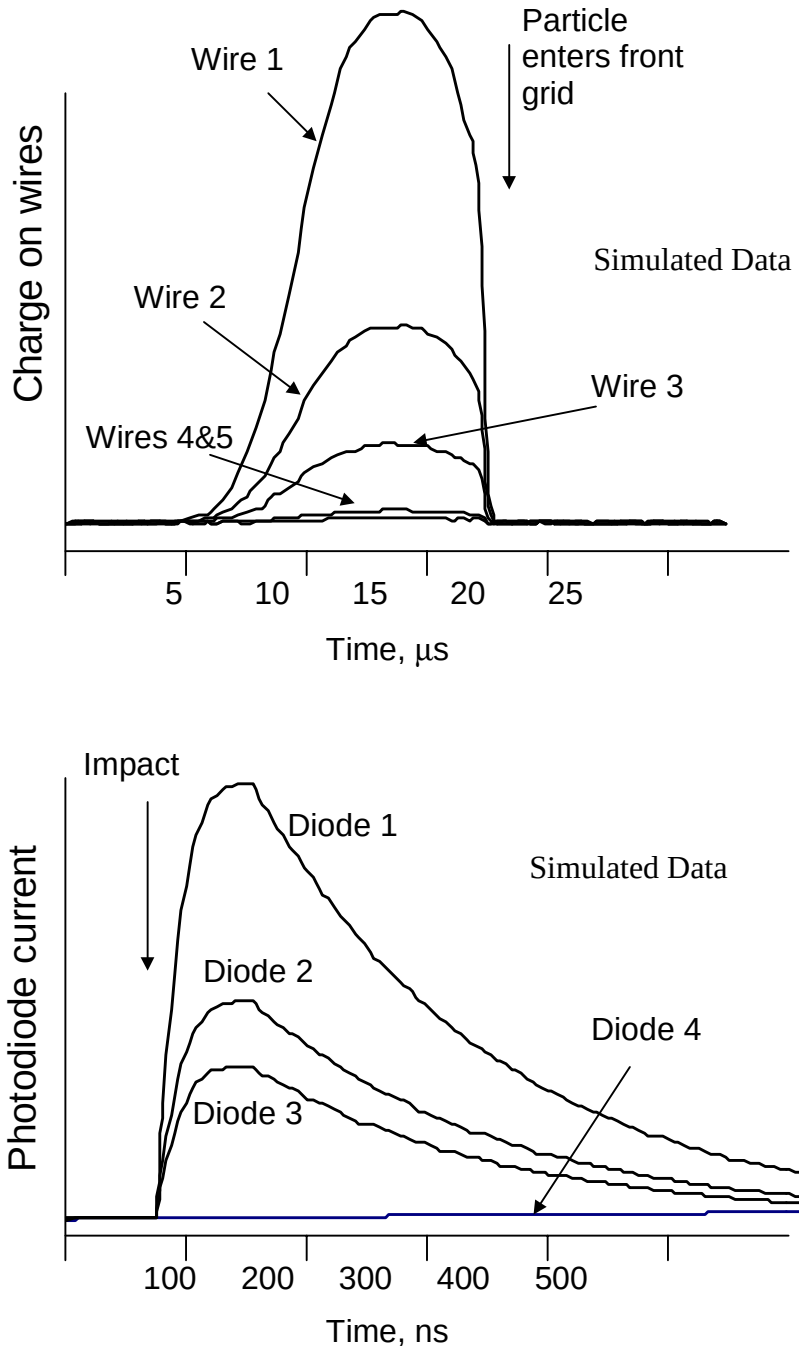

Figure 2.10. Simulated signals on charge-sensitive wires and photodiodes. Differences in signal amplitudes constrain particle location at each event. Timing between events constrains particle velocity. Signals also yield particle charge and impact kinetic energy.

In order to reduce the exposure of the ion detector, an ion reflector could be placed at the rear of the drift tube. Ions would then be deflected 90° onto the detector. The detector would thus be completely shielded from stray microparticles and incident radiation. Simulations on this possibility were not performed. Ion focusing could be an issue, and this will need to be explored in the future.

Finally, the spacing between the impact plate and extraction grid should be somewhat larger than originally designed. A distance of 4 mm seems to reduce plasma shielding, which can create a spread in the apparent times-of-birth of the ions, as well as increase the spread in the kinetic energy of the ions after extraction.

2.8 References

1. Friichtenicht, J. F., *Micrometeoroid simulation using nuclear accelerator techniques.* Nuclear Instruments and Methods, 1964. **28**: p. 70-78.
2. Dietzel, H.; Neukum, G.; Rauser, P., *Micrometeroid simulation studies on metal targets.* Journal of Geophysical Research, 1972. **77**(8): p. 1375-1395.
3. Grun, E.; Landgraf, M.; Horanyi, M.; Kissel, J.; Krüger, H.; Srama, R.; Svedhem, H.; Withnell, P., *Techniques for galactic dust measurements in the heliosphere.* Journal of Geophysical Research, 2000. **105**(A5): p. 10403-10410.
4. Ratcliff, P. R.; McDonnell, J. A. M.; Firth, J. G.; Grun, E., *The Cosmic Dust Analyzer.* J. British Interplanetary Soc., 1992. **45**(9): p. 375-380.
5. Hansen, D. O., *Mass analysis of ions produced by hypervelocity impact.* Applied Physics Letters, 1968. **13**(3): p. 89-91.

6. Austin, D. E.; Ahrens, T. J.; Beauchamp, J. L., *Dustbuster: a compact impact-ionization time-of-flight mass spectrometer for in situ analysis of cosmic dust.* Review of Scientific Instruments, 2002. **73**(1): p. 185-189.

7. Melosh, H. J., *High-velocity solid ejecta fragments from hypervelocity impacts.* Int J Impact Engng, 1987. **5**: p. 483-492.

8. Cotter, R. J., *Time-of-flight Mass Spectrometry*. 1997, Washington, D. C.: American Chemical Society. 326.

9. Friichtenicht, J. F.; Roy, N. L.; Becker, D. G. *The Cosmic Dust Analyzer: experimental evaluation of an impact ionization model*. in *International Astronomical Union Colloquium #13*. 1971. State University of New York, Albany, NY: Scientific and Technical Information Office, NASA, Washington, D.C.

10. Dahl, D. A., *SIMION 3D*. 2000, Idaho National Engineering and Environmental Laboratory: Idaho Falls, ID.

11. Ratcliff, P. R. and Allahdadi, F., *Characteristics of the plasma from a 94 km/s microparticle impact.* Advances in Space Research, 1996. **17**(12): p. (12)87-(12)91.

12. Hamabe, Y.; Kawamura, T.; Nogami, K.-i.; Ohashi, H.; Shibata, H.; Sasaki, S.; Hasegawa, S. *Development of dust analyzer with TOF mass spectrometry, abstract # 1760*. in *Lunar and Planetary Science XXX*. 1999. Lunar and Planetary Science Institute, Houston, TX.

13. Abramov, V. I.; Bandura, D. R.; Ivanov, V. P.; Sysoev, A. A., *Energy and angular characteristics of ions emitted in the impact of accelerated dust particles on a target.* Sov. Tech. Phys. Lett., 1991. **17**(3): p. 194-195.

14. Svedhem, H., *Cosmic Dune: an observatory for the study of interstellar and interplanetary dust*. 2002, European Space Agency.

15. Eichhorn, G., *Analysis of the hypervelocty impact process from impact flash measurements.* Planet. Space Sci., 1976. **24**: p. 771-781.

16. Burchell, M. J.; Kay, L.; Ratcliff, P. R., *Use of combined light flash and plasma measurements to study hypervelocity impact processes.* Advances in Space Research, 1996. **17**(12): p. (12)41-(12)45.

17. Burchell, M. J.; Cole, M. J.; Ratcliff, P. R., *Light flash and ionization from hypervelocity impacts on ice.* Icarus, 1996. **122**: p. 359-365.

Chapter 3

Laser Desorption Ionization Experiments

3.1 Introduction

The first step in demonstrating the Dustbuster's capabilities was simulating dust impacts using laser desorption ionization. The properties of ions produced using laser desorption are somewhat different than those produced in a high-velocity impact, but there are sufficient similarities to make laser desorption a useful method for evaluating instrument performance [1, 2]. For instance, the ionizing ability of light is much greater than that of an impacting particle with the same energy, while the cratering and vaporizing efficiencies are similar. As a result, the ratio of ions to neutrals in the vapor may be different between the two ionization methods. This may result in different space-charge or shielding effects. However, the initial kinetic energies of the ions are roughly the same, approximately 10-30 eV for laser desorption [3-5]. The duration of the laser pulse can be chosen so that it is similar to the duration of an impact ionization event, estimated to be a few nanoseconds [6, 7].

Laser ionization of stainless steel and copper impacts plates, as well as ionization of various mineral samples embedded in copper impact plates, were used for these

studies. The goal of laser desorption ionization experiments was demonstration of the Dustbuster capabilities, in particular mass resolution and sensitivity, and was not intended as a thorough investigation of the laser desorption ionization process. Some of these results have been reported previously [8, 9].

3.2 Experimental Setup

For laser desorption ionization studies the Dustbuster prototype, shown in Figure 3.1, was assembled using the design described in Chapter 2. The reflectron rings and the drift tube were made from type 304 stainless steel. The front grid was a knitted tungsten mesh custom ordered from Kimball Physics (Wilton, NH). Reflectron rings were spot-welded each to three support pieces, which in turn were mounted using alumina rods and spacers. In order to simplify machining and aligning, only a representative section of the impact plate and extraction grid was built, as illustrated in Figure 3.2. The instrument base, an aluminum piece, served as the center point for all mounted components, including the reflectron rings, the impact plate, extraction grid, drift tube, and support rods. The extraction grid was a 70% transmission, 333 wire-per-inch nickel electroformed grid from Buckbee-Mears St. Paul (St. Paul, MN). Attempts to spring-load the extraction grid for tautness were not successful, so the grid was mounted using conducting carbon tabs. The grids at the center of the impact plate and at the beginning of the drift tube were knitted tungsten mesh.

Using adjustable support rods the Dustbuster was mounted onto an 8” vacuum flange. Also mounted onto the flange were a 25-mm MCP detector (comprised of two

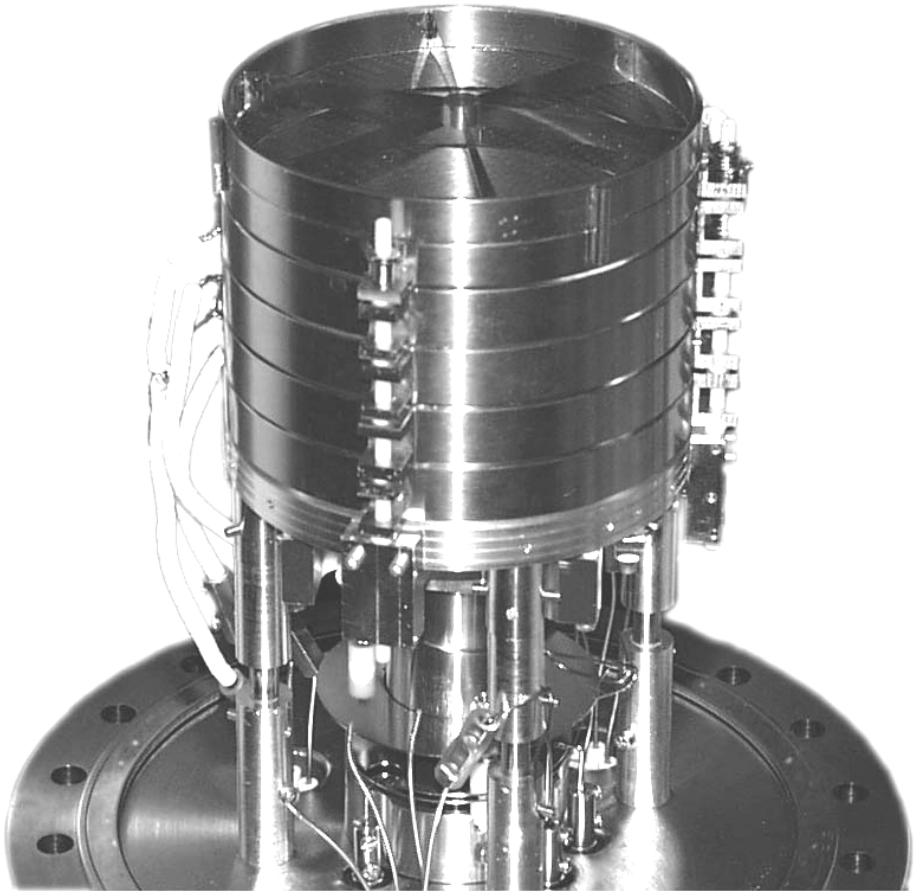

Figure 3.1. Photograph of the Dustbuster prototype used in laser experiments.

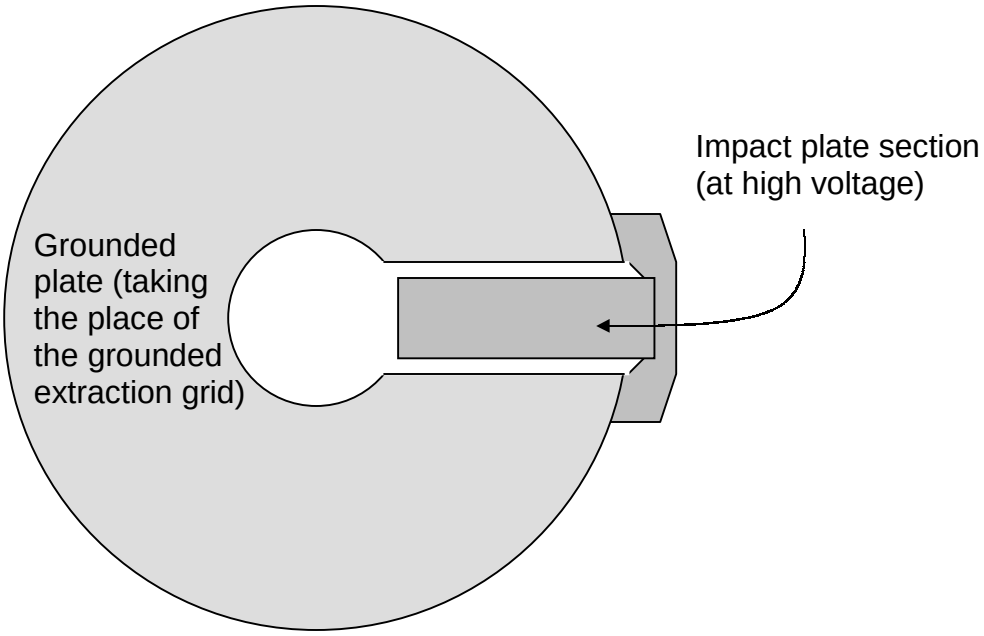

Figure 3.2. Diagram of target plate section used in laser desorption studies of the Dustbuster. Instead of mounting a large grid over the target plate, only a representative section of target plate is used, and is covered with a smaller piece of grid. The extraction grid is mounted on, and connected directly to a grounded plate, which takes the place of the rest of the extraction grid.

stacked plates) and all the electrical feedthroughs needed to provide voltages to the MCP and the Dustbuster electrodes. The mounted MCP detector, purchased from R. M. Jordan, Inc. (Grass Valley, CA) was equipped with a conical anode and impedance-matched (50Ω) connections. The output of the MCP was amplified using an EG&G Ortec fast differentiating pre-amp (model VT120C), which in turn was connected to either a 200 MHz digital oscilloscope (Tektronix) or a 150 MHz digital oscilloscope (Yokogawa).

Voltages for both the MCP plates and the Dustbuster electrodes were produced using two voltage dividers, which in turn were powered by 5 kV power supplies from Stanford Research Systems (Sunnyvale, CA). Although the MCP voltage divider was made from Caddock High Voltage Resistors (Riverside, CA), the other voltage divider was composed of common, inexpensive resistors, arranged so that the voltage across each resistor never exceeded the ratings. The voltage divider made from less expensive resistors seemed to have sufficient stability for the experiment, and no electrical discharges or other problems were observed, even at high voltages.

Figure 3.3 shows the setup for the laser desorption ionization experiments. A 337-nm nitrogen laser (Laser Science, Inc., Franklin, MA) with a pulsewidth of 4 ns was attenuated from 300 μJ to approximately 60 μJ using a variable neutral density filter, although precise laser intensity measurements were not made. Using a bi-convex lens with a focal length of 40 cm, the laser beam was focused to the smallest possible spot size, estimated to be 40 μm, resulting in a power density of 10^8-10^9 W/cm^2. The neutral density filter was varied in order to achieve the best spectra: with too little laser power, spectra showed only alkali metal ions, while too much laser power produced very noisy

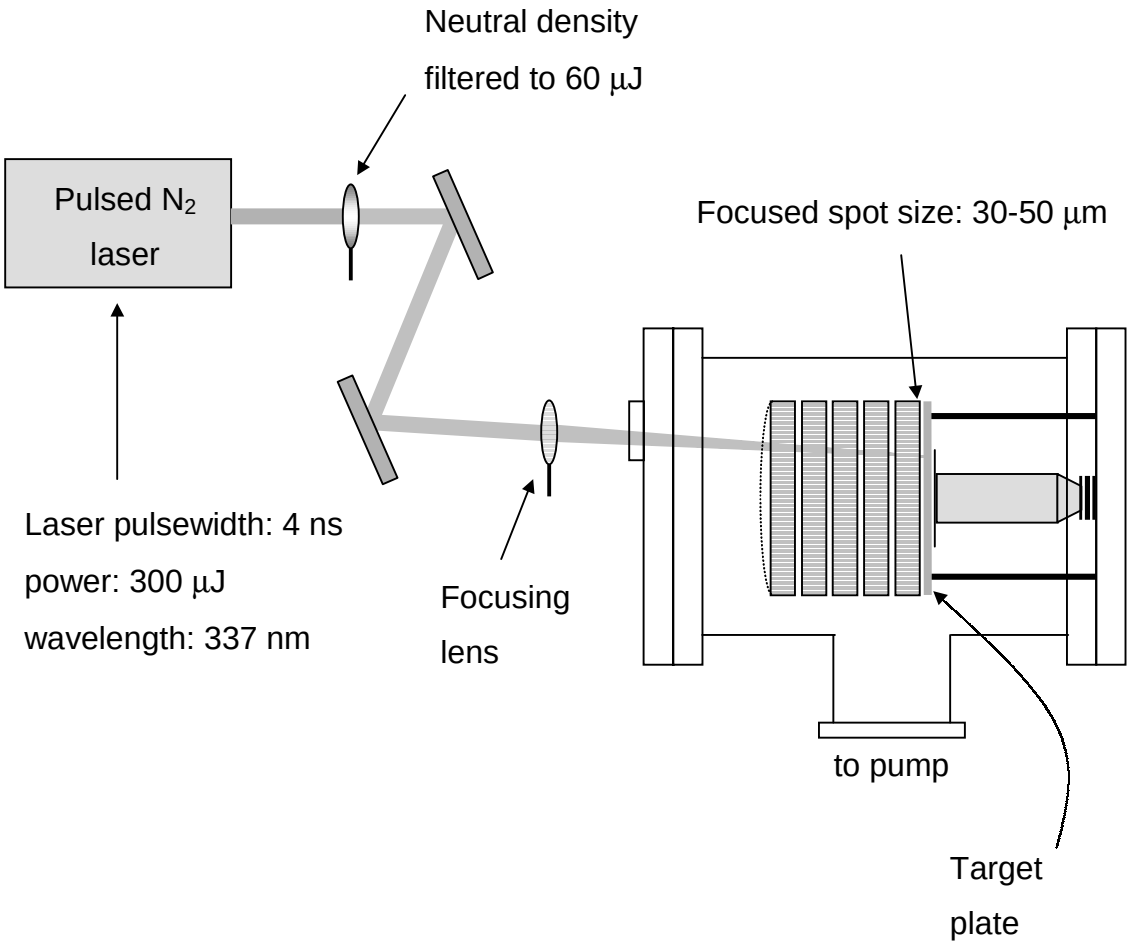

Figure 3.3. Experimental setup for laser desorption ionization experiments on the Dustbuster. Mineral samples were embedded in target plate for some experiments; for others the target plate was made of copper or stainless steel, which acted as the sample.

spectra. At the laser power used in these experiments nearly all species observed were singly charged atomic ions. The Dustbuster was inside a vacuum chamber, which was evacuated by turbopump to below 10^{-7} torr. The position of the focused laser spot was varied over the impact plate in order to simulate impacts at different radii from the instrument axis. However, a careful measurement of spot position was not made. In addition, for mineral samples the laser spot location was limited to the size of the mounted sample, about 5 mm.

For the first laser experiments representative target plate sections were made from type 304 stainless steel and copper. The purity of the copper was not known, although it was probably oxygen-free high-conductivity copper. The steel and copper surfaces were sanded until shiny with 600-grit silicon carbide sandpaper, then degreased and sonicated in HPLC grade methanol. A sputtering source was not available for further surface improvement. In later experiments, mineral samples were mounted onto the copper target plate. Minerals were obtained from the collection of George R. Rossman, Professor of Minerology, Division of Geological and Planetary Sciences, California Institute of Technology, Pasadena, CA. Minerals studied included chalcopyrite ($FeCuS_2$), dolomite ($CaMg(CO_3)_2$), olivine ($(Mg,Fe)_2SiO_4$), and chlorite ($(Mg,Fe)_5(Al,Fe)_2Si_3O_{10}(OH)_8$). For all minerals but dolomite, freshly-cleaved samples, roughly 0.1-0.3 mm thick and 5 mm in diameter, were mounted into recessed holes in the copper plate using adhesive conducting carbon tabs (routinely used for STM work). Of these minerals, only chalcopyrite is electrically conducting. In the cases of the other minerals, the electrical potential at the ionizing surface was not well defined. The depth of the recess in the copper plate corresponded to the thickness of the samples, so that the

mineral surfaces were nearly coplanar with the surface of the copper plate. The dolomite sample did not cleave into a thin piece, but was easily crushed into a powder, which was then pressed onto the adhesive carbon tab.

3.3 Results and Discussion

All laser desorption ionization experiments involved extraction and analysis of positive ions only. Spectra from laser desorption of the stainless steel impact plate were printed out using the Yokagawa oscilloscope printer, but were not recorded in a digital format. Figure 3.4 shows two representative spectra from the steel plate. Note that these are time-domain spectra, so mass scales quadratically, and that the domain is inverted. Ions of sodium and potassium, common contaminants both in laser- and impact-generated ions [6, 10], were observed in all spectra. A peak at m/z = 52, corresponding to $^{52}Cr^{+}$, the principal isotope of chromium (84% of total Cr), was present in all spectra. Type 304 stainless steel is typically 18-20% chromium. The other three stable isotopes of chromium were not clearly observed. Aluminum ion peaks appeared in most of the spectra, but their source is unknown. Neither iron nor the other components of stainless steel were observed, although two spectra showed an unusual group of ion peaks including masses 12, 13, 14, and 15. A few spectra showed small peaks corresponding to hydrogen ions. Appendix A lists all stable, naturally occurring isotopes of all elements observed in the spectra of Chapters 3-5, and includes the masses and natural isotope abundances for each isotope. Accurate estimations of mass resolution were not possible with the steel spectra because of their recorded format.

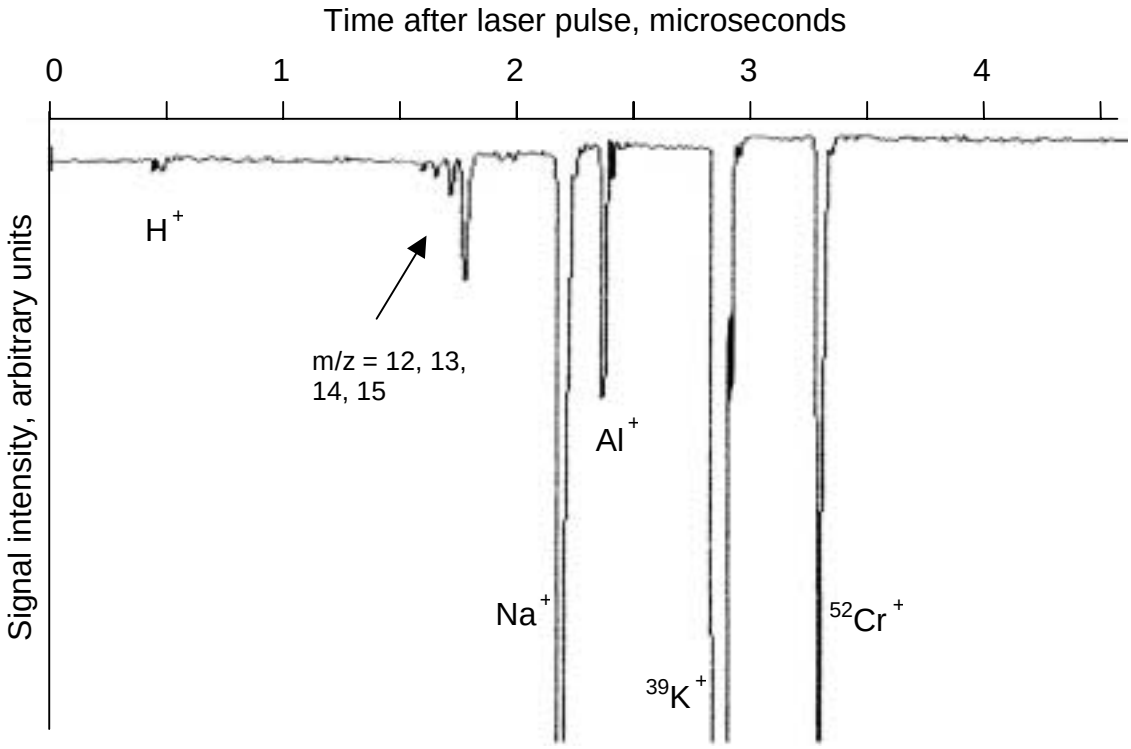

Figure 3.4. Typical laser desorption ionization spectra using a stainless steel target plate. Note that the abscissa is in units of time; mass is not linear on this scale.

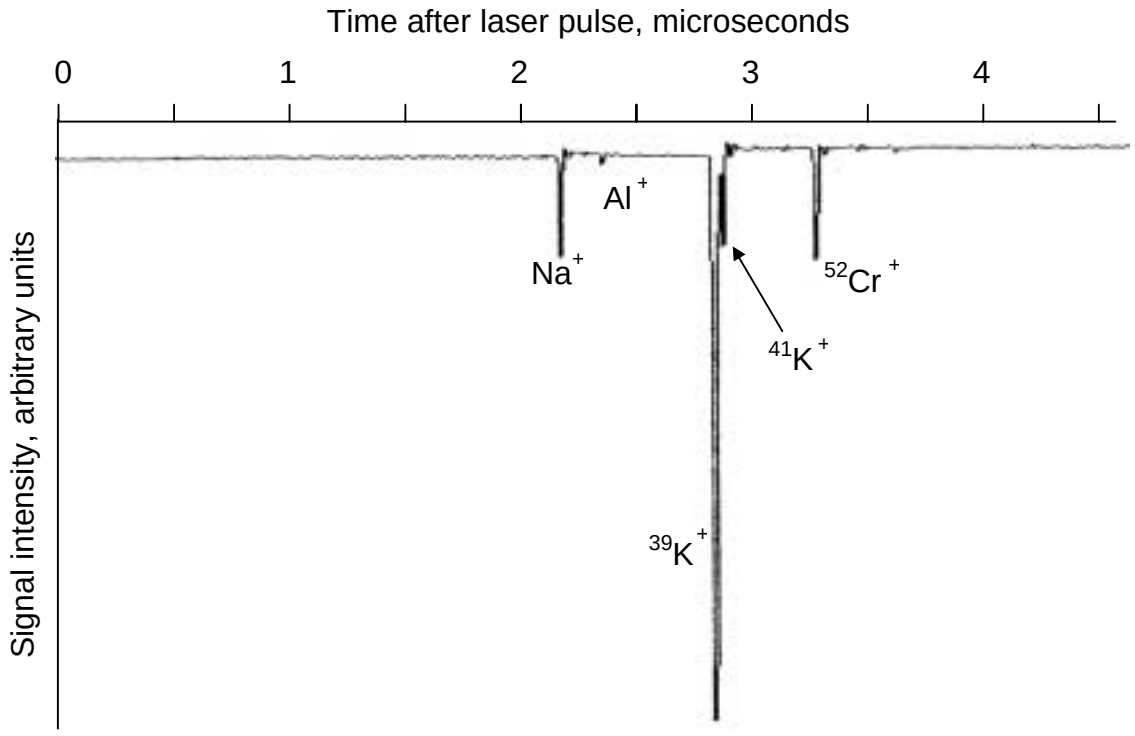

Figure 3.4, continued. Typical laser desorption ionization spectra using a stainless steel target plate. Note that the abscissa is in units of time; mass is not linear on this scale.

Figure 3.5 shows a laser-desorption time-of-flight mass spectrum of the copper target plate. This spectrum is the average of 12 single-shot spectra. Both isotopes of copper are present and completely resolved. Copper cluster ions were also detected. Figure 3.6 shows two representative single-shot spectra using the copper plate. In the averaged spectrum the $^{63}Cu^{+}$ peak has a mass resolution ($m/\Delta m$) of 100. The mass resolution of copper peaks in the individual (single-shot) spectra ranged from 83-150, with an average of 116 and standard deviation of 24. The differences in resolution between shots may be caused by inhomogeneities in the laser beam or the copper surface, or by space-charge effects. The copper isotope ratios, $^{63}Cu/^{65}Cu$, which were measured for each copper spectrum, ranged from 2.3 to 9.3, with an average of 5.4 and standard deviation of 2.45. The value of this ratio should be 2.24 based on natural isotope abundances (see Appendix A). In each case the $^{65}Cu^{+}$ peak is smaller than expected. The small $^{65}Cu^{+}$ peaks appear to be caused by signal overshoot and the slow recovery of the microchannel plate detector.

Figure 3.7 shows an average of 9 spectra from the chalcopyrite ($FeCuS_2$) sample. Figure 3.8 shows two single-shot spectra typical of those observed for chalcopyrite. The chalcopyrite spectra showed a great deal of variability, especially in the relative amounts of copper and iron detected. Other peaks observed include hydrogen, lithium, sodium, aluminum, and potassium. Ions of the principal isotopes of iron, ^{54}Fe and ^{56}Fe, and of copper, ^{63}Cu and ^{65}Cu appeared in most spectra. However, the isotope ratios vary significantly from expected values. The $^{56}Fe/^{54}Fe$ ratio ranged from 9 to 62, although in the latter case the $^{54}Fe^{+}$ peak was small enough to be affected by noise. The average $^{56}Fe/^{54}Fe$ ratio was 16.5, which is close to the expected value of 15.68, based on natural

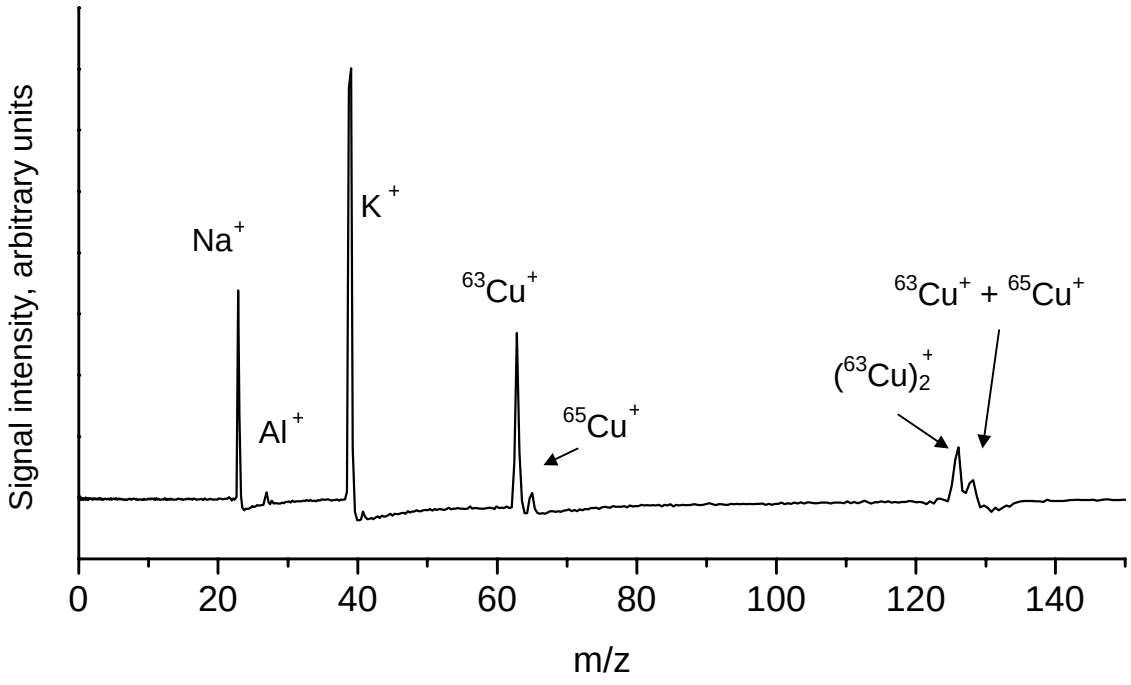

Figure 3.5. Average of 12 laser desorption spectra in which the target plate is copper. Note the presence of both isotopes of copper, as well as the singly charged copper dimer.

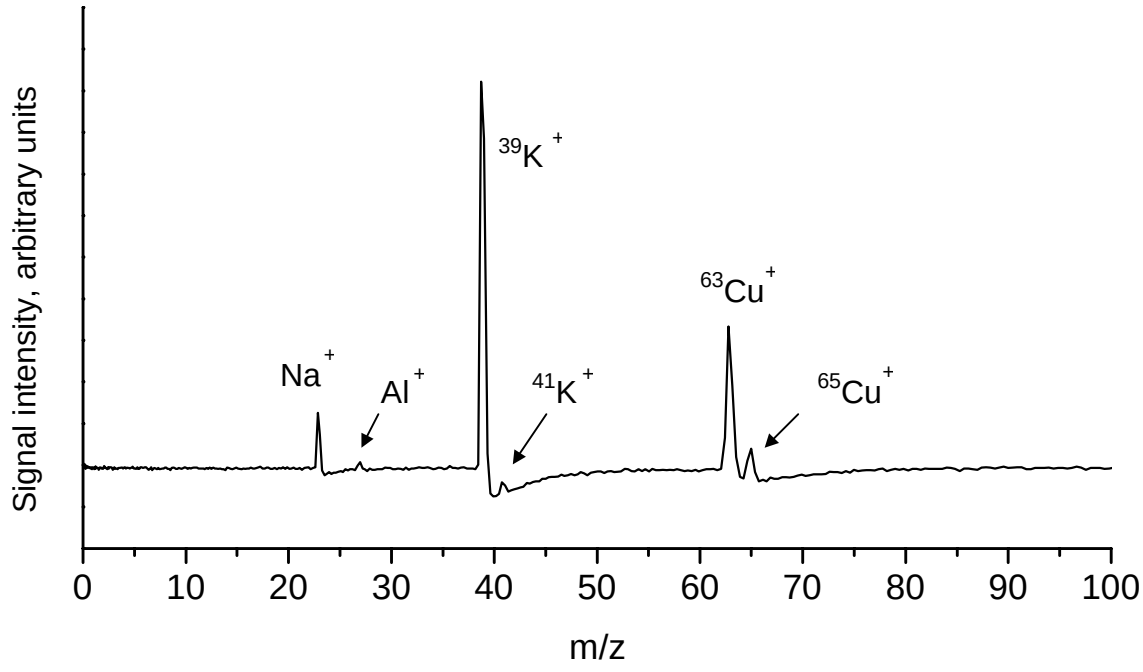

Figure 3.6. Typical single-shot laser desorption ionization spectra of copper target plate.

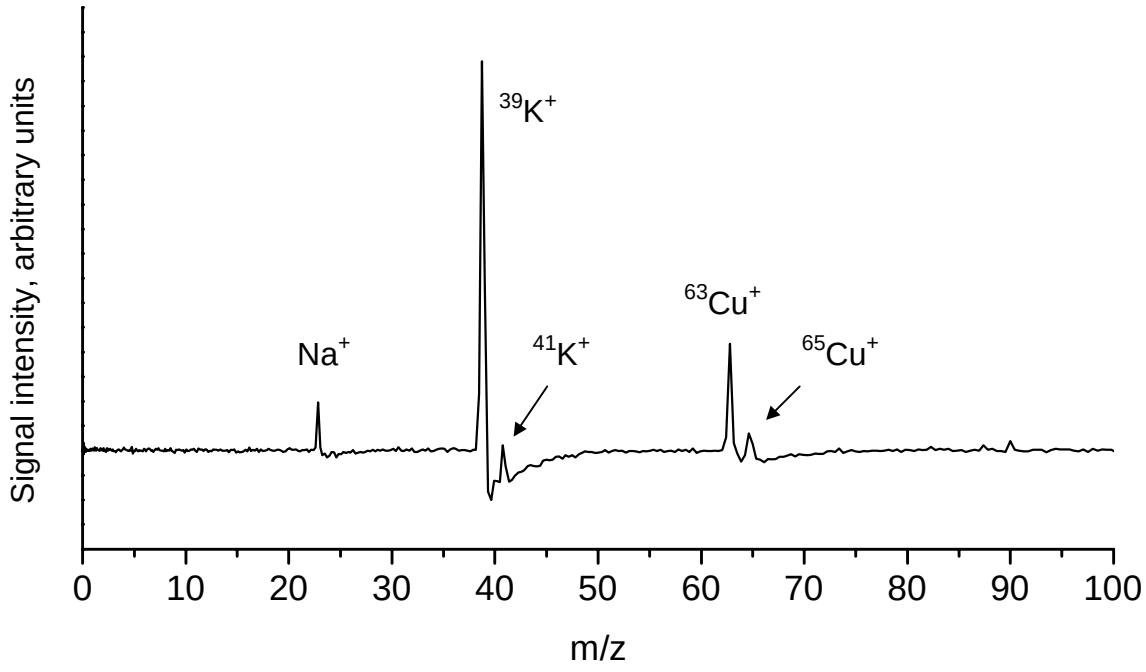

Figure 3.6, continued. Typical single-shot laser desorption ionization spectra of copper target plate.

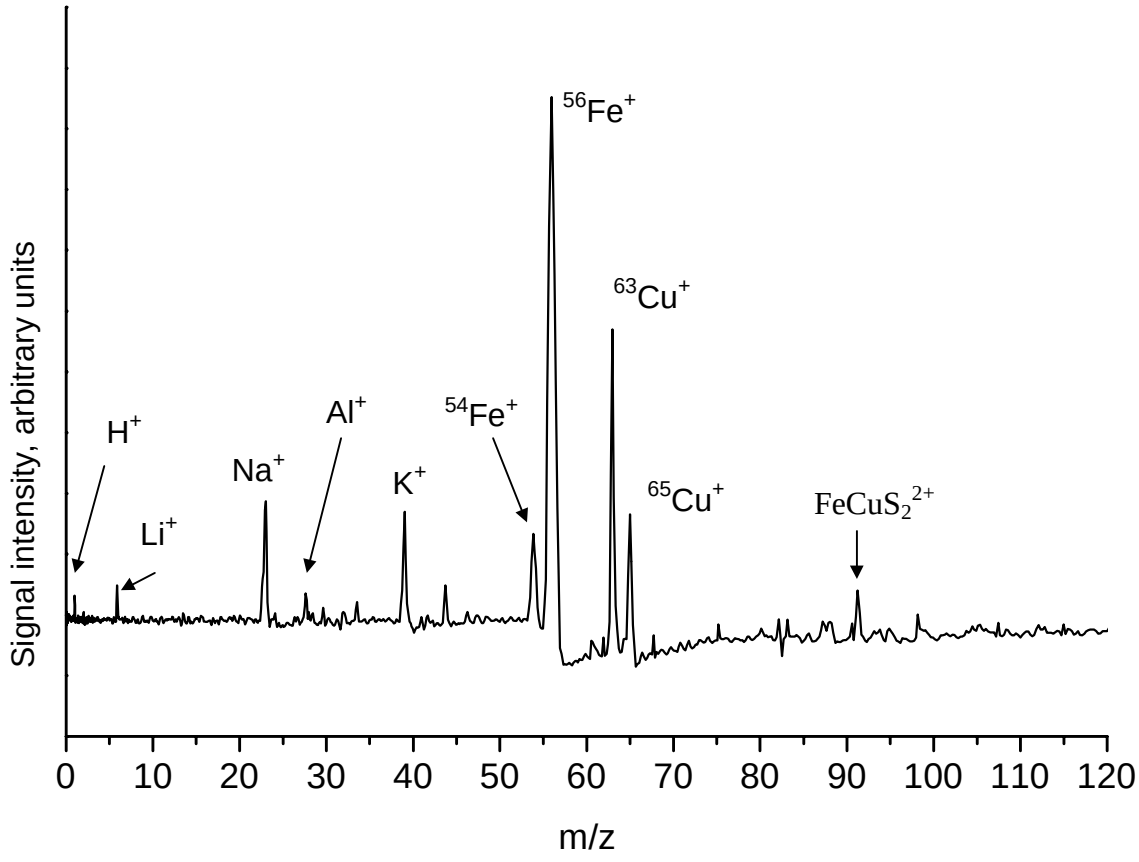

Figure 3.7. Average of nine laser desorption ionization spectra of chalcopyrite, $FeCuS_2$, mounted on target plate.

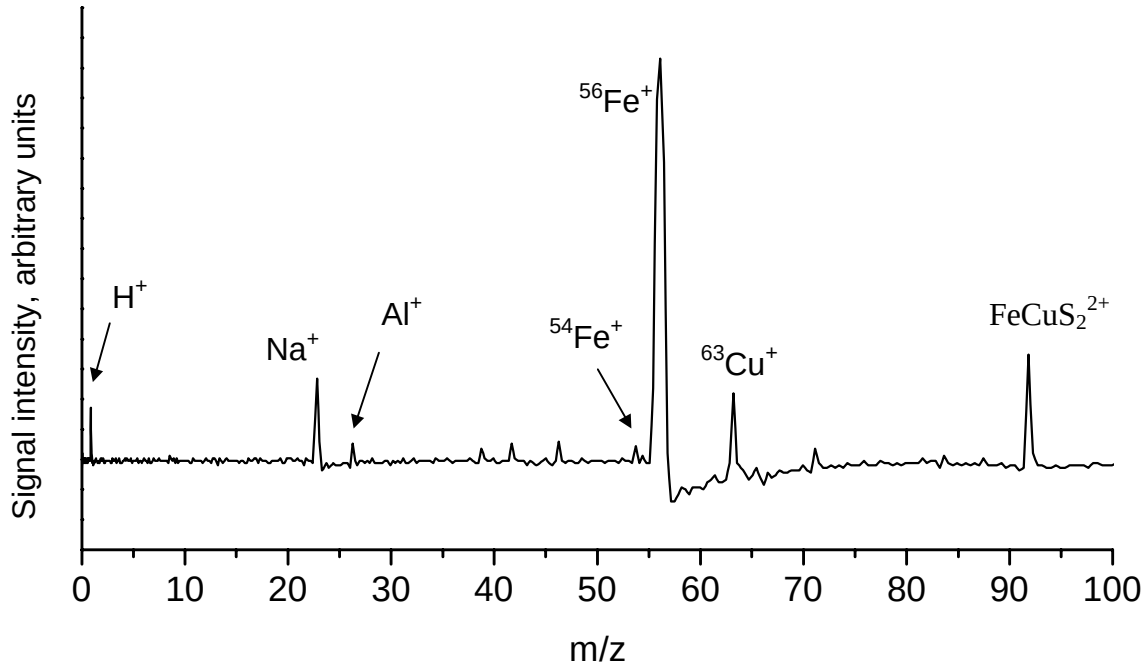

Figure 3.8. Typical single-shot laser desorption ionization spectra of chalcopyrite, $FeCuS_2$.

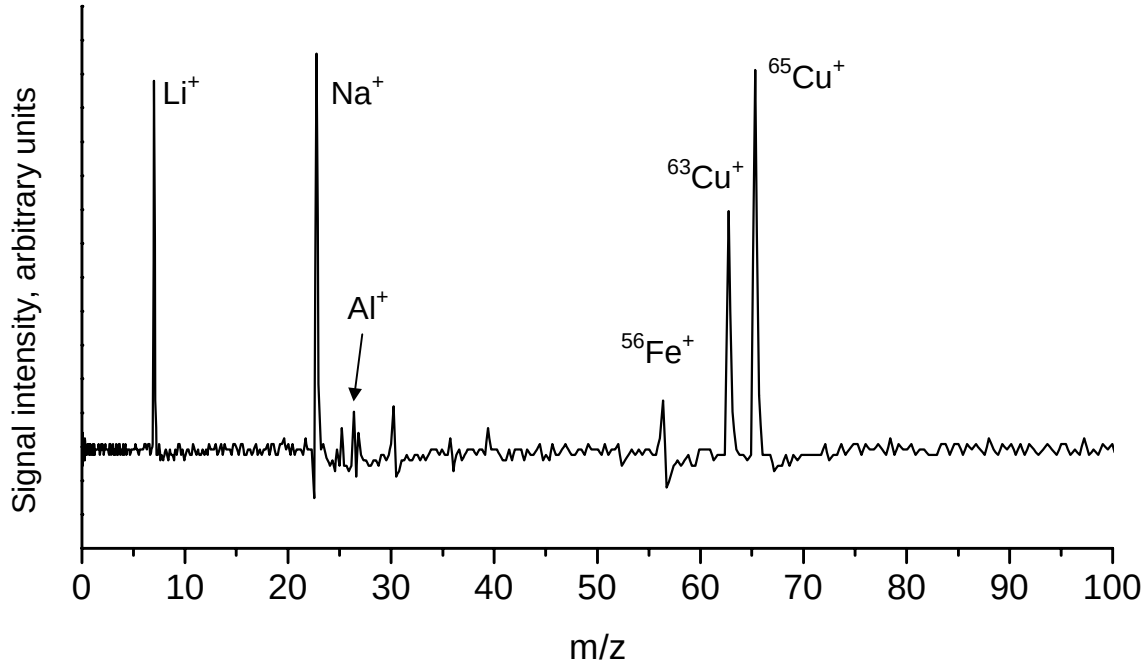

Figure 3.8, continued. Typical single-shot laser desorption ionization spectra of chalcopyrite, $FeCuS_2$.

isotope abundances. The $^{63}Cu/^{65}Cu$ ratio ranged from 0.65 to 3.46. The average $^{63}Cu/^{65}Cu$ ratio was 2.03, close to the expected value of 2.24. In some spectra with weak iron and/or copper signals, the expected intensities of minor isotopes were similar to the intensity of noise peaks, and could not be accurately measured. Chalcopyrite typically does not contain elemental impurities, except occasional zinc [11].

Figure 3.9 shows two typical single-shot spectra from dolomite, $CaMg(CO_3)_2$. The principal isotope of calcium, ^{40}Ca, appears in most spectra. Magnesium is less common. Sodium and potassium appear in most spectra. A peak at 72 appears in most spectra, and could be a species such as CaO_2^+. Some dolomites have impurities of iron, magnesium, or zinc [12].

The chlorites are layered minerals resembling micas. A typical chemical formula for chlorite is $(Mg,Fe)_5(Al,Fe)_2Si_3O_{10}(OH)_8$. The name chlorite is from Greek *chloros*, green, and the mineral does not contain chlorine. Chlorite often contains impurities and trace elements, including Mn, Cr, Ni, Ti, Ca, Na, and K [11]. Figure 3.10 shows two typical single-shot spectra from chlorite. Hydrogen, lithium, and silicon ions appear in some spectra. Various other peaks, some of which are not identifiable, appear sporadically. Most chlorite spectra show several strong, irreproducible peaks at high masses (>100), which are not shown in Figure 3.10. Iron and magnesium ion peaks did not appear at all, and aluminum ions showed up in only one spectrum. The chlorite spectra showed a surprising amount of variation.

Olivine minerals show a great deal of compositional variation, and frequently have impurities of titanium, aluminum, manganese, calcium, sodium, potassium, nickel, chromium, and water [13]. Figure 3.11 shows four typical spectra from olivine,

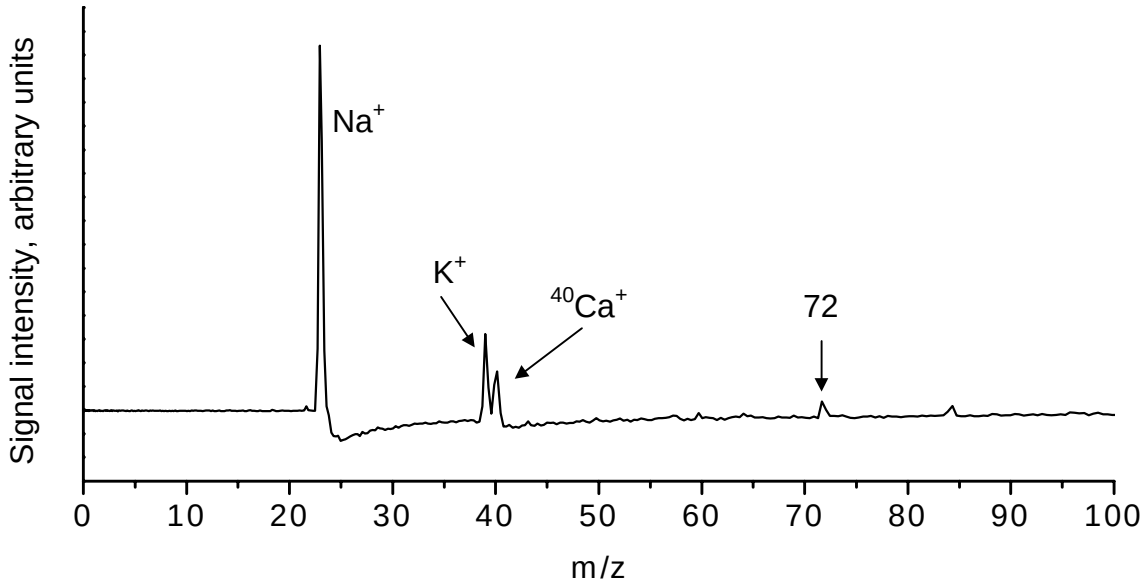

Figure 3.9. Typical single-shot laser desorption ionization spectra of dolomite, $CaMg(CO_3)_2$.

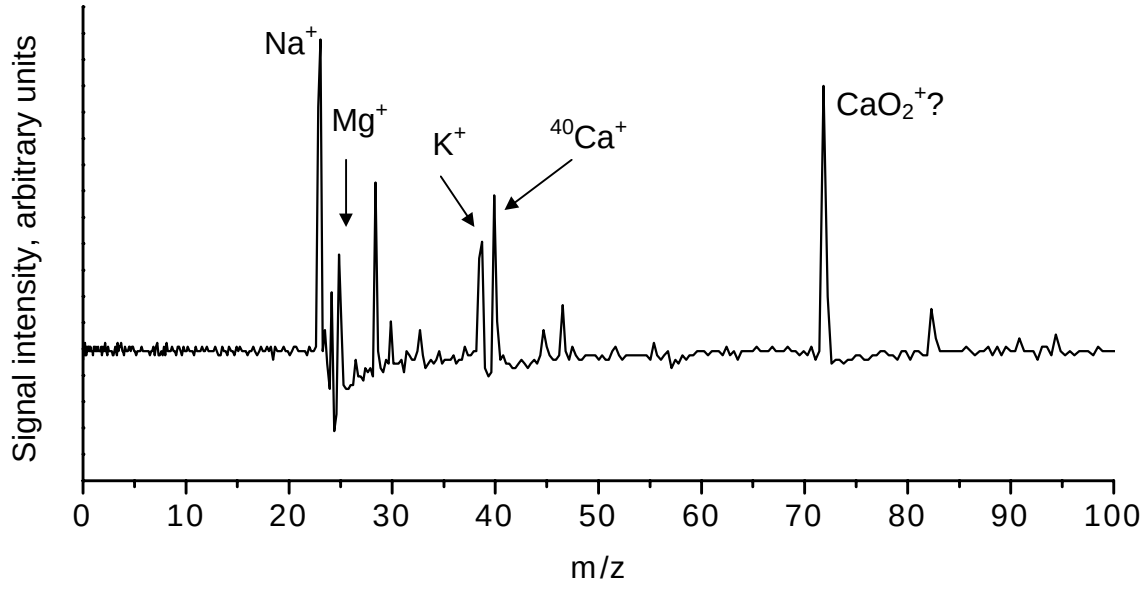

Figure 3.9, continued. Typical single-shot laser desorption ionization spectra of dolomite, $CaMg(CO_3)_2$.

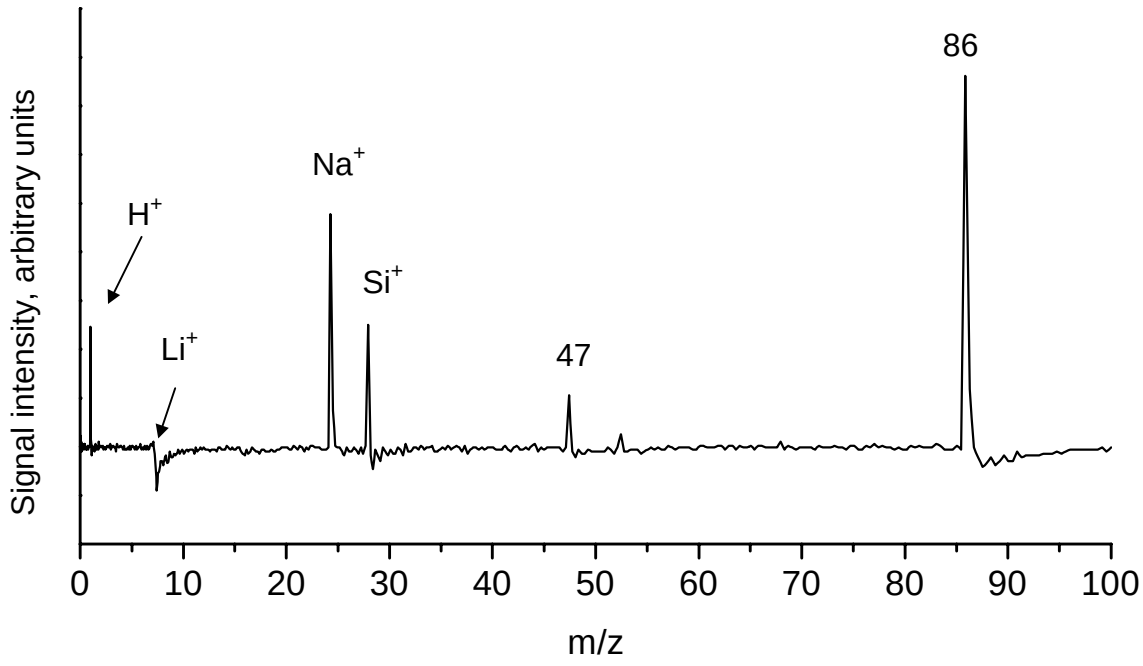

Figure 3.10. Typical single-shot laser desorption ionization spectra of chlorite, $(Mg,Fe)_5(Al,Fe)_2Si_3O_{10}(OH)_8$.

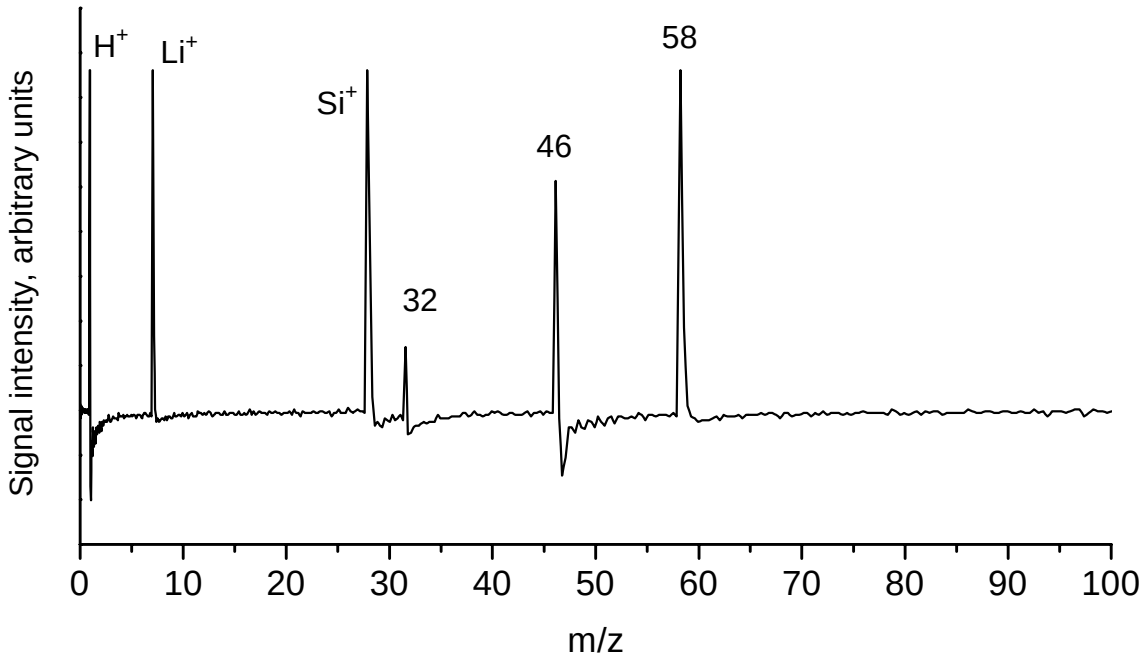

Figure 3.10, continued. Typical single-shot laser desorption ionization spectra of chlorite, $(Mg,Fe)_5(Al,Fe)_2Si_3O_{10}(OH)_8$.

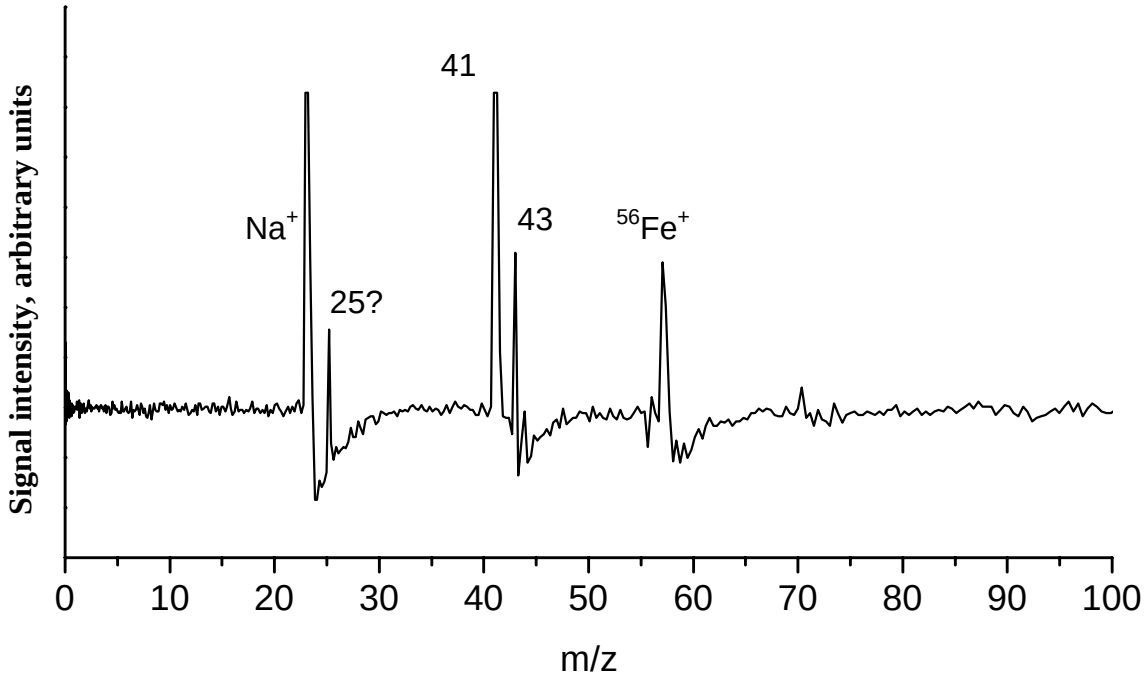

Figure 3.11. Typical single-shot laser desorption ionization spectra of olivine, $(Mg,Fe)_2SiO_4$.

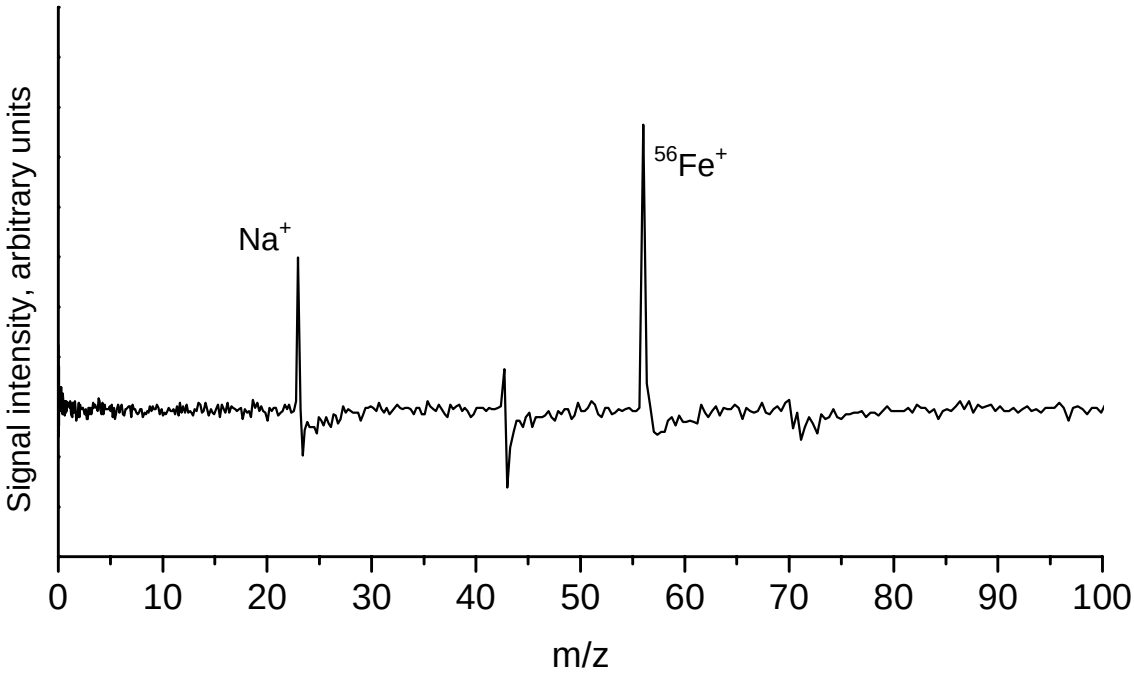

Figure 3.11, continued. Typical single-shot laser desorption ionization spectra of olivine, $(Mg,Fe)_2SiO_4$.

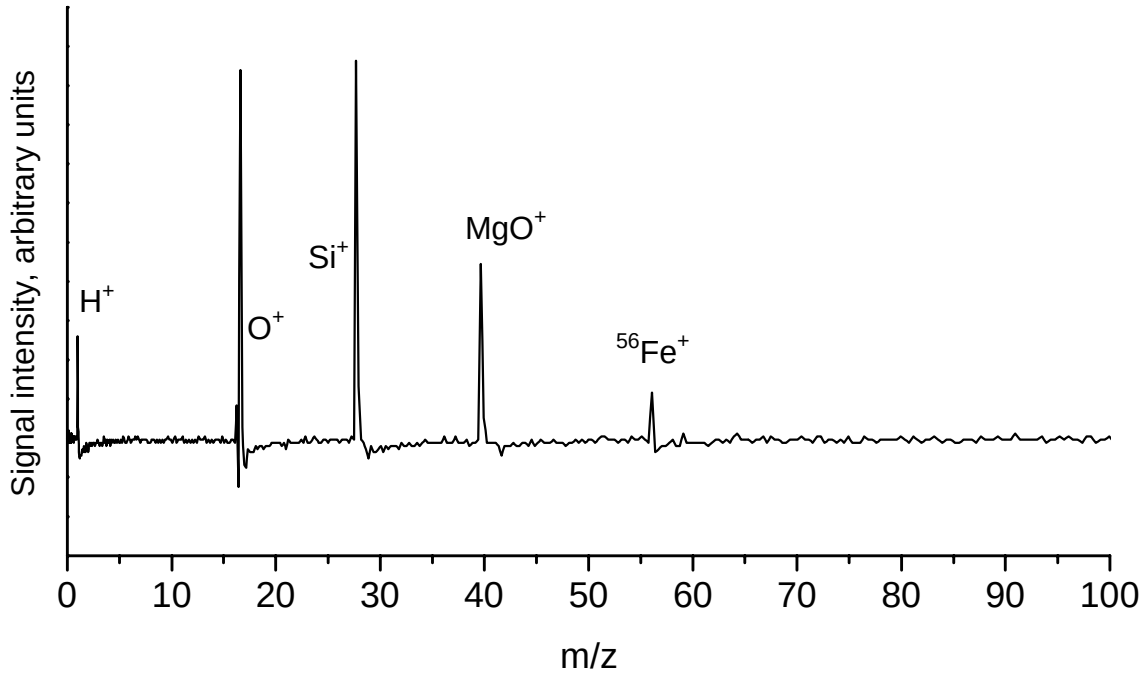

Figure 3.11, continued. Typical single-shot laser desorption ionization spectra of olivine, $(Mg,Fe)_2SiO_4$.

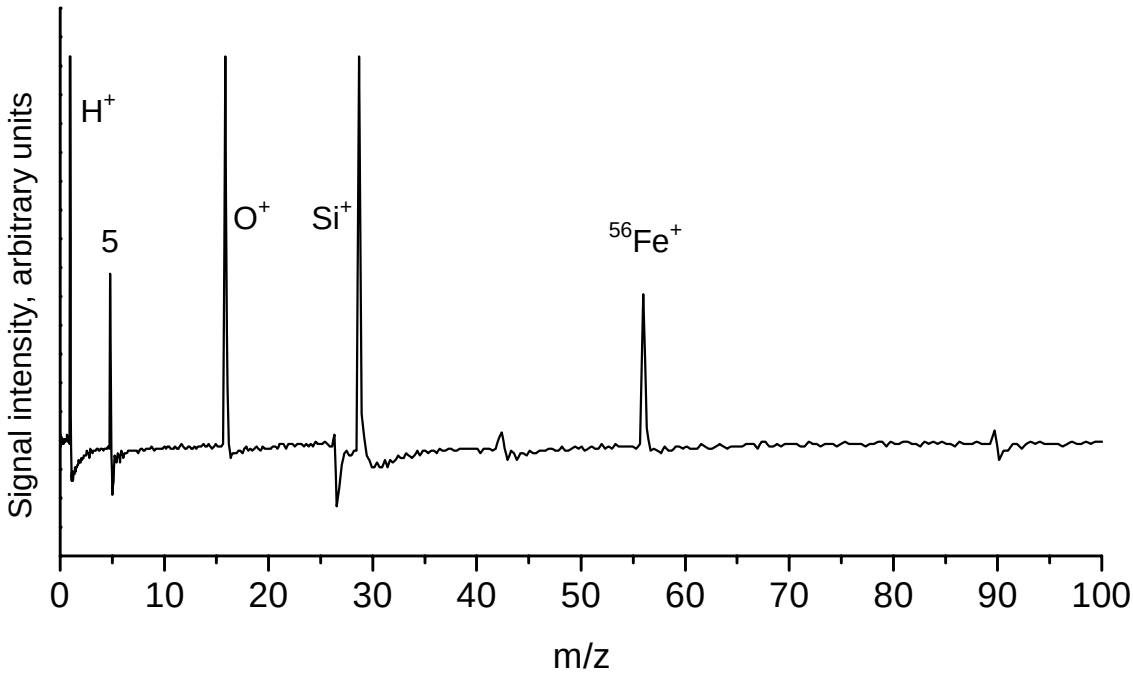

Figure 3.11, continued. Typical single-shot laser desorption ionization spectra of olivine, $(Mg,Fe)_2SiO_4$.

$(Mg,Fe)_2SiO_4$. These spectra also show large variability. Hydrogen, sodium, and silicon ions appear in several spectra each. Oxygen ions are present in some spectra. Although magnesium peaks are absent, iron (^{56}Fe) appears in all spectra. ^{54}Fe is not visible in any spectra. It is possible that the peak at m/z = 56 is something other than iron, such as MgO_2^+ or CaO^+, which might explain the lack of a peak at m/z = 54. Even more unusual is a peak at m/z = 5 which appeared in one spectrum. Because ions originate on an insulating surface with a poorly defined electrical potential, flight times may be skewed, and the normal calibration may not be appropriate. Mass resolution in all the mineral spectra was sufficiently high to resolve isotopes of elements present.

Some of these minerals are semitransparent to visible light, and may be partially transparent to the wavelength of laser used in this experiment. As a result, absorption, ablation, and ionization may be highly inhomogeneous. It is likely that the laser energy is preferentially absorbed by defects and trace metals near the surface of the mineral grains. This may explain the variation and unusual peaks in these spectra, as well as the lack of such peaks as magnesium. Chlorite and olivine, which had the most variation and peculiarities, are also the most transparent. Chalcopyrite is completely opaque to visible light, and dolomite is somewhat opaque.

Isotope ratios varied considerably between shots for each sample examined. In many spectra with iron, $^{54}Fe^+$ was not visible, although it should have been 6% the intensity of the $^{56}Fe^+$ peak. This is clearly not caused by detector saturation because the attenuated peak precedes the large peak in time, but the cause of the anomaly is not known. Averaging several spectra reduces the magnitude of the isotope error for iron, so perhaps the minor isotope peak is simply too small to be seen above the noise in

single-shot spectra. Using an ion detector with a greater dynamic range and sensitivity, such as improved microchannel plates or continuous dynode detectors, will reduce this problem for single-shot spectra. In addition, sources of noise can be identified and reduced.

Laser desorption ionization experiments demonstrate several aspects of the Dustbuster capabilities. Mass resolution is sufficiently high to distinguish isotopes of light elements, at least through copper. Sensitivity is high enough to detect ion signals, although minor isotopes may be difficult to measure. In general, the design seems to work as intended.

3.4 References

1. Kissel, J. and Krueger, F. R., *Ion formation by impact of fast dust particles and comparison with related techniques.* Applied Physics A: Solids and Surfaces, 1987. **42**: p. 69-85.
2. Jyoti, G.; Gupta, S. C.; Ahrens, T. J.; Kossakovski, D.; Beauchamp, J. L., *Mass spectrometer calibration of high velocity impact ionization based cosmic dust analyzer.* International Journal of Impact Engineering, 1999. **23**: p. 401-408.
3. Amoruso, S.; Berardi, V.; Bruzzese, R.; Spinelli, N.; Wang, X., *Kinetic energy distribution of ions in the laser ablation of copper targets.* Applied Surface Science, 1998. **127-129**: p. 953-958.
4. Phipps, C. R. and Dreyfus, R. W., *The High Laser Irradiance Regime: A. Laser Ablation and Plasma Formation*, in *Laser Ionization Mass Analysis*, Vertes, A.; Gijbels, R.; Adams, F., Editors. 1993, Wiley. p. 369-431.

5. Vertes, A.; Juhasz, P.; Jani, P.; Czitrovszky, A., *Kinetic energy distribution of ions generated by laser ionization sources.* International Journal of Mass Spectrometry and Ion Processes, 1988. **83**: p. 45-70.

6. Hansen, D. O., *Mass analysis of ions produced by hypervelocity impact.* Applied Physics Letters, 1968. **13**(3): p. 89-91.

7. Roy, N. L., *Research Investigations of the Physical Interactions and Phenomena Associated with Hypervelocity Sub-micron Particles*. 1975, TRW Systems Group: Redondo Beach, CA. p. 67.

8. Austin, D. E.; Ahrens, T. J.; Beauchamp, J. L., *Dustbuster: a new generation impact-ionization time-of-flight mass spectrometer for in situ analysis of cosmic dust.* Bulletin of the American Astronomical Society, 2000. **32**(3): p. 1043.

9. Austin, D. E.; Ahrens, T. J.; Beauchamp, J. L., *Dustbuster: a compact impact-ionization time-of-flight mass spectrometer for in situ analysis of cosmic dust.* Review of Scientific Instruments, 2002. **73**(1): p. 185-189.

10. Auer, S. and Sitte, K., *Detection technique for micrometeoroids using impact ionization.* Earth and Planetary Science Letters, 1968. **4**: p. 178-183.

11. Deer, W. A.; Howie, R. A.; Zussman, J., *Rock-forming Minerals.* Vol. 3: Sheet Silicates. 1962, New York: Wiley.

12. Chang, L. L. Y.; Howie, R. A.; Zussman, J., *Rock-forming Minerals*. Vol. 5B: Non-silicates: Sulphides, Carbonates, Phosphates, Halides. 1996, Essex: Longman Group.

13. Chang, L. L. Y.; Howie, R. A.; Zussman, J., *Rock-forming Minerals*. Vol. 1A: Orthosilicates. 1982, London: Longman.

Chapter 4

Hypervelocity Microparticle Impact Experiments

4.1 Simulating cosmic dust impacts in the lab: accelerating microparticles

A thorough understanding of the impact ionization process is essential in developing and testing new cosmic dust mass spectrometers, as well as interpreting the results from previous instruments. Controlled studies of impact-related phenomena require the ability to produce high-velocity particles and projectiles in the laboratory. Methods for producing hypervelocity (>1-2 km/s) projectiles began to be developed in the 1950s in both national defense and space-related programs. Defense-related efforts included exploring the possibility of knocking enemy missiles off course by bombardment with large numbers of small, fast particles launched from a satellite [1]. Of concern to the emerging space program was the possibility that spacecraft would suffer damage from continual impacts of dust grains. Another question was whether the lunar surface would be sufficiently solid to land (and relaunch) a manned spacecraft, and whether spacesuits could withstand impacts without being punctured.

In 1955 Fred Whipple and George Gamow recommended that the United States develop three promising methods of producing hypervelocity particles: the light gas gun,

shaped charge jets, and electromagnetic guns [1]. Explosive and magnetic methods were also studied in this context. However, all of these methods had limitations that adversely affected the ability to carefully research the impact phenomenon as it related to microparticles. For instance, each method typically produced numerous hypervelocity particles simultaneously, hindering study of individual impacts. In addition, these methods could not produce particles with velocities greater than approximately 10 km/s.

Direct electrical acceleration of charged particles was also considered for development. A major limitation is that, regardless of the charging mechanism used, particles will all have different mass-to-charge ratios, precluding the possibility of using cyclic or multi-stage accelerators such as synchrotrons or linacs. Charged microparticle acceleration requires a single-stage electrostatic system powered by a very high voltage. For a conducting particle with mass in kilograms, m, and charge in Coulombs, q, accelerated through a voltage, V, the particle kinetic energy is

$$KE = \frac{1}{2}mv^2 = qV \tag{1}$$

and its velocity, in m/s, is

$$v = \sqrt{\frac{2qV}{m}}\,. \tag{2}$$

Of course, the total amount of negative charge on a particle is limited by the electron field emission limit, about 10^9 V/m. The total amount of positive charge on a particle is limited by the ion field emission limit, roughly 10^{10} V/m [2]. The other limiting factor in obtaining high velocities is the availability of high (MV range) voltage sources.

In 1960 Shelton [2] developed and demonstrated an electrostatic accelerator capable of delivering individual, high-velocity, highly charged micron-sized metal particles. Dust particles, such as reduced iron carbonyl, became highly charged upon contact with a charged needle. They were then accelerated through 100 kV. Shelton also constructed a series of induced-charge sensors to measure the velocity and charge of accelerated particles. Friichtenicht [3] used the principles of Shelton's instrument and constructed a larger dust accelerator with a 2 MV van de Graaff accelerator as the voltage supply. Friichtenicht observed particles with velocities as high as 14 km/s. Several other dust accelerators were built at this time—all of them based on Friichtenicht's design [4].

4.2 Impact ionization theory, models, and experiments

In 1964 Friichtenicht [5] observed that hypervelocity impacts of iron particles on metal targets resulted in the production of ions. He found that impacts on metals such as tantalum, tungsten, and platinum produced significantly more ions than impacts on lead, indium, or beryllium-copper. He also found that craters on the former set of metals were much smaller than craters on the latter set of metals, implying a relationship between the ionization susceptibility and cratering susceptibility of the metals. Two directions of research resulted from this discovery: (1) attempts to understand the ion formation process, and (2) efforts to use impact ionization as a method for studying cosmic dust.

Soon after Friichtenicht's discovery Auer and Sitte [6] and Hansen [7] performed nearly identical experiments in which the ions produced during hypervelocity impacts of

iron particles were characterized using time-of-flight mass spectrometry. When extracting positive ions they observed singly charged sodium, potassium, iron, and sometimes hydrogen, carbon, and oxygen. Sodium, although frequently the largest peak in the spectra, constituted only 2 ppm of the target plate composition, as determined using flame photometric measurements. Negative charge extraction experiments showed that electrons accounted for all negative charge produced.

Later experiments by Friichtenicht *et al*. [8], Dietzel *et al*. [9], and Roy [10] showed similar results. From these experiments emerged a theoretical model of impact ionization. Ions from elements with lower ionization potentials (e.g., alkali metals) were much more abundant than ions from elements with higher ionization potentials. The number of ions of each type was consistent, at least to a first approximation, with an equilibrium plasma described by the Saha equation [11]:

$$\frac{n_e n_i^s}{n_n^s} = CT^{3/2}\left(\frac{u_i^s}{u_n^s}\right)e^{\left(\frac{-E_I^s}{kT}\right)}, \tag{3}$$

where n_e is the total number of electrons per unit volume, n_i^s is the number of ions of species *s* per unit volume, n_n^s is the number of neutral species per unit volume, C is a constant, T is the plasma temperature, u_i^s and u_n^s are the internal partition functions of ions and neutrals of species *s*, k is Boltzmann's constant, and E_I^s is the ionization potential of species s. The presence of certain species with high ionization potentials, such as hydrogen, carbon, and oxygen, was much greater than could be accounted for in this equilibrium plasma model. However, the intensities of hydrogen, carbon, and oxygen peaks increased with impact velocity. Friichtenicht [8] and Roy [10] used the ratios of ions of metal species (including alkali metals) to estimate the plasma

temperatures in impacts, which they reported as being typically 6000 K ± 3000 K for impacts in the range of 20-50 km/s. Their data show no relationship between plasma temperature and impact velocity within this range of velocities, although such a relationship was expected. In each of these studies the total charge, Q, produced during an impact was fit to the empirical relationship:

$$Q = Km_p^{\alpha} v^{\beta}, \tag{4}$$

where K is a constant for each material (dependent largely on the atomic mass), m_p is the mass of the particle, and v is the impact velocity. Values for α range from 1.33 to 0.154 and seem to show a dependence on both the impact velocity and the experimental conditions. The value of β is usually near 1.

In the 1980s three identical impact ionization time-of-flight mass spectrometers were included on three of the five spacecraft that encountered Halley's Comet [12]. During this time, laboratory dust impact experiments focused on the goal of understanding impacts in the velocity range of the comet encounter, 70-80 km/s. No new results were obtained, but a great deal of work was done in comparing impact ionization yields to other ionization types, such as ion or atom bombardment, IR and UV laser ionization, and electronic ionization [13, 14]. Data from the comet particles showed an unexpectedly large number of hydrogen (H), carbon (C), nitrogen (N), and oxygen O) ions [15, 16], as well as expected ions from iron, silicon, and magnesium [17]. The lighter elements, H, C, N, and O, were interpreted to indicate the presence of relatively high concentrations of organic species, supported by the presence of very small peaks at heavier masses corresponding possibly to organic fragments and molecules [18, 19].

More recent contributions to understanding impact ionization have included hydrocode calculations and other theoretical treatments [20-22] that estimate ionization parameters based on shock wave propagation and the thermodynamic properties of irreversible adiabatic expansions. However, these calculations are unable to explain the presence of many ions for impacts at less than 40 km/s, and they greatly underestimate the ion yield of species such as hydrogen, carbon, and oxygen. They attributed these "extra ions" to surface disturbances, as occur when a shock wave reaches a free surface. Recent experiments [23] also show ions assumed to be produced in an equilibrium plasma with unexplained ions such as hydrogen, carbon, nitrogen, or oxygen.

In 1991 Abramov and co-workers [24] examined the angular and energy distributions of ions produced in impacts of aluminum particles with velocities of 1-11 km/s, although results are only presented for a particle with a velocity of 3.4 km/s. In this case the initial kinetic energies were on the order of 2 eV. They note, however, that these ions were extracted using a very low electric field (1 V/cm), and that higher fields produced larger kinetic energies. Their energy analysis was based on the widths of the mass spectra peaks, although no information about calibration was given.

In the latter half of the 1990s, researchers at the University of Kent at Canterbury, England, performed several dust accelerator experiments in order to determine the nature of the ionization mechanism and ion yields for different species. Comparing experimental results to theoretical predictions shows good agreement for metal ions but poor agreement for non-metal ions [25]. However, theoretical predictions using different methods sometimes vary considerably. In one experiment they observed the shape of the mass spectra peaks for ions originating from a 94 km/s impact of a

boron carbide particle on a silver-doped aluminum surface [26]. They observed peaks corresponding to hydrogen, carbon, aluminum, and silver. Although only one spectrum was observed, they used the shapes of each spectral peak to estimate the thermal properties of the ions produced. They reported that both hydrogen and carbon ions were best fit by a Gaussian curve, indicating a non-equilibrium plasma. Hydrogen ions had an initial kinetic energy of 160 ± 16 eV, while carbon ions were 40 ± 25 eV. Aluminum ions showed initial kinetic energies of 9.7 eV, and the peak shape was not easily fit to either a Gaussian or Maxwellian curve, so no distribution was given. Hydrogen ions showed an angular distribution of $\cos^3 \theta$ with respect to the normal, while aluminum ions showed a $\cos^2 \theta$ distribution. They note that the number of carbon ions detected was greater than the number of carbon atoms assumed to be present in the impacting boron carbide particle. Presumably both hydrogen and carbon had come from some other source, such as pump oil adsorbed to the exterior of the particle and aluminum surface. Of course, if sufficient oil had adsorbed onto the particle to produce as many ions as they saw, the particle's velocity would have been greatly reduced before striking the impact plate of their mass spectrometer. The initial kinetic energies of ions produced showed a large variation, revealing a complication in the traditional impact ionization mechanism. Not only were hydrogen and carbon ions being produced in much greater quantities than theory predicted, but they were being produced with larger initial kinetic energies than expected.

Although the energy required to produce free H^+, C^+, and O^+ is much higher than the impact energy, their presence may be explained by a theory proposed by Novikov [27] and discussed by Sysoev [28, 29] and McDonnell [30]. They postulate that an electric

discharge occurs between the charged particle and target surface immediately before impact. According to their model, as the charged microparticle approaches the surface, the high electric field causes electrons to be emitted from the target surface and strike the particle, causing electron-induced desorption and ionization. Implications of this model are discussed in greater detail in Section 4.8. Of particular importance are implications of charge-induced ionization on interpretation of the spectra taken during hypervelocity microparticle impact studies of the Dustbuster. Of course, this mechanism also has implications for interpretation of spectra from other instruments, and this is also discussed.

4.3 The dust accelerator at Concordia College, Moorhead, Minnesota

Following laser desorption experiments (described in Chapter 3), the Dustbuster was tested using hypervelocity microparticle impacts to simulate cosmic dust. These tests were conducted on the van de Graaff dust accelerator at Concordia College in Moorhead, Minnesota.

One of the original Friichtenicht-style dust accelerators was built for NASA in the early 1960s under the direction of Otto Berg. When funding for dust research became sparse, use of this accelerator was discontinued, and in 1975 the accelerator was donated to Concordia College, Berg's *alma mater*. The faculty of the Concordia Physics Department has maintained the accelerator in working condition since then. To my knowledge it is now the only operational van de Graaff dust accelerator in the Western Hemisphere (other operational accelerators being in Germany and England, and a

recently constructed accelerator in Japan). Hypervelocity microparticles produced at the Concordia dust accelerator were used for testing the Dustbuster and for other microparticle impact studies.

The design of the Concordia dust accelerator is essentially identical to Friichtenicht's accelerator [3], and is shown in Figure 4.1. The principal components include the vacuum system, the dust reservoir and charging needle, the 2 MV van de Graaff ball, and charge-sensitive electrodes along the length of the flight tube.

The dust reservoir and charging needle, illustrated in Figure 4.2, are located within the van de Graaff ball. Because the dust reservoir is floated at high voltage, all the associated electronics are optically isolated. The dust particles, typically a fine powder (particle sizes ranging from about 0.1 to 10 μm) are stored in a small box-like cavity. Above the powder rests a planar electrode (the "tongue"), normally at the same electrical potential as the dust. When the dust source is triggered, a voltage is applied to the tongue, creating an electric field in the box and inducing charge on the dust grains. If the Coulombic repulsion on a given grain is sufficient to overcome gravity, the particle rises and strikes the tongue. The resulting dust motion is similar to the motion of gas molecules. Eventually some dust grains will leave the dust reservoir through a small hole and enter the region of the charging electrode. In this region particles continue to "bounce around," acquiring the potential of the surface contacted. Due to this random motion, particles may come into contact with the charging electrode, which is held at a potential several kV higher than the surroundings. Upon contact with the charging electrode, particles acquire a large positive charge, and some of them may have

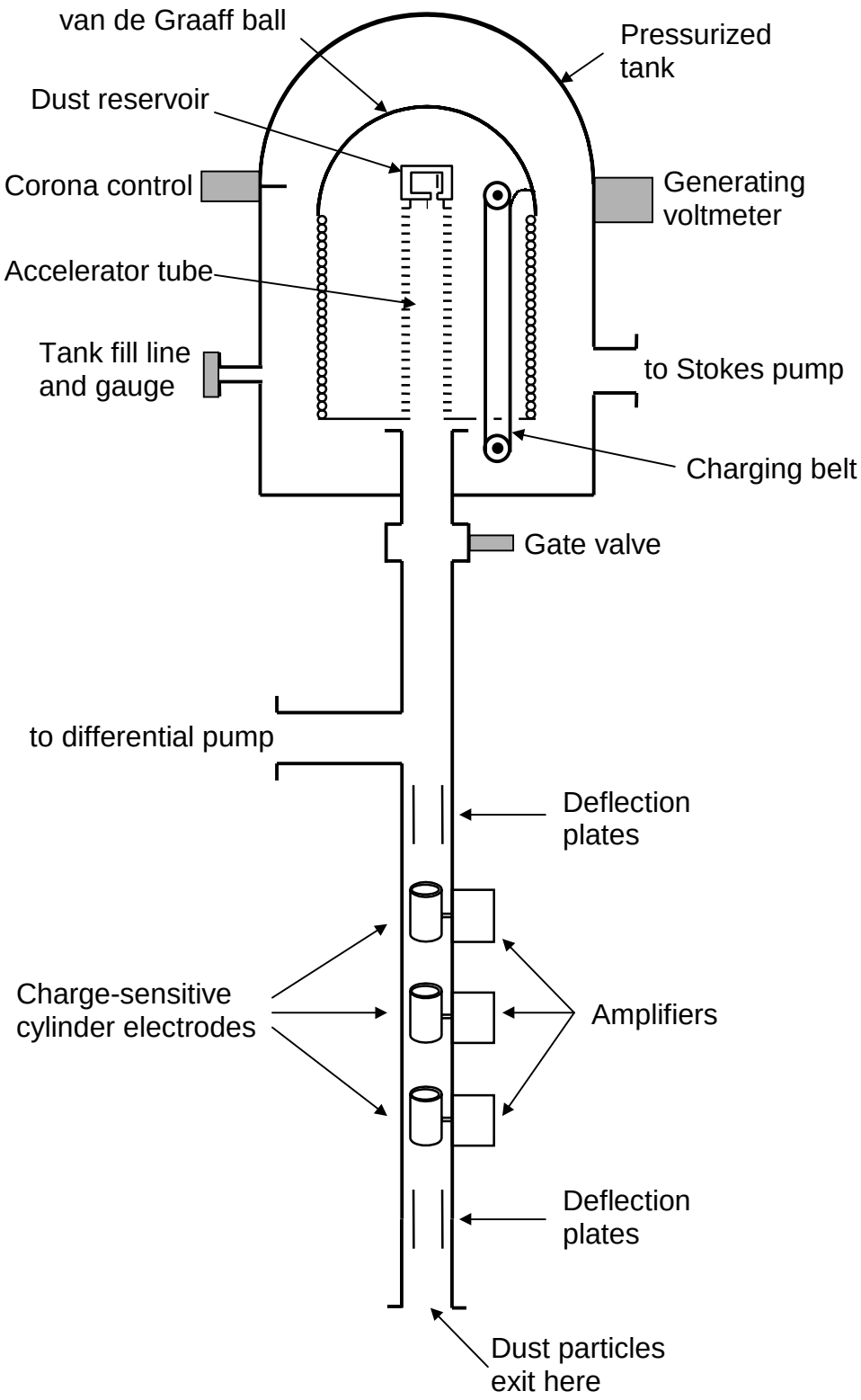

Figure 4.1. Diagram of the van de Graaff dust accelerator at Concordia College.

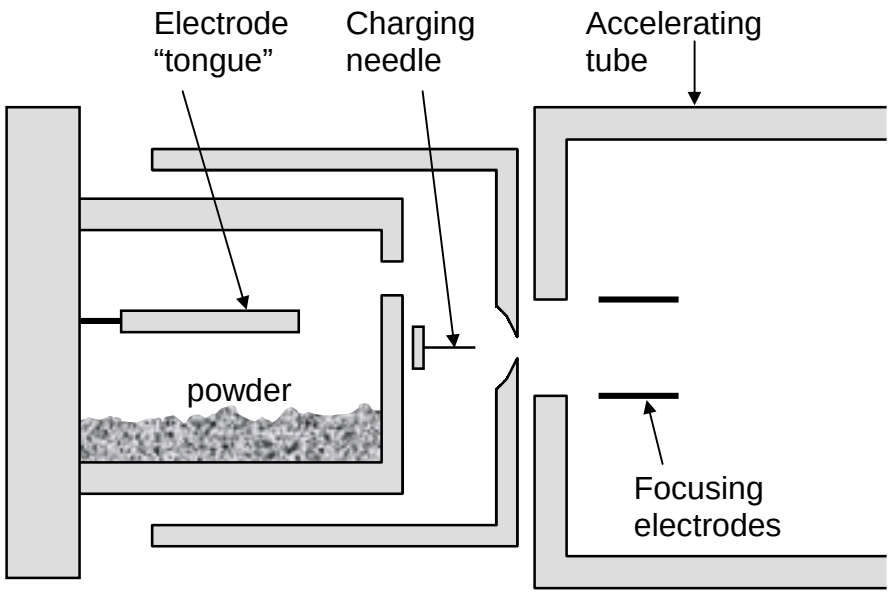

Figure 4.2. Details of the dust reservoir of the van de Graaff accelerator.

the proper trajectory to leave the charging region and enter the accelerating tube. In the accelerating tube particles are accelerated from the van de Graaff voltage to ground.

Three cylindrical electrodes within the flight tube allow measurement of the charges and velocities of the accelerated particles. Each particle induces an image current as it passes through each cylinder. The resulting voltage pulses are combined, amplified, and recorded by an oscilloscope. Particle charge, q, can then be calculated using the relation

$$q = CV \,, \tag{5}$$

where C is the measured capacitance of the first cylinder electrode in the drift tube, and V is the magnitude of the induced voltage pulse. Particle velocity is determined from the distance between the other two electrodes and the time between those signals. Particle mass, m, is found from

$$m = \frac{2qV_a}{v^2} \,, \tag{6}$$

where V_a is the total accelerating voltage and v is the measured particle velocity. The lower limit of charge sensitivity of the cylinder electrodes is around 1 fC, corresponding to a maximum observable velocity of 20-30 km/s and minimum observable mass of around 5×10^{-18} kg, based on typical surface charge densities of the accelerated metal particles. Charge is roughly proportional to surface area and mass is proportional to volume, leading to an overall $v \propto r^{-1/2}$ relationship. As a result, smaller particles with less charge are accelerated to higher velocities than larger particles with more charge. Although the van de Graaff ball is rated at 2 MV, due to various limitations the ball is routinely used at only 1.5 MV.

The flight tube also has several electrodes used to select particles with mass and velocity that fall within specified limits, and deflect particles outside those limits. Although these plates could be used for beam alignment, they typically are not. The accelerator is also equipped with a delayed trigger system, in which a trigger pulse is produced when the particle reaches some point beyond the flight tube.

4.4 Characterization of microparticle impacts using energy analyzer

In order to better understand the impact ionization process, I designed and built a pulsed ion energy analyzer to examine the initial kinetic energies of microparticles accelerated with the Concordia accelerator. Ideally an energy analyzer for this purpose would measure both the kinetic energy distribution and the spatial distribution of each type of ion. Most energy analyzers, such as retarding field [31], cylindrical mirror [32], and directional filtering analyzers [33] require a continual beam of ions, and the energy or spatial distribution is scanned in some fashion. Pulsed ion sources cannot be scanned, although statistical analysis of many pulses can be used to give similar results. Pulsed ion sources are generally studied using time-of-flight methods [34]. In time-of-flight methods, the arrival time of any given ion is related to its initial kinetic energy (plus any additional extraction energy). Analysis of ion energies is subject to errors due to the same factors that affect mass resolution, including detector response, space-charge effects, and ion optics problems [35]. The time-of-flight method was used by Ratcliff for analysis of the 94 km/s impact [26] and by Abramov for lower velocity impacts [24]. In designing my energy analyzer I was severely limited both by time and money. Rather

than performing a fitting analysis on peak shapes as Ratcliff had done, I designed and built a novel pulsed ion energy analyzer based on spatial filtering of ions.

The design of the impact ionization energy analyzer is shown in Figure 4.3. Accelerated dust particles impact the target plate, which is held at some potential. Ions from the impact are extracted by a grounded grid, pass through a reflectron, and are focused onto a microchannel plate detector. However, as the ions leave the reflectron, two removable rings block most of the ions from reaching the detector. The only ions that reach the detector are those for which the velocity components perpendicular to the instrument axis fall within some range. Thus only a "ring" of ions is permitted into the drift region. Varying the extraction voltage and varying the radius of the rings between impacts allows ion energies to be "scanned." Of course, for a given particle, only one range of energies can be detected. Forming a complete distribution description requires a statistical analysis of ions from numerous impacts. While most energy analyzers measure only the "component of kinetic energy" perpendicular to the surface at which ions are formed, this energy analyzer measures the component parallel to the surface (and perpendicular to the instrument axis). Additionally, if the voltage of the front grid is close to the extraction voltage, ions with perpendicular energy components greater than that difference escape the instrument, and are not detected. Thus it is also possible, at least in theory, to scan the perpendicular component of energy, similar to a retarding field analyzer, but subject to the previously mentioned statistical limitations of a pulsed ion source.

The components of energy (or more correctly, velocity) parallel to the impact surface are the result of several factors. First, of course, is the thermal energy and

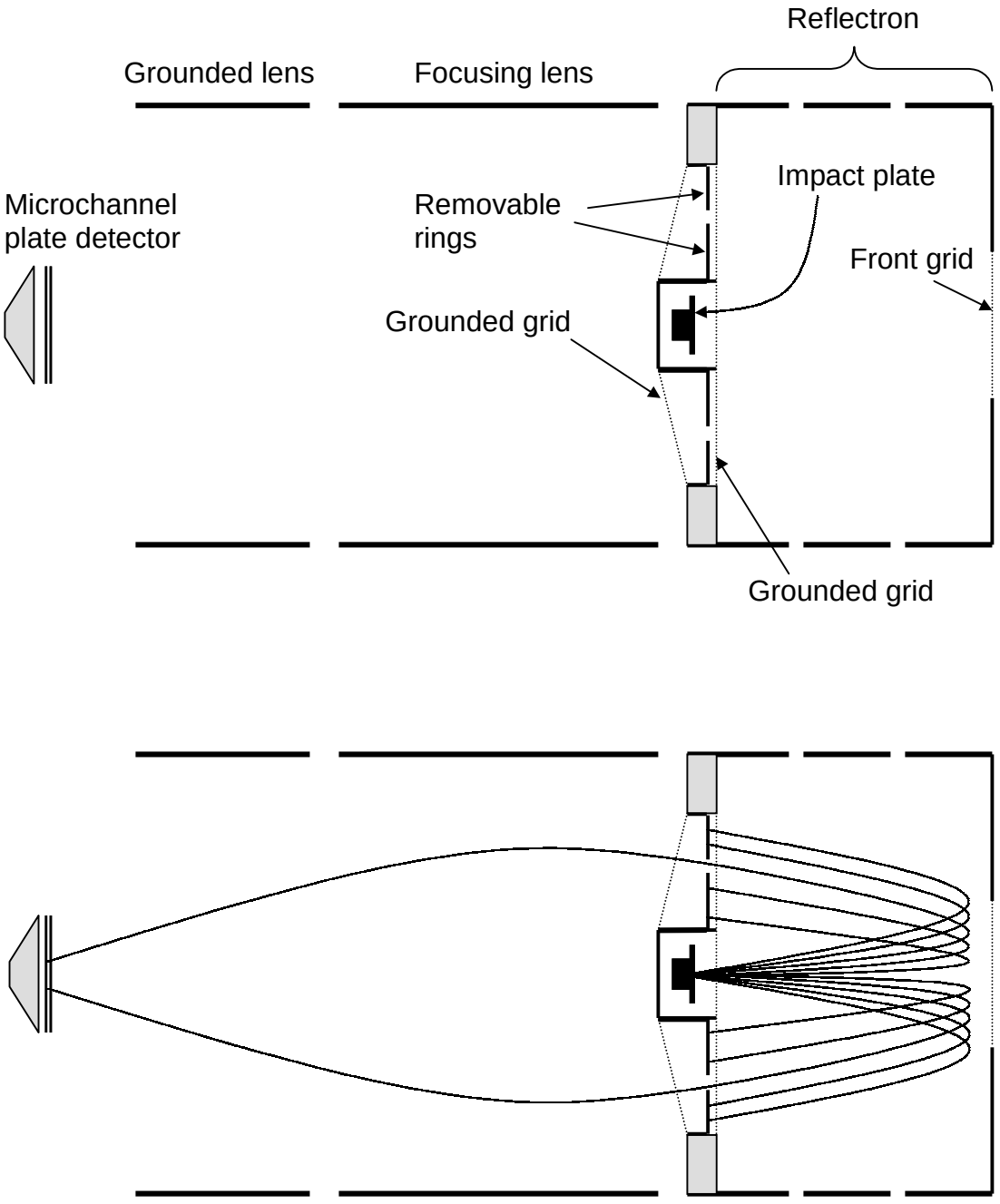

Figure 4.3. Diagram of the energy analyzer. Ions are created at the impact plate, extracted into the reflectron region, and selected for energy at the exit of the reflectron. Ions with correct energies pass on to the MCP detector. In the lower diagram typical ion paths are shown.

spatial distribution arising from the impact plasma itself. Related to this are space-charge effects, which still apply after the plasma expands to a collisionless state. Third, impacts plasmas may not be symmetrical. Spatial inhomogeneities may lead to different local plasma pressures, and ions emerging from these regions may have exceptional kinetic energies. Fourth, although ions are extracted by a reasonably uniform electric field, grid scatter increases the beam spread and increases the average velocity components in these two directions. Lastly, the large electrical field in the extraction region may have an effect on ion energies other than simple addition. Although only the first of these effects is of interest to impact ionization theory, all five factors will be operative in any cosmic dust time-of-flight mass spectrometer. Thus the results from the energy analyzer represent actual conditions in real instruments. Other small effects may influence the spreading out of the ion packet as it traverses the reflectron. These include off-center impacts, roughness of the impact surface, grid scatter from the front grid, imperfect machining and assembly, or inhomogeneous electrical fields in the ion extraction and reflectron regions. It is difficult to assess the relative importance of these factors, and no attempt was made to do so.

Performance of the energy analyzer was simulated using SIMION ion trajectory software. Figure 4.4 shows a typical case.

Figure 4.5 shows the experimental setup for hypervelocity impact studies using the energy analyzer. A mixture of micron-sized iron and copper particles were placed in the dust reservoir. The dust reservoir ball, chamber, and flight tube were then evacuated. On average, 1-10 particles per minute struck the energy analyzer impact plate.

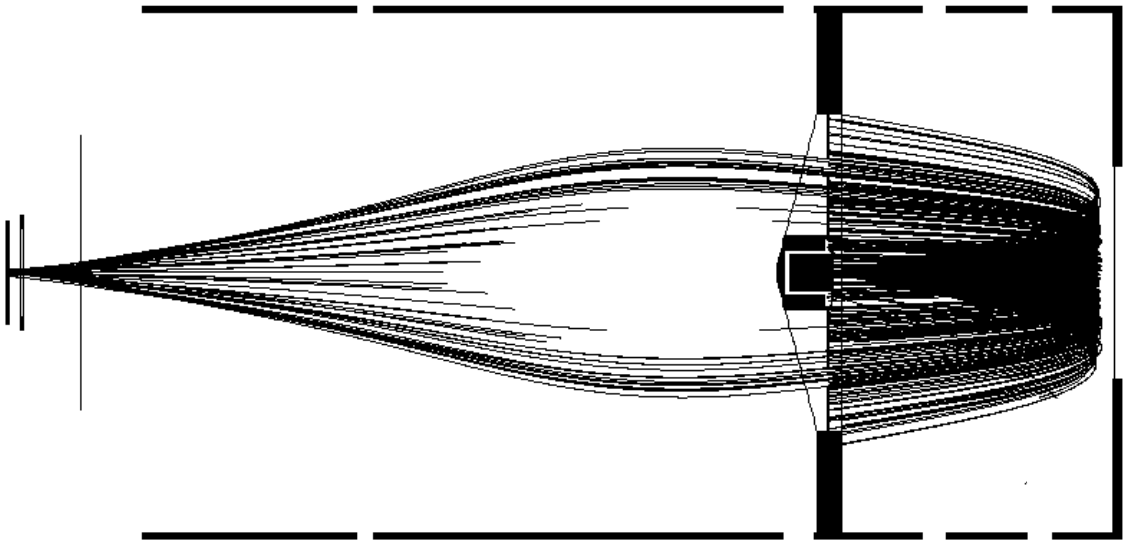

Figure 4.4. Simulation of ion trajectories in the energy analyzer. This is a cut-away view, so portions of the ion trajectories disappear if they are too far away from the plane. Ions have initial KE of 40 eV +/- 25 eV. Extraction voltage is 2600 V, and the opening between rings is at an intermediate radius, as shown.

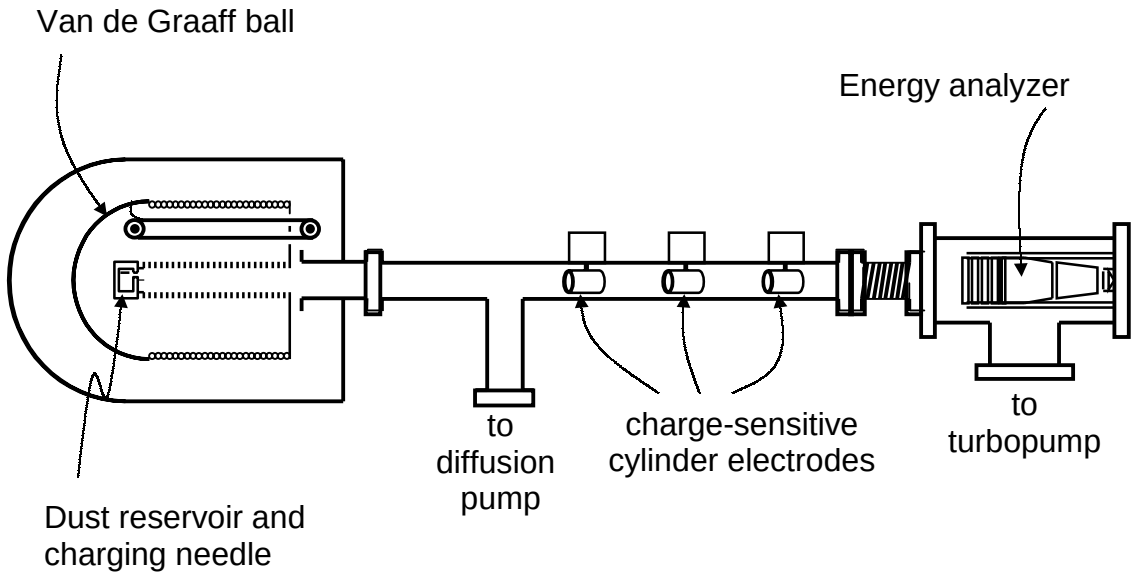

Figure 4.5. Experimental setup for energy analyzer experiments on Concordia van de Graaff dust accelerator. Particles are charged within the van de Graaff ball, then accelerated onto the energy analyzer. Cylindrical electrodes within the flight tube measure charge and velocity of accelerated particles.

The dust reservoir, accelerator, and flight tube were evacuated by a diffusion pump. Because this vacuum system was only able to maintain 3×10^{-6} torr at the exit of the flight tube, the energy analyzer was mounted inside its own vacuum chamber, evacuated by a turbopump to 10^{-7} torr. The two vacuum systems were connected with a 1-cm circular aperture, through which the charged particles left the flight tube and entered the energy analyzer. A flexible bellows allowed alignment of the particle beam (which had a typical spread of 2 mm) with the energy analyzer impact plate.

Particles used included wire-exploded copper with an average diameter of 100-150 nm (Argonide Nanomaterials), 1-micron copper (Sigma Chemical), and 0.1- to 3-micron (diameter) iron spheres produced by the mist reduction of iron carbonyl (General Aniline and Film Corp.).

Spectra were recorded using a 150 MHz Yokagawa digital oscilloscope, which was triggered by the signal on the MCP detector. Over 1,000 dust impact spectra were recorded. Target plate composition included tantalum and molybdenum. Extraction voltages ranged from 150 to 4800 V. The distance between the impact plate and extraction grid was varied between 4, 8, and 12 mm in order to observe any plasma shielding effects. Combinations of any two of ten rings allowed different radii for allowed ions to pass. Unfortunately, interchanging rings, changing the physical length of the extraction region, and changing the impact plate material required breaking vacuum, so a total of only six combinations were used. The ring sizes were chosen to detect ions with energies up to 50 eV (again, referring to the total magnitude of the energy components parallel to the impact plate). It was assumed that for impacts in the range of 1-10 km/s essentially all ions would have less kinetic energy than this. The

energy analyzer was not designed with the capability of measuring the angular or spatial distribution of ions, nor did it have a way of distinguishing a spatial distribution function from the energy distribution function. On the other hand, the entire instrument was designed and built in only two weeks, and at a cost (for materials) of less than $50.

4.5 Results of pulsed ion energy analyzer experiments

Figure 4.6 shows several spectra typical of those acquired on the energy analyzer. Peaks frequently appearing include hydrogen, carbon, oxygen, sodium, potassium, iron, copper, and tantalum. These peaks are the same as those observed in previous impact experiments [10]. Molybdenum appeared in some spectra in which particles impacted the molybdenum plate. A discussion of the origins of each of these peaks is given in Section 4.7.

Variables taken into account in the data analysis included particle velocity, mass, composition, target material, extraction voltage, ring radii, and detector gain. Because of the large number of variables involved, and the large variations between spectra from otherwise identical impacts, no statistically significant information was obtainable regarding the energy distribution of ions produced. However, one interesting and important observation was made: even with the highest extraction voltage (4800 V) and the largest ring set, a large number of ions were still reaching the detector, even for slow impacts (2-3 km/s). This implies that the initial kinetic energy components parallel to the impact surface were quite high for these impacts. The ions resulting from these impacts had initial kinetic energies of at least 50 eV, and probably much higher.

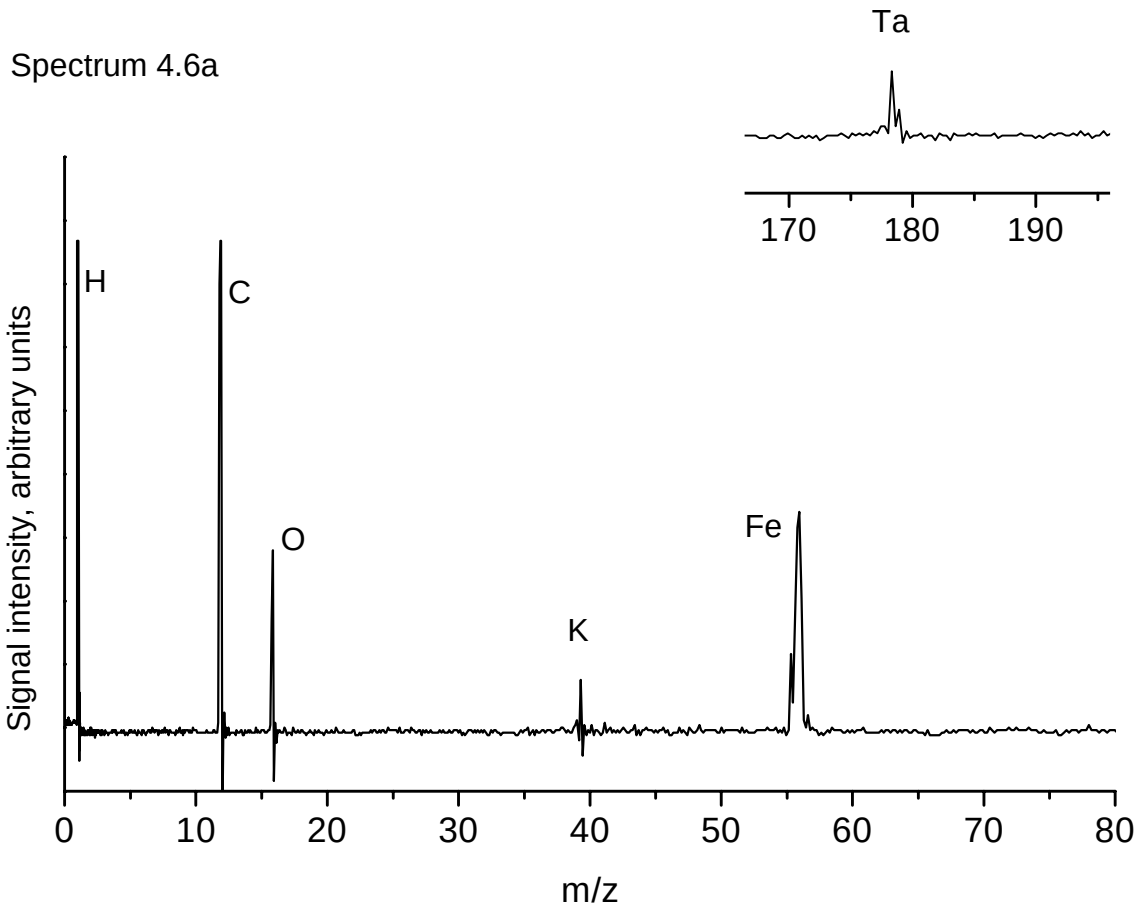

Figure 4.6. Typical spectra from energy analyzer. Spectrum 4.6a is from a 1.88×10^{-15} kg iron particle impacting the tantalum target at 3.3 km/s. Extraction voltage: 4750 V, extraction region length: 12 mm, ring set: 0.73-0.88" radius, MCP detector: ~767 volts per plate.

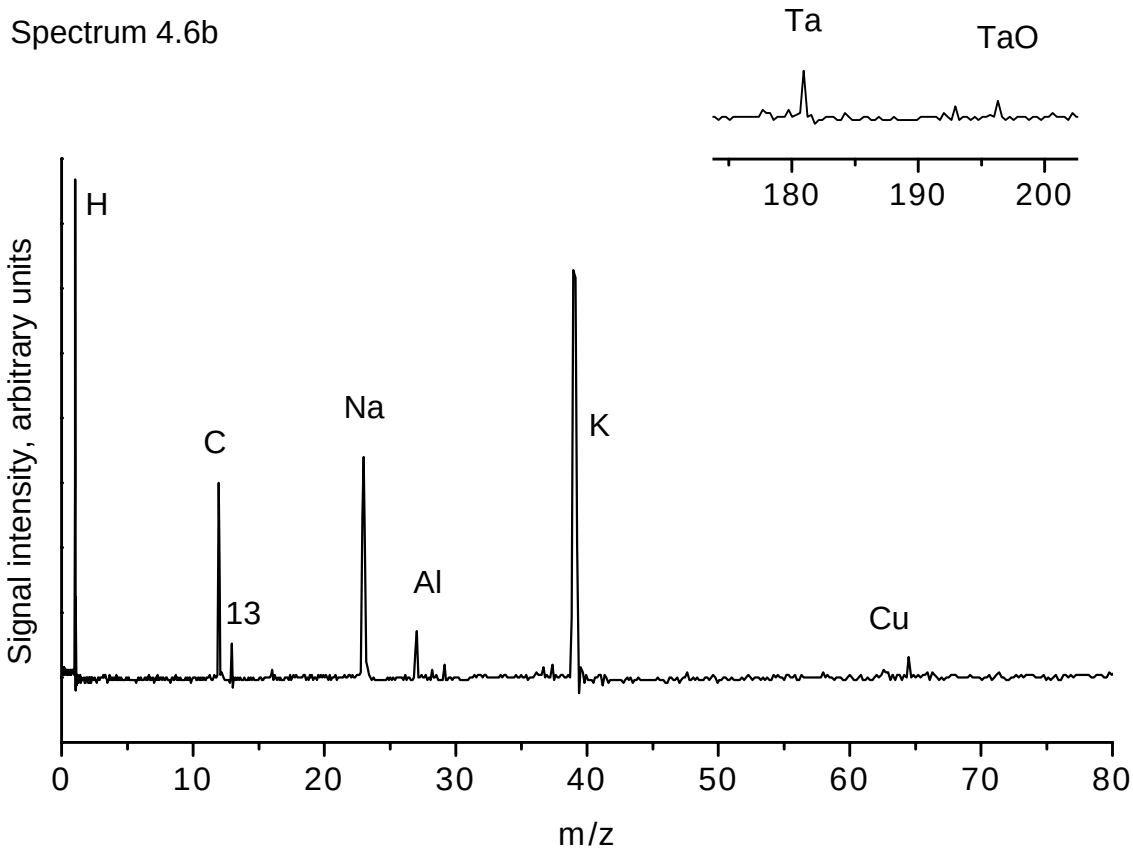

Figure 4.6, continued. Typical spectra from energy analyzer. Spectrum 4.6b is from a 3.37×10^{-16} kg copper particle impacting the tantalum target at 6.4 km/s. Extraction voltage: 4750 V, extraction region length: 12 mm, ring set: 0.73-0.88" radius, MCP detector: ~767 volts per plate.

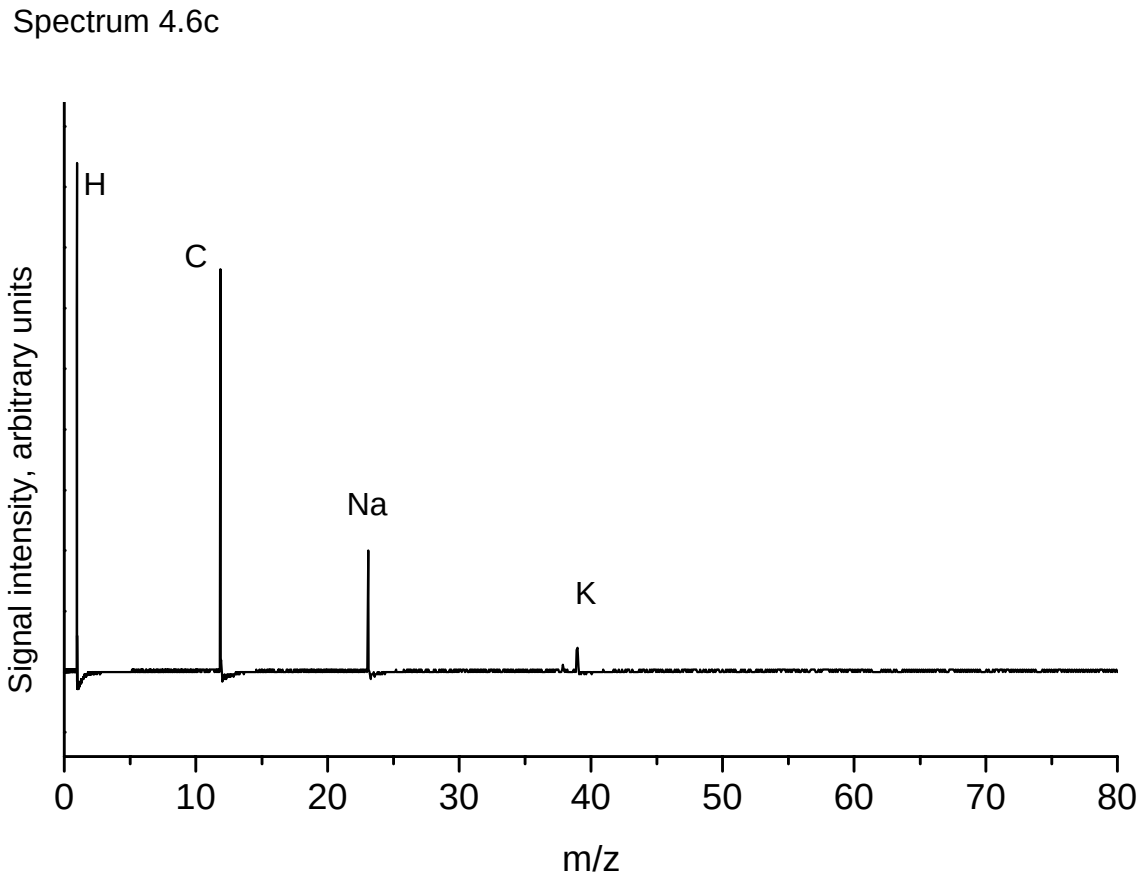

Figure 4.6, continued. Typical spectra from energy analyzer. Spectrum 4.6c is from an impacting particle with unknown mass and velocity. Extraction voltage: 950 V, extraction region length: 9 mm, ring set: 0.50-0.66" radius, MCP detector: ~833 volts per plate.

Spectrum 4.6d

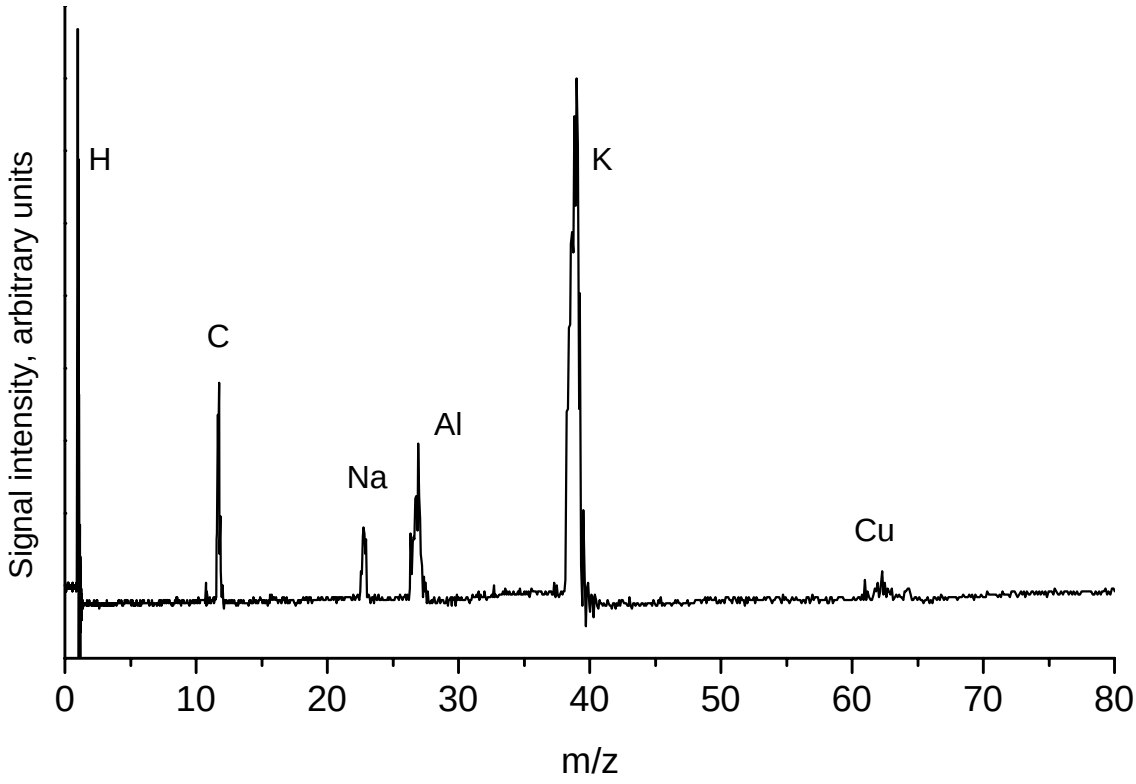

Figure 4.6, continued. Typical spectra from energy analyzer. Spectrum 4.6d is from an impacting copper particle with unknown mass and velocity. Extraction voltage: 1925 V, extraction region length: 9 mm, ring set: 1.09-1.25" radius, MCP detector: ~767 volts per plate.

Spectrum 4.6e

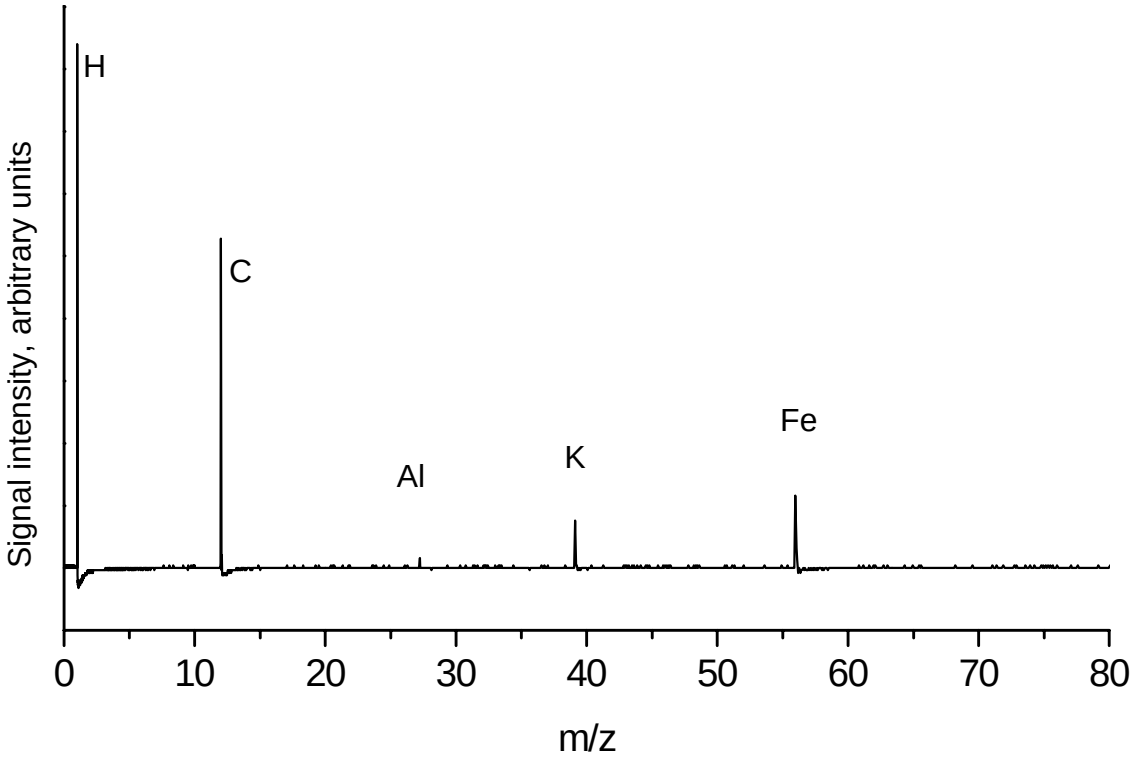

Figure 4.6, continued. Typical spectra from energy analyzer. Spectrum 4.6e is from an impacting iron particle with unknown mass and velocity. Extraction voltage: 950 V, extraction region length: 9 mm, ring set: 0.50-0.66" radius, MCP detector: ~833 volts per plate.

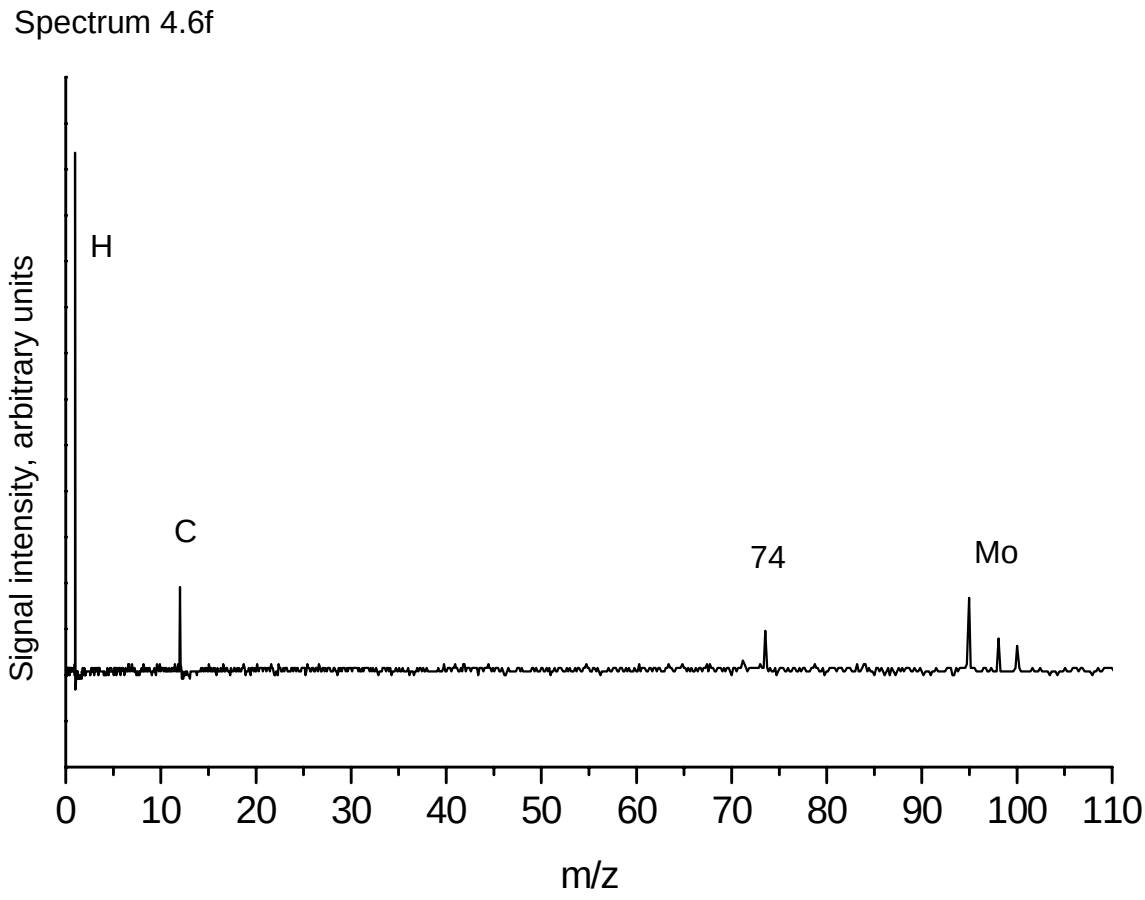

Figure 4.6, continued. Typical spectra from energy analyzer. Spectrum 4.6f is from an impact on the molybdenum target plate by 3.3 km/s, 1.6×10^{-14} kg particle. Three isotopes of molybdenum are clearly visible (95, 98, and 100); other isotopes do not appear. Extraction voltage: 3800 V, extraction region length: 9 mm, ring set: 0.73-0.88" radius, MCP detector: ~833 volts per plate.

Spectrum 4.6g

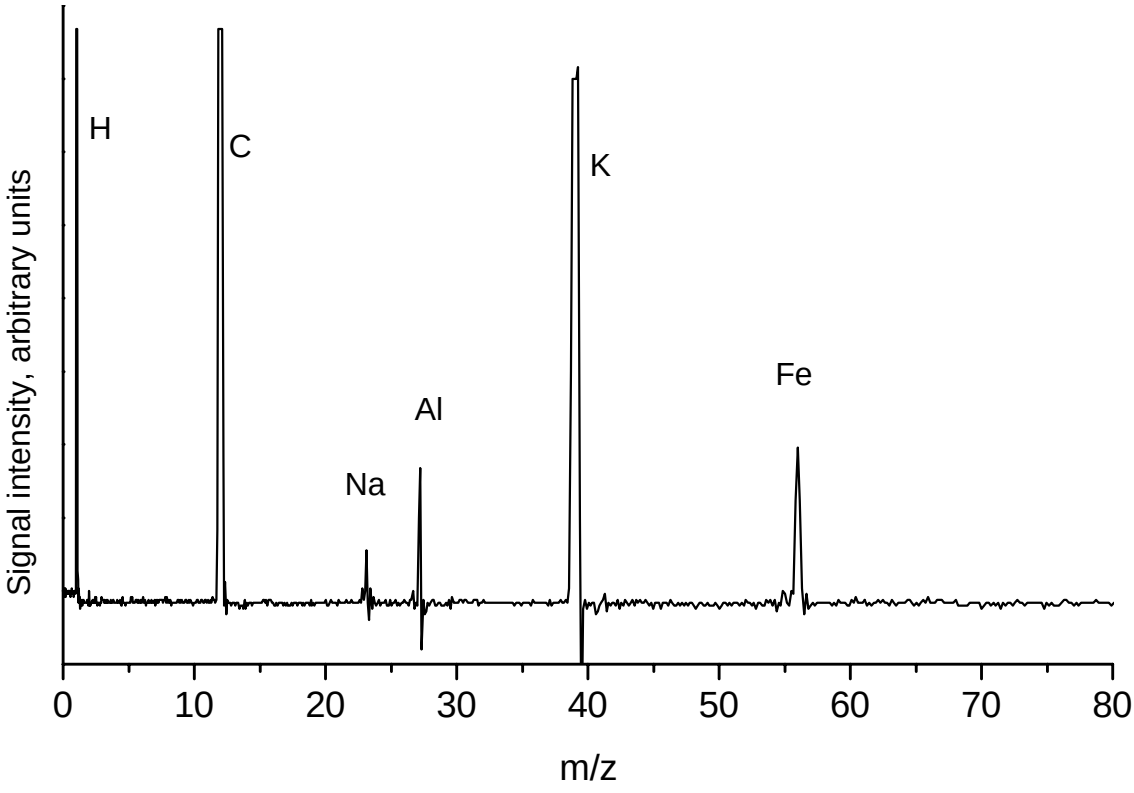

Figure 4.6, continued. Typical spectra from energy analyzer. Spectrum 4.6g is from an impacting iron particle with unknown mass and velocity. Extraction voltage: 4500 V, extraction region length: 9 mm, ring set: 1.09-1.25" radius, MCP detector: ~767 volts per plate.

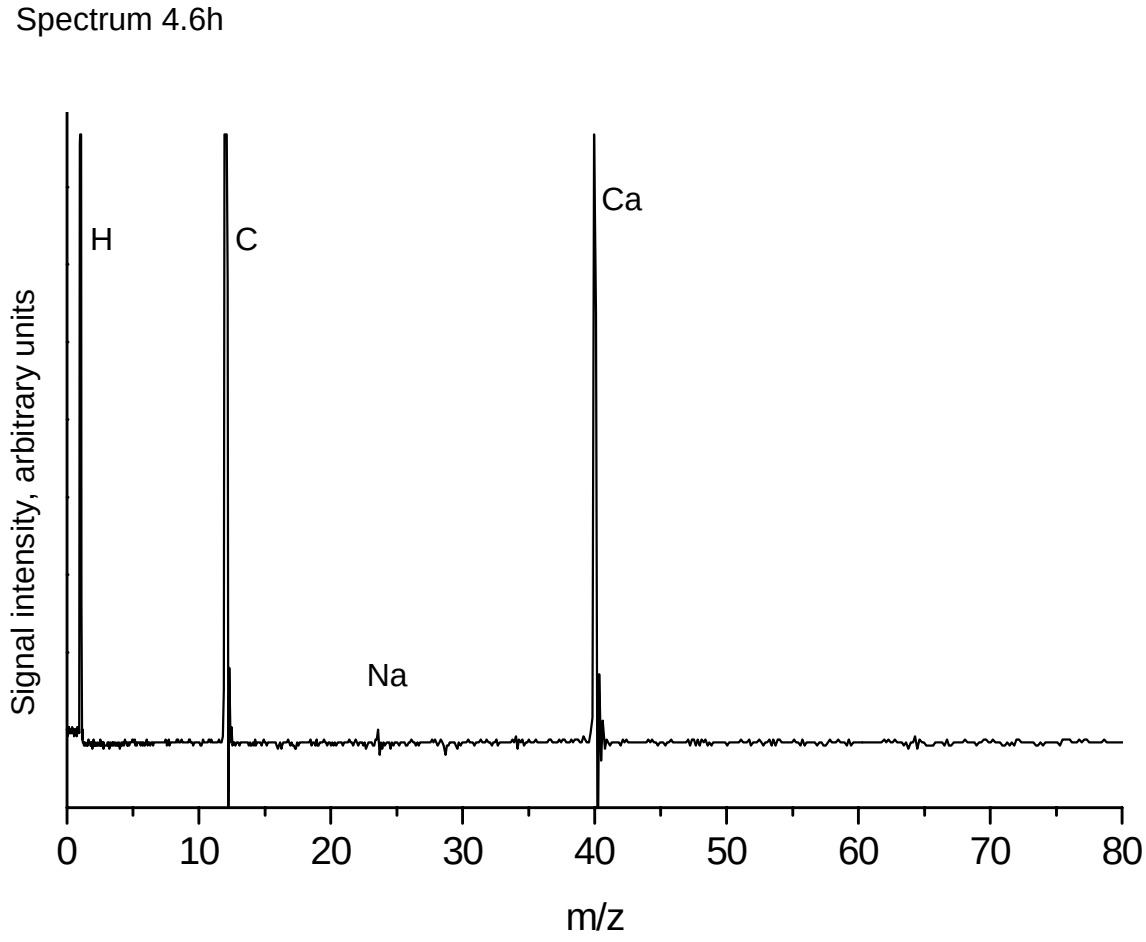

Figure 4.6, continued. Typical spectra from energy analyzer. Spectrum 4.6g is from an impacting particle with unknown mass and velocity. Extraction voltage: 4500 V, extraction region length: 9 mm, ring set: 1.09-1.25" radius, MCP detector: ~767 volts per plate.

Although some of this detected kinetic energy may be due to grid scatter effects, such effects will be present in the Dustbuster and other dust mass spectrometers, and must be taken into account when designing ion optics systems for such instruments. Effects of grid scatter and related extraction phenomena on initial kinetic energies would not have appeared in the experiments of Abramov [24]. Some contribution to the initial kinetic energies undoubtedly came from the thermal properties of the plasma, although separating these two types of effects is not possible at this time. The large initial kinetic energies are not explainable using models of shock-induced ionization and equilibrium plasma. They may be the result of more highly energetic (although perhaps more localized) ionization effects.

4.6 Experimental setup for Dustbuster testing

Hypervelocity microparticles from the Concordia dust accelerator were also used to test the performance of the Dustbuster.

The experimental setup was similar to that used with the energy analyzer, as illustrated in Figure 4.7. Micron-sized iron and copper particles were placed in the dust reservoir. The dust reservoir ball chamber and flight tube were then evacuated. On average, 1-10 particles per minute struck the Dustbuster impact plate. Because the spectrum acquisition time was only 10 μs, the probability of overlapping spectra from coincident particles was negligible.

The dust reservoir, accelerator, and flight tube were evacuated by a diffusion pump. Because this vacuum system was only able to maintain 3×10^{-6} torr at the exit of

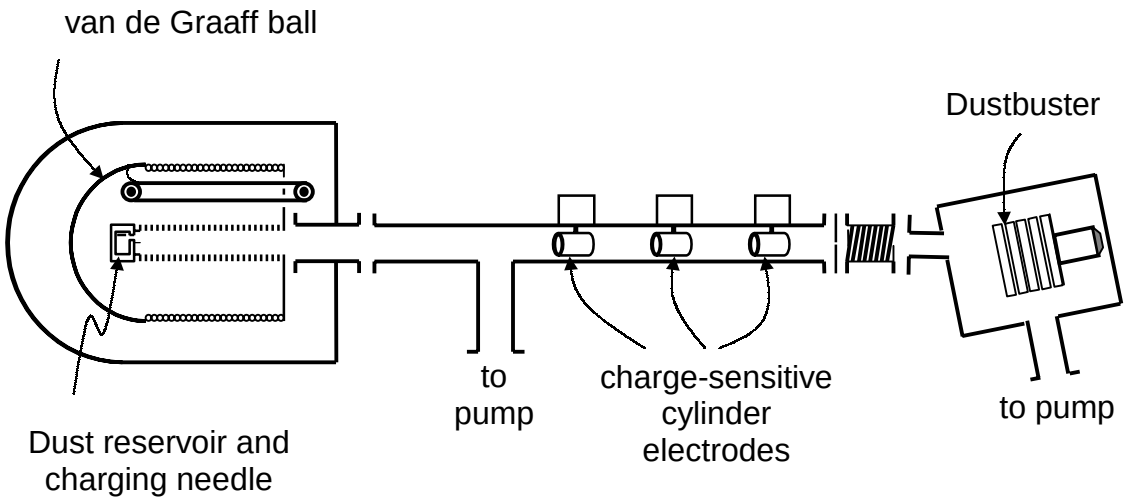

Figure 4.7. Experimental setup for particle impact studies on the Dustbuster. Particles are charged within the van de Graaff ball, then accelerated onto the Dustbuster target plate. Cylindrical electrodes within the flight tube measure charge and velocity of accelerated particles. To permit alignment and testing, the entire Dustbuster vacuum chamber is mounted on a translation/rotation stage capable of motion in all six degrees of freedom.

the flight tube, the Dustbuster was mounted inside its own vacuum chamber, evacuated by a turbopump to 10^{-7} torr. The two vacuum systems were connected with a 1-cm circular aperture, through which the charged particles left the flight tube and entered the Dustbuster. The Dustbuster vacuum chamber included angled connection ports in order to observe particle impacts at angles of up to 25° from the normal. Further, a flexible bellows directed the particle beam to various locations on the target plate, covering all radial distances from 1.5 to 4 cm from the instrument axis. The Dustbuster vacuum chamber was mounted on a large, custom-designed xyz translation/3-axis rotation stage which assisted in varying and measuring the angle and location of the particle impacts on the target plate.

Particles used included wire-exploded copper with an average diameter of 100-150 nm (Argonide Nanomaterials), 1-micron copper (Sigma Chemical), and 0.1- to 3-micron (diameter) iron spheres produced by the mist reduction of iron carbonyl (General Aniline and Film Corp.). The majority of experiments were carried out using iron particles alone. On the assumption that the composition of each particle could be deduced from its mass spectrum, the dust reservoir was filled with a mixture of copper and iron powder in a few later experiments.

For these experiments the entrance grid and extraction grid of the Dustbuster were made of knitted tungsten (Kimball Physics) and electroformed nickel (Buckbee-Mears), respectively. The target plate was made out of 99.95% pure tantalum (Alfa Aesar), sanded with 2400-grit silicon carbide sandpaper, degreased, cleaned, and sonicated in HPLC grade methanol. A sputtered target would have been better, but was not available.

The Dustbuster was originally designed to use 4.8 kV for ion extraction. In order to determine the possibility of operating the instrument using less power, a number of lower voltages were also tried, with all electrostatic potentials scaled proportionally. In addition, the voltage on the microchannel plate detector was independently varied from 700 to 900 volts per plate in order to determine the optimum conditions for observing the mass spectra. The signal from the microchannel plate detector was amplified with a 20x gain differentiating preamplifier (EG&G Ortec VT120) and recorded using a 150 MHz digital oscilloscope (Yokagawa 1520). Spectra were calibrated using the sodium and potassium (^{39}K) peaks. Time-equals-zero points were not directly measured, but were extrapolated using the calibration points. A total of 750 spectra were recorded.

4.7 Results of microparticle impact experiments on the Dustbuster

Figure 4.8 shows particle velocity as a function of mass for all particles studied. Measured particle velocities were generally between 1 and 10 km/s, although velocities up to 23 km/s were observed. Uncertainties in velocity and charge measurements were approximately 5%. Figure 4.9 shows the mass and charge of all detected particles. Also included are lines of constant surface charge density for ideal iron spheres in the range of the measured particles. The charge density of nearly all the particles in this experiment were at least an order of magnitude below the field desorption limit, 2×10^{10} V/m, consistent with previous results using similar charging methods [2, 3, 5]. Interestingly, the larger particles were charged to a fairly constant surface charge density (5×10^{-3} C/m^2), while particles below 2×10^{-16} kg follow more closely a curve

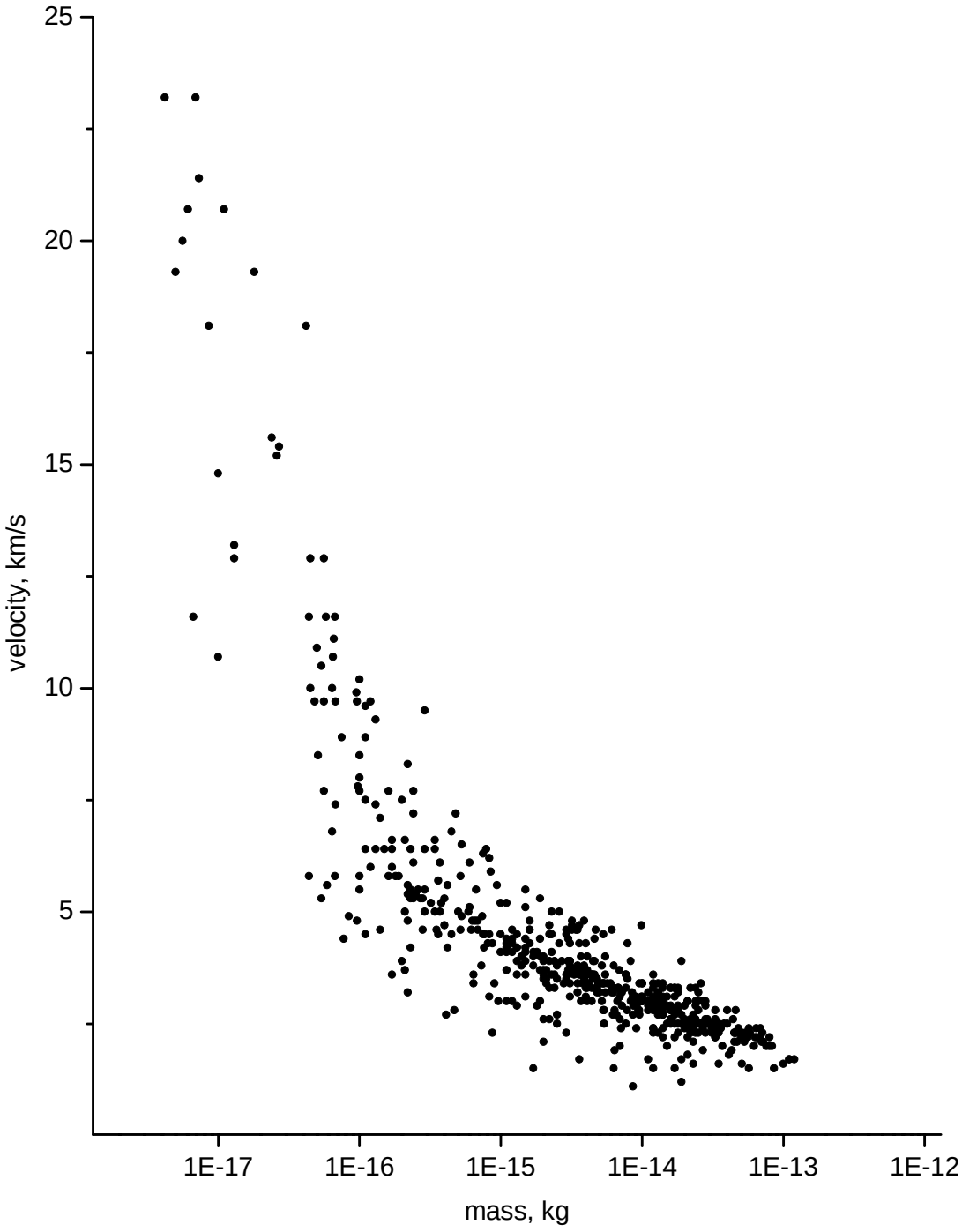

Figure 4.8. Velocity and mass of microparticles studied.

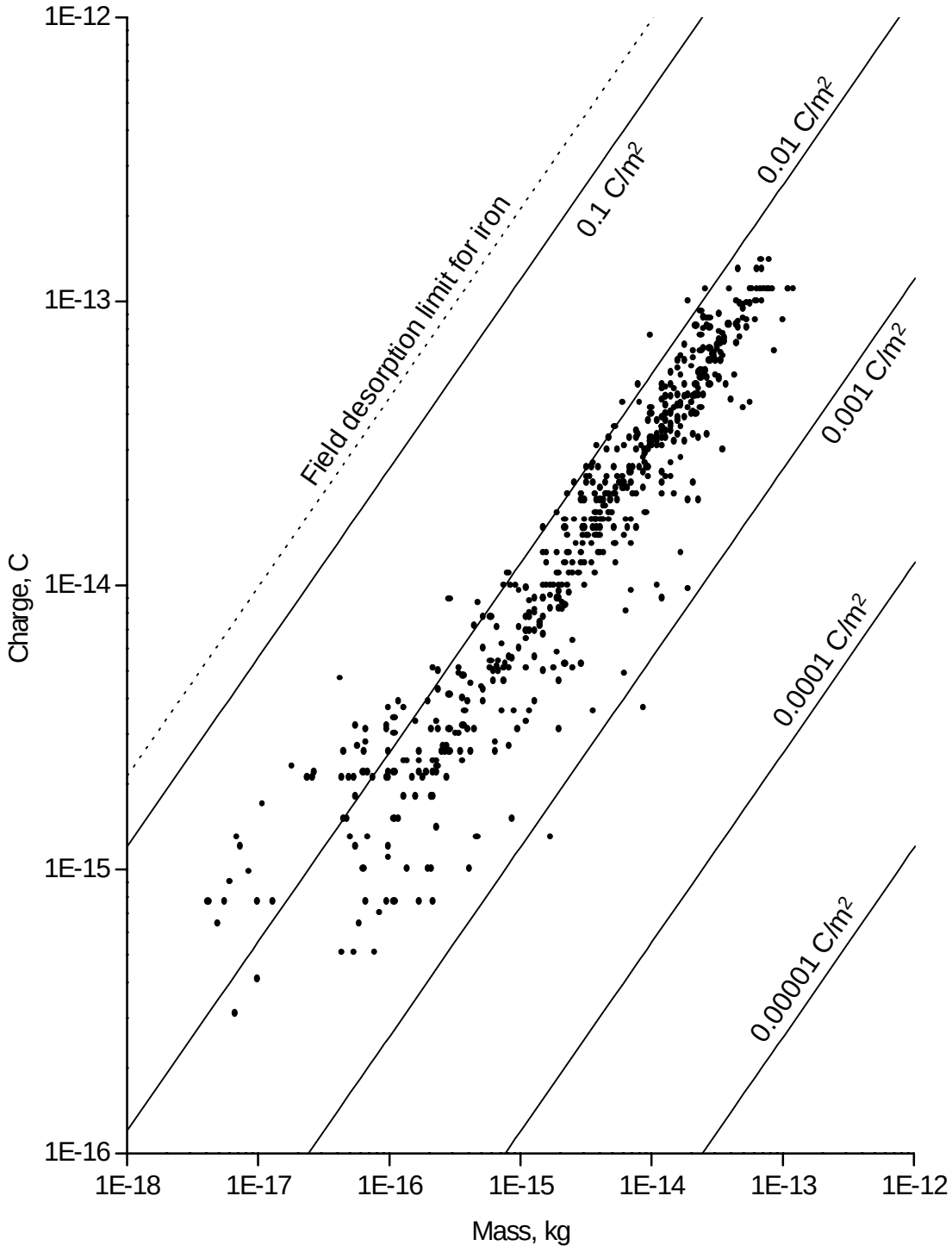

Figure 4. 9. Mass and charge of accelerated microparticles, shown with lines of constant surface charge density for iron spheres.

of constant surface potential. During the experiments, a large number of particles struck the Dustbuster and triggered the recording electronics, but had too small a charge to be detected by the cylinder electrodes in the accelerator flight tube. Nonetheless, most of these particles generated interpretable mass spectra.

Figures 4.10 and 4.11 show representative mass spectra for particles with defined and undefined velocities, respectively. Spectrum 4.10a, typical of roughly 20% of the impacts, shows only sodium (Na^+) and potassium (K^+) ion peaks with high mass resolution. Spectrum 4.10b shows a hydrogen ion (H^+) peak and unusually broad sodium and potassium peaks. Spectrum 4.10c shows broad sodium and potassium peaks along with a strong iron (Fe^+) peak. Similarly broadened peaks appeared in about 15% of the spectra, but sodium and potassium were the only species for which significant broadening occurred. In general, these peaks were broader for slower impact velocities. Impact angle, which was varied from 0º to 23º, did not have any noticeable effect on the amount of peak broadening. In many spectra, the number of ions observed from a given *m/z* exceeded the input voltage limit of the signal amplification or recording electronics, producing the peak clipping seen in spectra 4.10c and 4.10d. Spectrum 4.10d shows peaks corresponding to hydrogen, carbon (C^+), oxygen (O^+), sodium, potassium, and iron, and a peak at $m/z = 40$, which was not positively identifiable, but was assumed to be either calcium or argon. Argon was used in the production of the copper and iron powders, and may have been incorporated into the microparticles. Thus the presence of argon in the spectra would not be surprising. Spectra 4.10e and 4.10f contain similar peaks with varying intensities. Spectra 4.10e and 4.10f showed peaks of tantalum (Ta^+) and tantalum oxide (TaO^+), and these portions of the spectra are shown as inserts. None

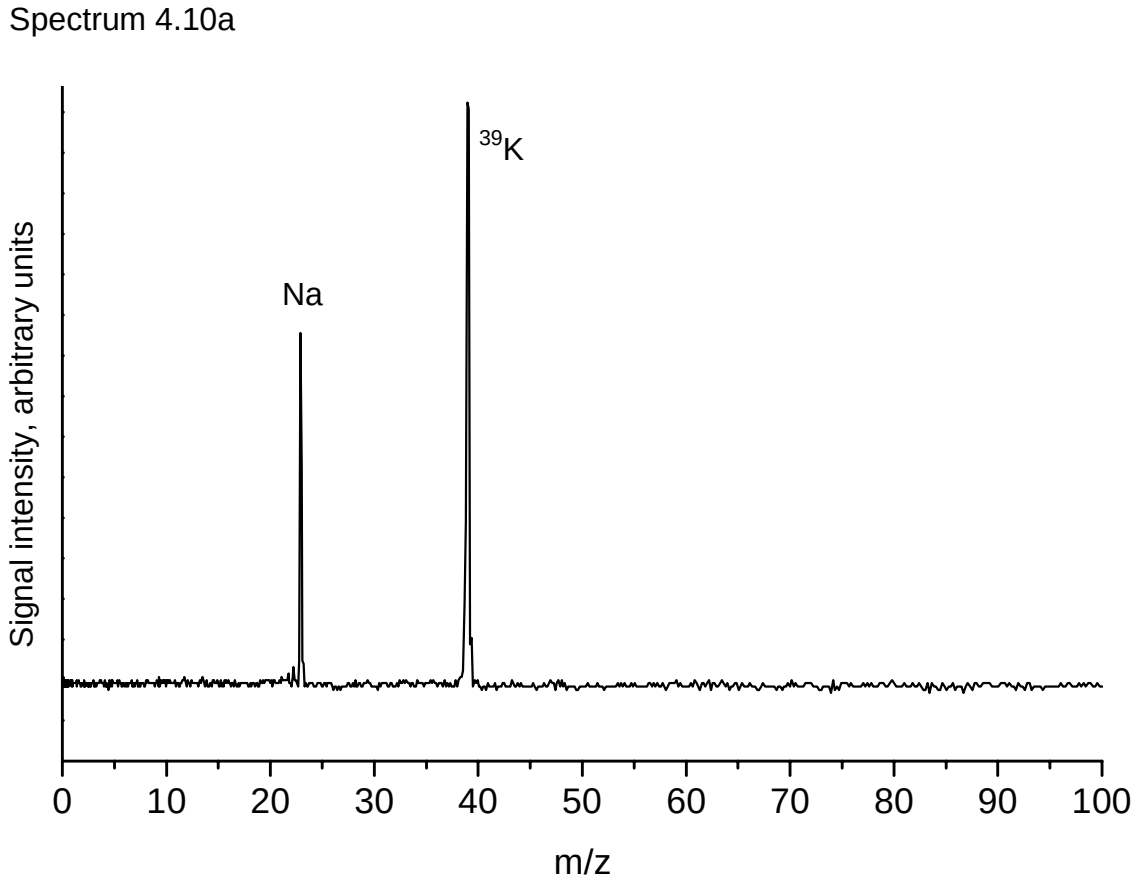

Figure 4.10. Hypervelocity microparticle impact spectra on the Dustbuster. Spectrum 4.10a was from a 1.3 μm, 2.4 km/s impact.

Spectrum 4.10b

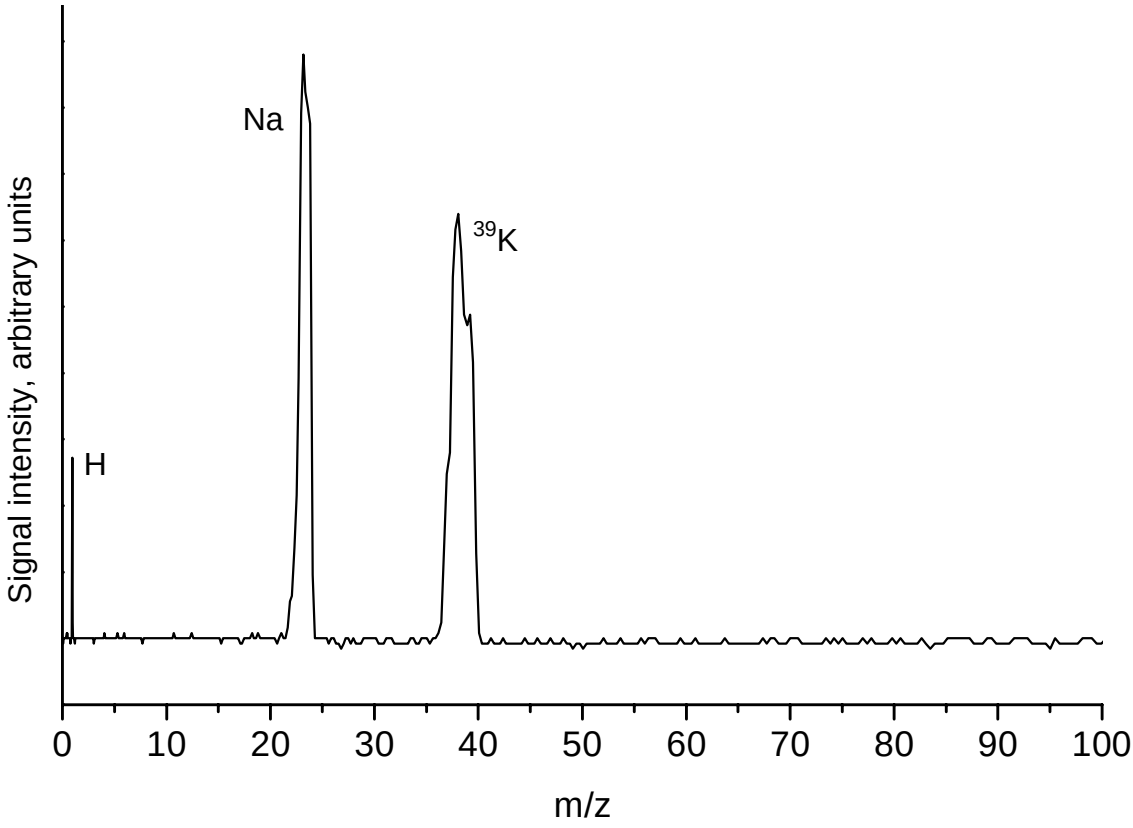

Figure 4.10. Hypervelocity microparticle impact spectra on the Dustbuster.

Spectrum 4.10b was from a 2.0 μm, 2.2 km/s impact.

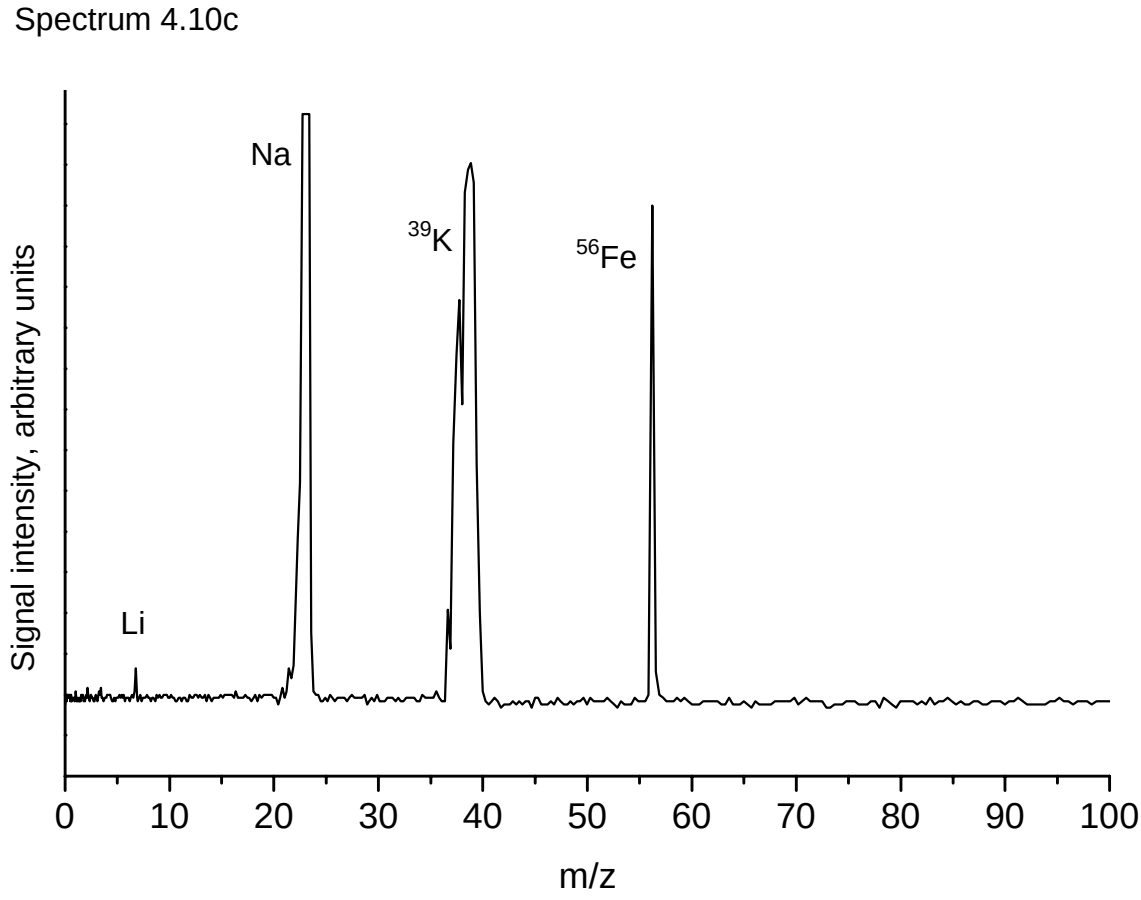

Figure 4.10, continued. Hypervelocity microparticle impact spectra. Spectrum 4.10c was from a 0.3 μm, 4.45 km/s impact.

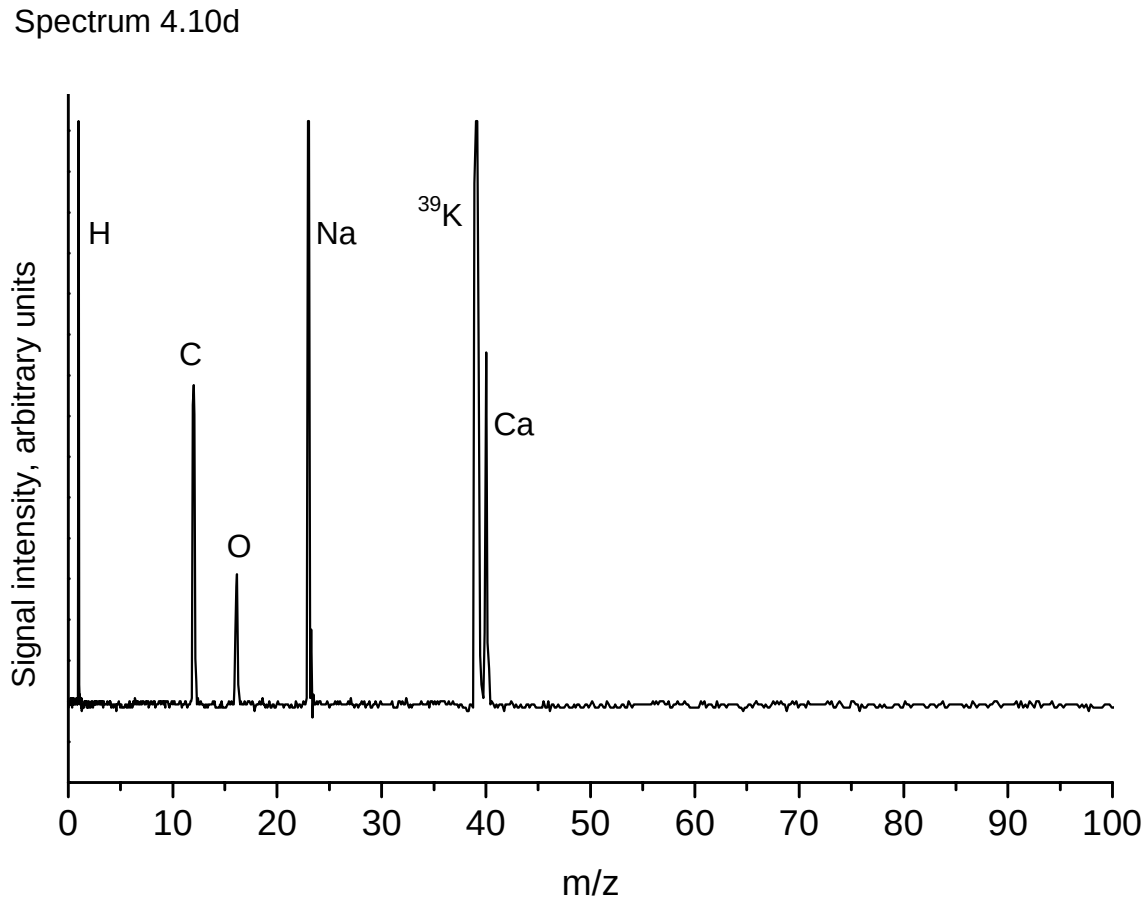

Figure 4.10, continued. Hypervelocity microparticle impact spectra. Spectrum 4.10d was from a 1.7 μm, 2.5 km/s impact.

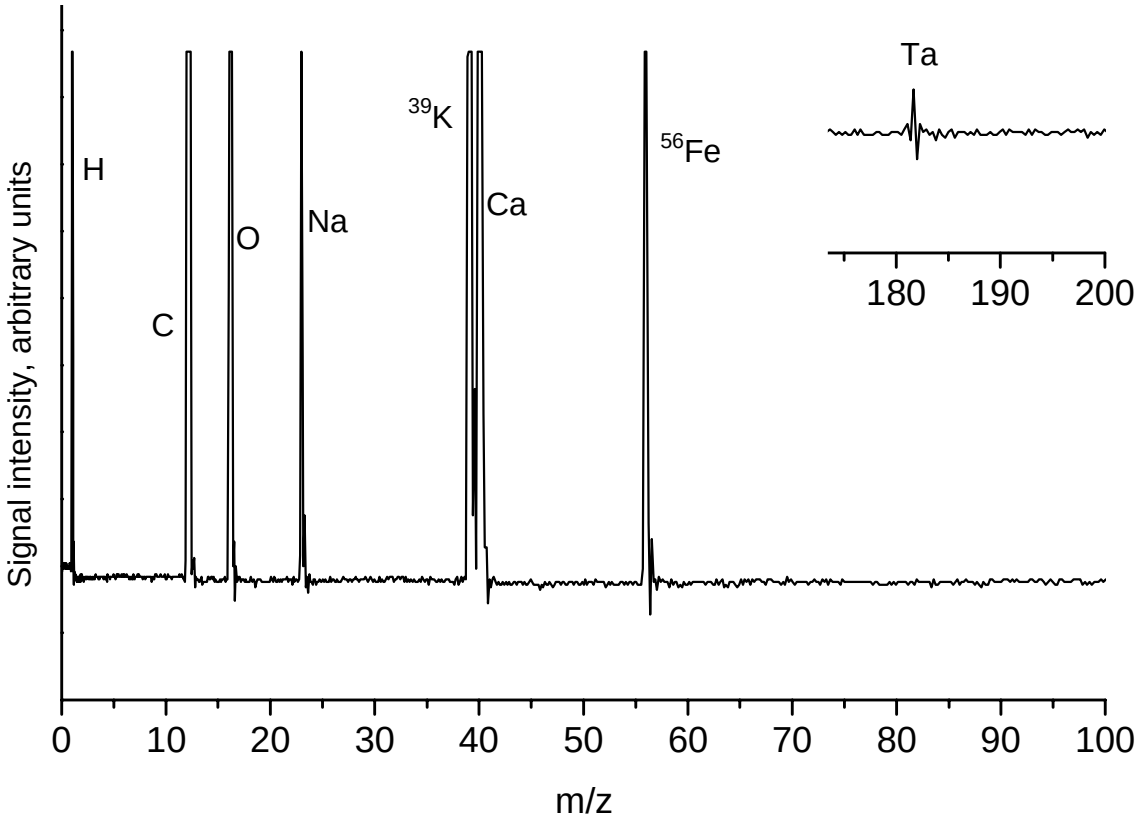

Figure 4.10, continued. Hypervelocity microparticle impact spectra. Spectrum 4.10e was from a 1.7 km/s impact.

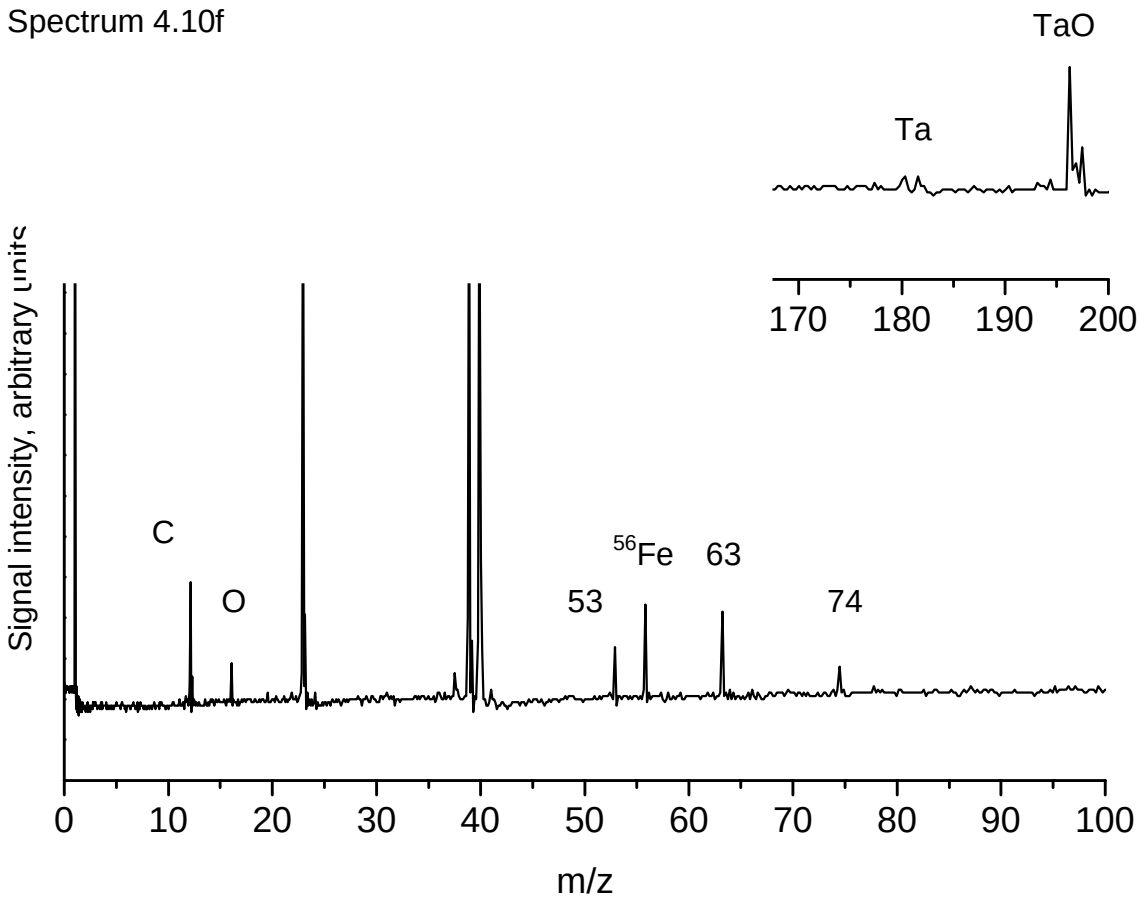

Figure 4.10, continued. Hypervelocity microparticle impact spectra. Spectrum 4.10d was from a 1.4 μm, 3.1 km/s impact.

Spectrum 4.11a

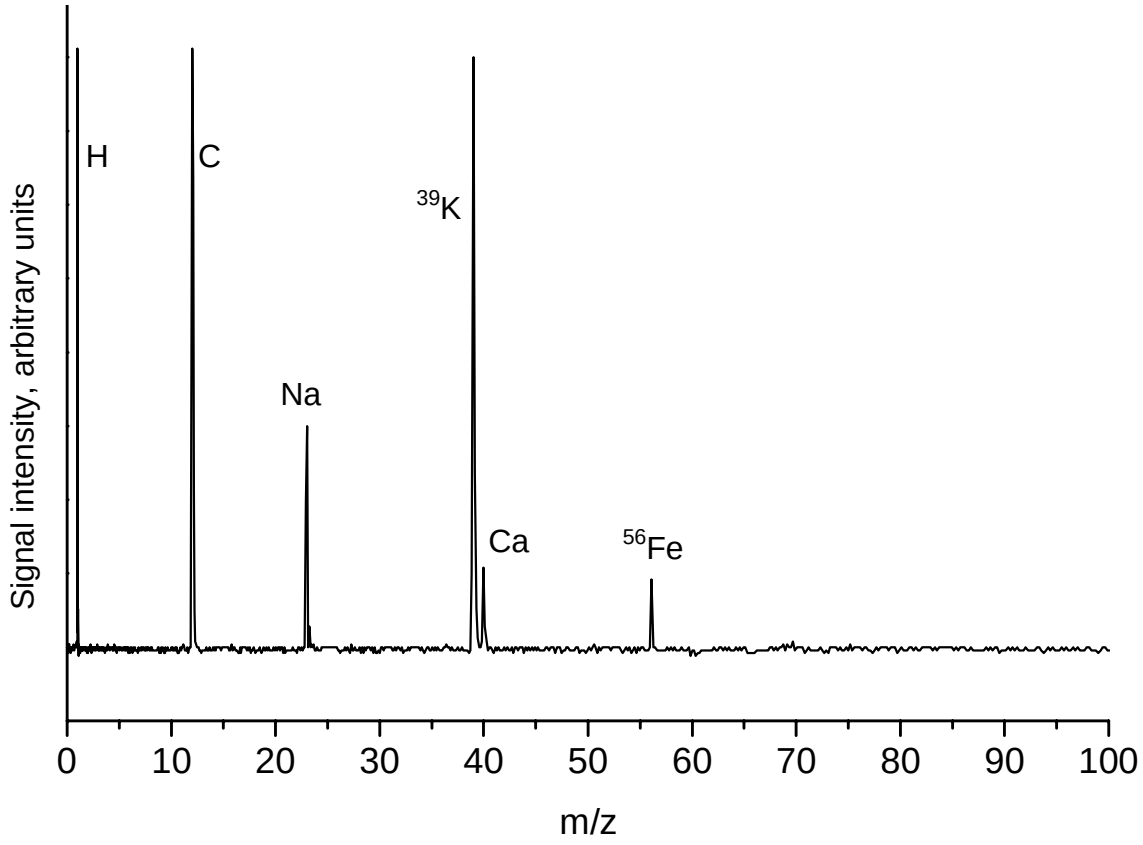

Figure 4.11. Hypervelocity microparticle impact spectra on the Dustbuster. These spectra were produced by particles whose mass and velocity could not be measured. Spectrum 4.11a is from an iron particle.

Spectrum 4.11b

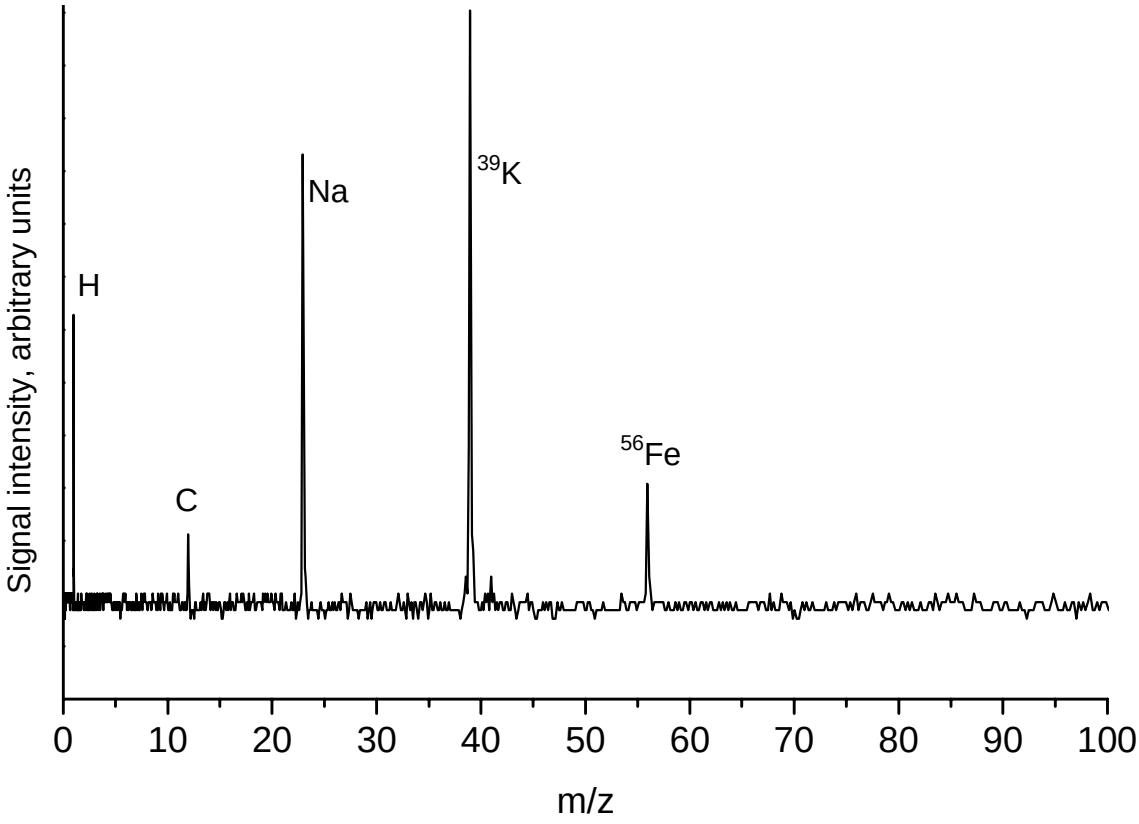

Figure 4.11, continued. Hypervelocity microparticle impact spectra on the Dustbuster. Spectra 4.11b was produced by an iron particles whose mass and velocity could not be measured.

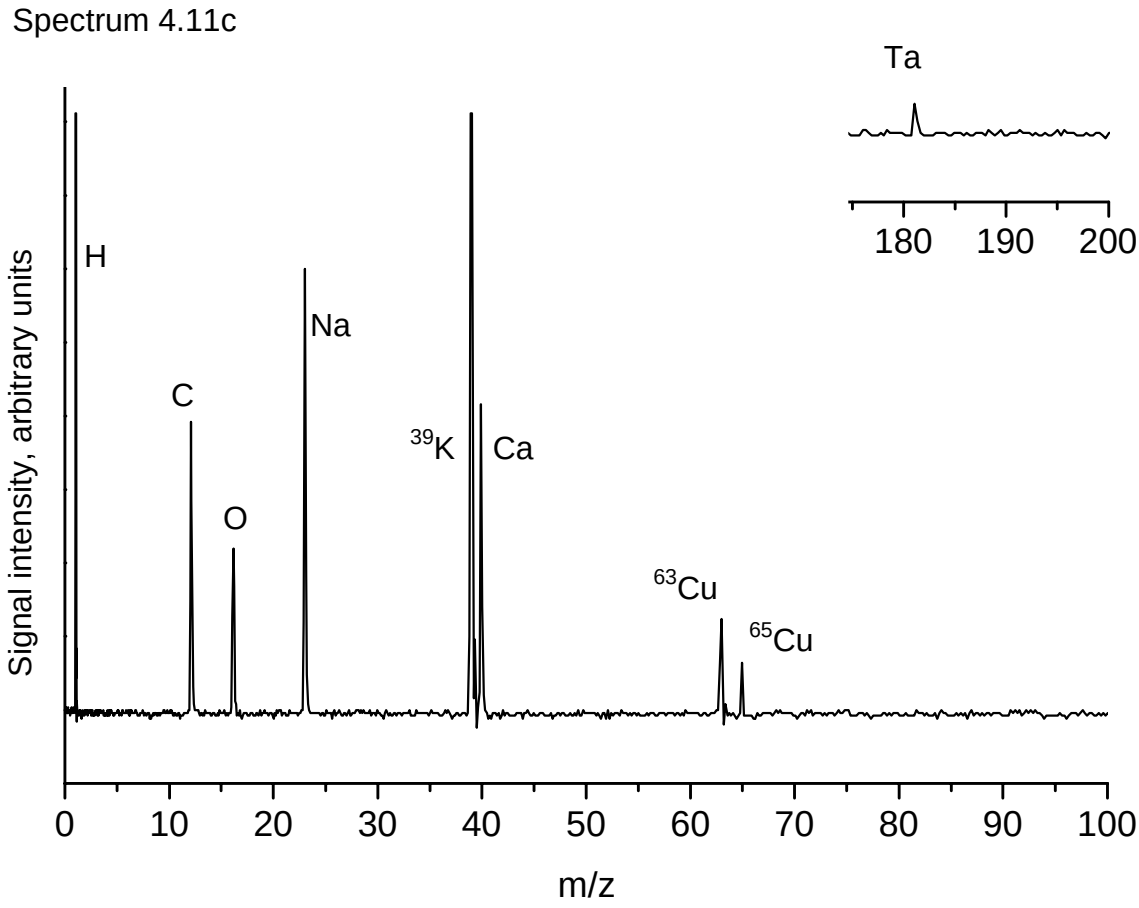

Figure 4.11, continued. Hypervelocity microparticle impact spectra on the Dustbuster. Spectrum 4.11c was a copper particle, unknown velocity or mass.

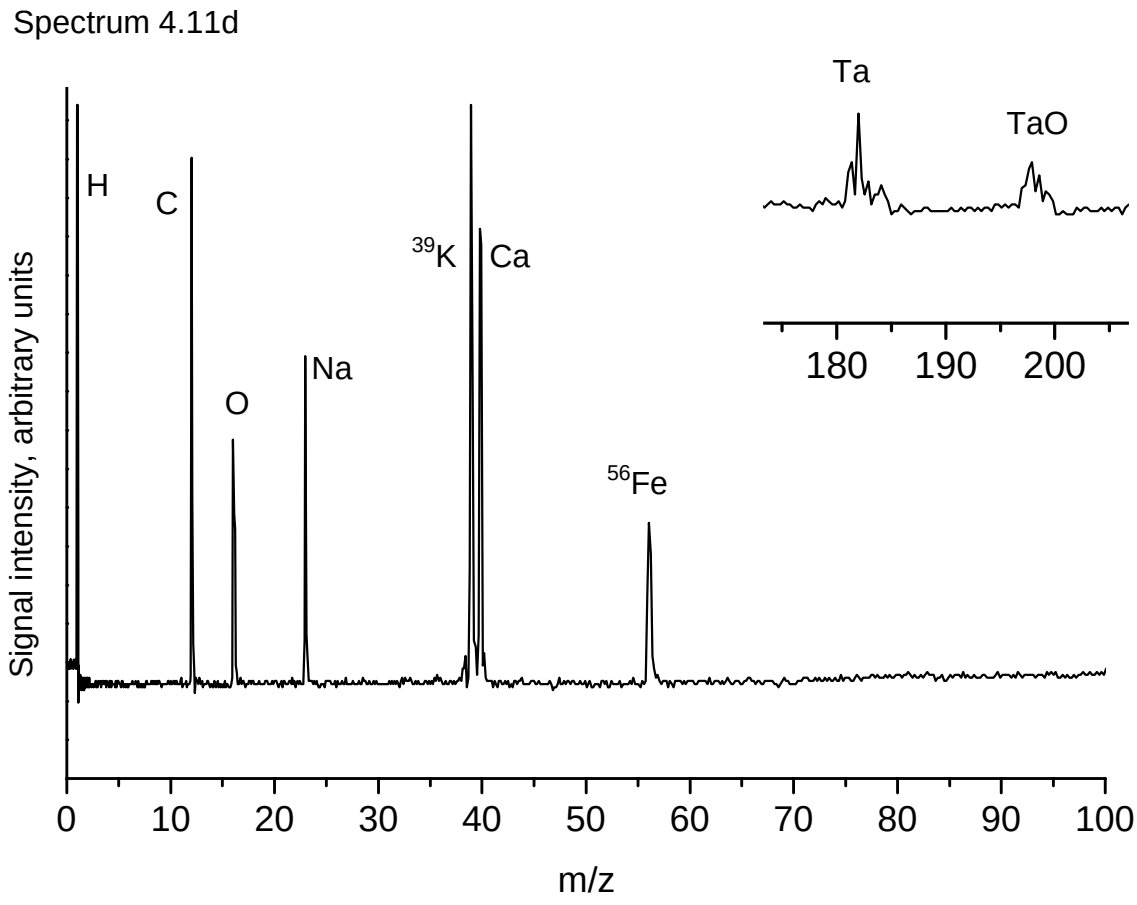

Figure 4.11, continued. Hypervelocity microparticle impact spectra on the Dustbuster. Spectrum 4.11d was an impact of an iron particle with unknown velocity or mass.

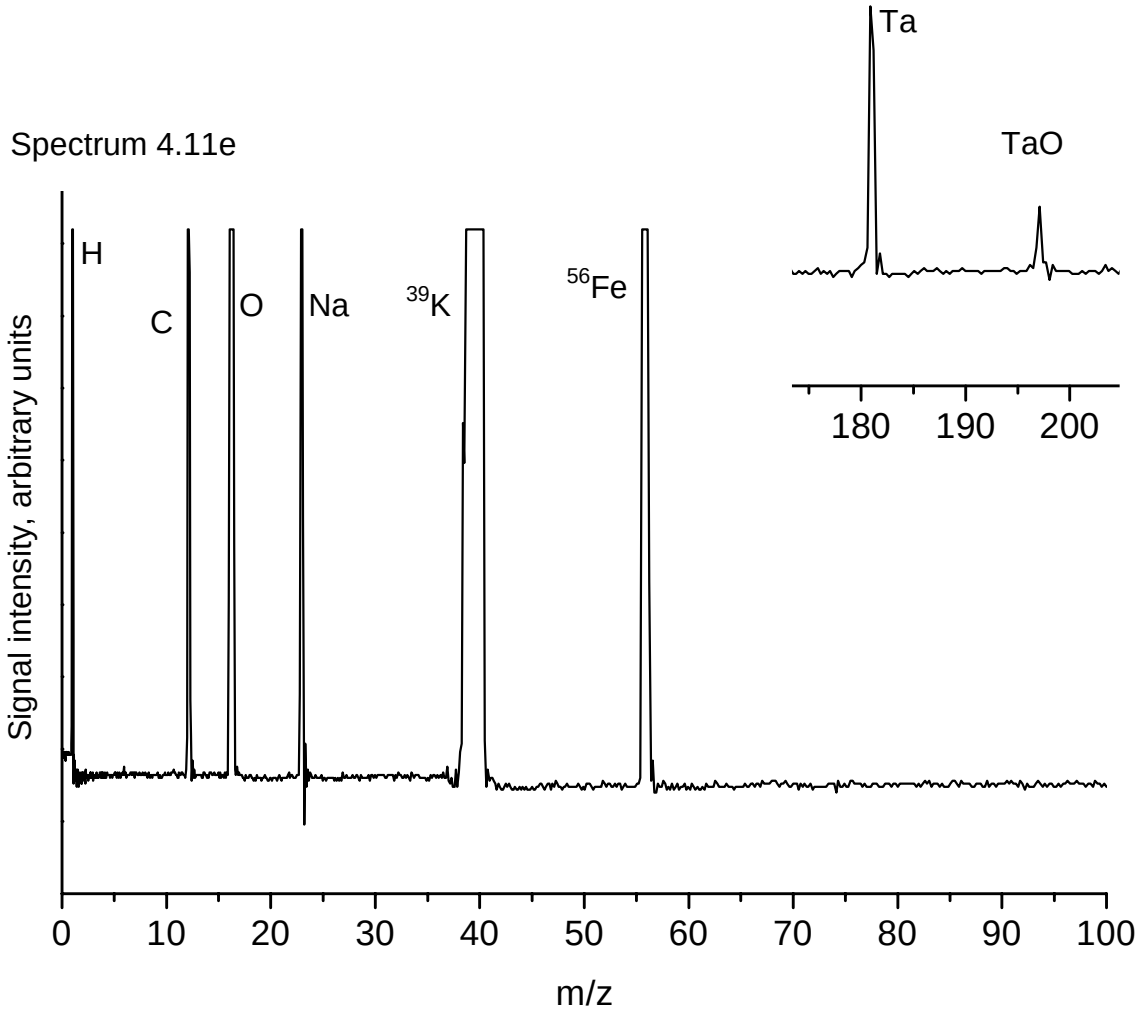

Figure 4.11, continued. Hypervelocity microparticle impact spectra on the Dustbuster from an iron particle with unknown velocity or mass.

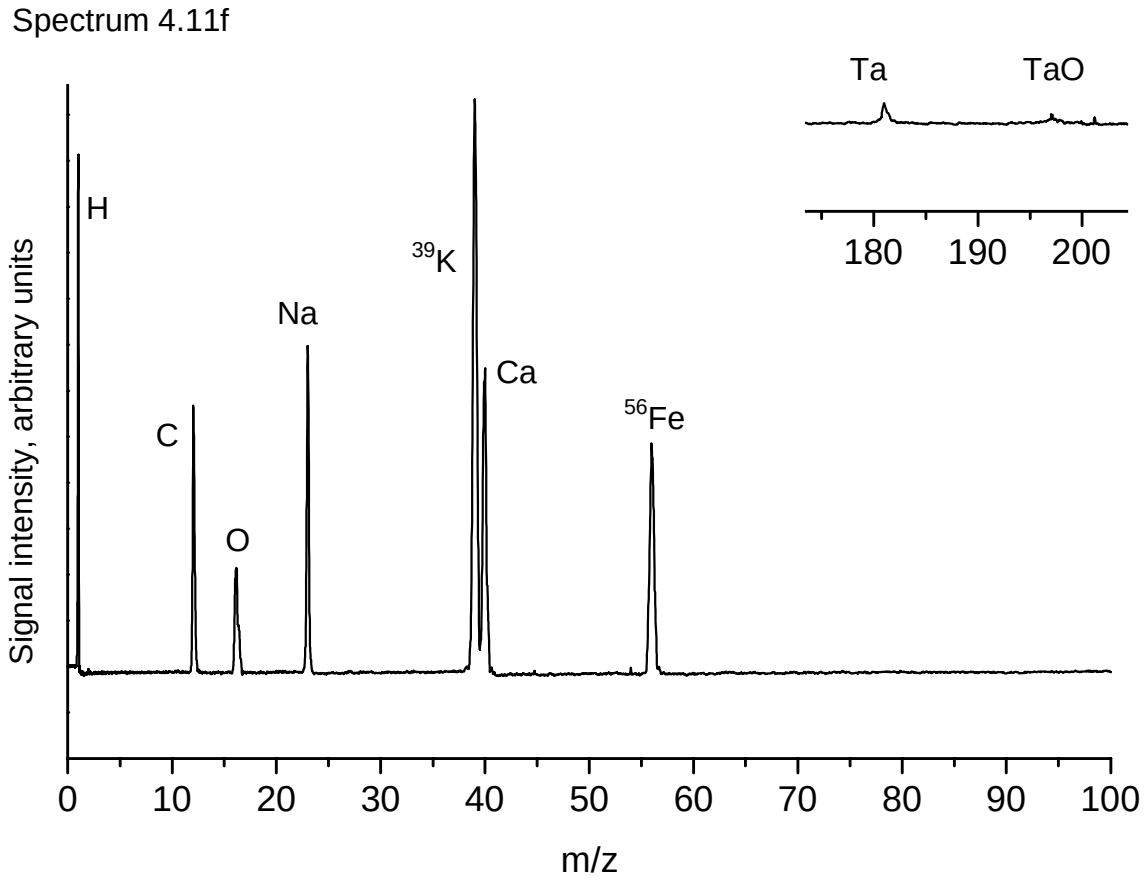

Figure 4.11, continued. Hypervelocity microparticle impact spectra on the Dustbuster from an iron particle with unknown velocity or mass.

of the spectra showed any significant peaks between m/z = 100 and tantalum. Figure 4.11 shows representative spectra produced by particles whose masses and velocities were beyond the detection limits of the cylinder electrodes. Tantalum and tantalum oxide from the target plate material are observed in some spectra. Table 4.1 enumerates all the mass peaks present in at least some of the spectra, and shows the ranges of mass resolution ($m/\Delta m$) for several species. For lighter species, particularly hydrogen, mass resolution is limited by the speed of the recording oscilloscope rather than by a distribution of ion arrival times.

In general, faster particles produced a larger number of ions, consistent with previous results [5]. As expected, neither the incident angle of impact nor the location of the impact on the target plate produced any measurable difference in the mass resolution or other features of the resulting spectra. A statistical analysis of all the spectra failed to detect any correlation between the presence or absence of any specific peaks and the velocities, masses, kinetic energies, or momenta of the impacting particles.

Several correlations exist relating the specific spectral peaks observed. For instance, tantalum (m/z = 181), tantalum oxide (m/z = 197), and a peak at m/z = 40 appear only in those spectra in which carbon and hydrogen are both present. Carbon is always present, and m/z = 40 is generally present in those spectra containing an atomic oxygen peak. H_2^+ appears only when hydrogen is present, but never when iron or copper are present. When hydrogen, carbon, and oxygen are present, their peak intensities are usually in approximately the same ratios.

m/z	% of spectra with given peak	Peak assignment	Mass resolution
1	77	H^+	20-25
2	15	H_2^+	
3	0.6	H_3^+	
7	8	Li^+	
12	59	C^+	50-150
13	0.7	CH^+	
16	28	O^+	
23	98	Na^+	5-200 (typically 100)
27	1.5	Al^+ or $C_2H_3^+$	
28	1.0	CO^+ or Si^+ ?	
39 (41)	99.5	K^+	5-200 (typically 100)
40	37*	Ar^+ , SiC^+ or Ca^+ ?	
56 (54)	16	Fe^+	150-350
63 (65)	8	Cu^+	150-350
181	9	Ta^+	300-600
197	6	TaO^+	

* Peaks may have been obscured by broad potassium lines, hence the occurrence of this peak may be more frequent than indicated.

Table 4.1. Summary of all peaks present in at least 3 impact spectra. Mass resolution ($m/\Delta m$ at FWHM) is given for important peaks.

In most spectra, peak intensities corresponding to minor isotopes, such as $^{41}K^{+}$ and $^{54}Fe^{+}$, were smaller than expected. In some spectra, minor isotopes were absent. For reference, Appendix A lists the natural abundances of all stable isotopes of elements observed in the impact experiments. These isotope anomalies were also seen in laser desorption ionization experiments both by myself (Section 3.3) and by other researchers using similar equipment [36, 37]. Several factors may be responsible for this effect. First, microchannel plate detectors are known to have nonlinear response to isotopes in some situations [38, 39]. Although MCPs have been used for careful isotope ratio measurements, corrections must be made for gain saturation and other effects [40]. In the current experiment minor isotope peaks may have been truncated or improperly sampled. Another possibility is that peaks such as m/z = 56 may have had, in addition to $^{56}Fe^{+}$, an additional contribution from a contaminant such as calcium oxide (CaO^{+}), reducing the expected intensity of other iron isotopes with respect to the principal peak at 56. If this is the case, the m/z = 40 peak may be calcium, which was not expected to be a significant contaminant in this experiment. Insufficient information exists to indicate which of these possible scenarios is responsible for the anomalous intensities of minor isotope peaks in the spectra. For a flight instrument, however, a more linear ion detector would reduce this obstacle to isotope ratio analysis.

Sodium and potassium ion peaks were observed in nearly all spectra. In many of the impacts, these were the only observed ion species. Because of their low ionization potentials (5.139 eV for sodium, 4.341 eV for potassium) and prevalence on metal surfaces, these alkali ion contaminants commonly appear in mass spectrometry involving surface ionization.

The presence or absence of certain mass peaks shows a great deal of variability between similar microparticles. This variability is sufficient to obscure correlations that might exist between measured particle parameters and spectral features. For instance, given two particles identical in mass, composition, charge, and velocity, one may produce significant C, H, and O peaks, while such peaks might be completely absent from the spectrum of the other particle. Figure 4.12 shows an example of this: three 2.6-micron iron particles (before copper dust was added to the dust source) impacting normal to the target, at 2.1 km/s, and in the same region of the target plate produce three different spectra. The origin of this variation in spectra is not clear, but illustrates the dependence of the ionization mechanism on one or more unmeasured variables. These variables may pose significant limitations on estimates of elemental composition from any cosmic dust analyzer of this type.

4.8 Charge transfer and the impact ionization mechanism

Non-metal ion peaks (H^+, C^+, O^+) have been observed in previous impact experiments, although their source is unclear. Ratcliff and Alladhadi [26] saw H^+ and C^+ peaks in their mass spectrum of a 94 km/s boron carbide particle impacting a silver-plated aluminum target. They attributed these peaks to hydrocarbon (pump oil) contamination, but no explanation was given for the lack of hydrocarbon fragment peaks. Hydrogen and carbon have relatively high ionization potentials (13.598 and 11.260 eV, respectively) and typical C-H bond strengths in hydrocarbons are 4 eV. A 9 km/s impact producing 0.4 eV per nucleon does not have sufficient kinetic energy to

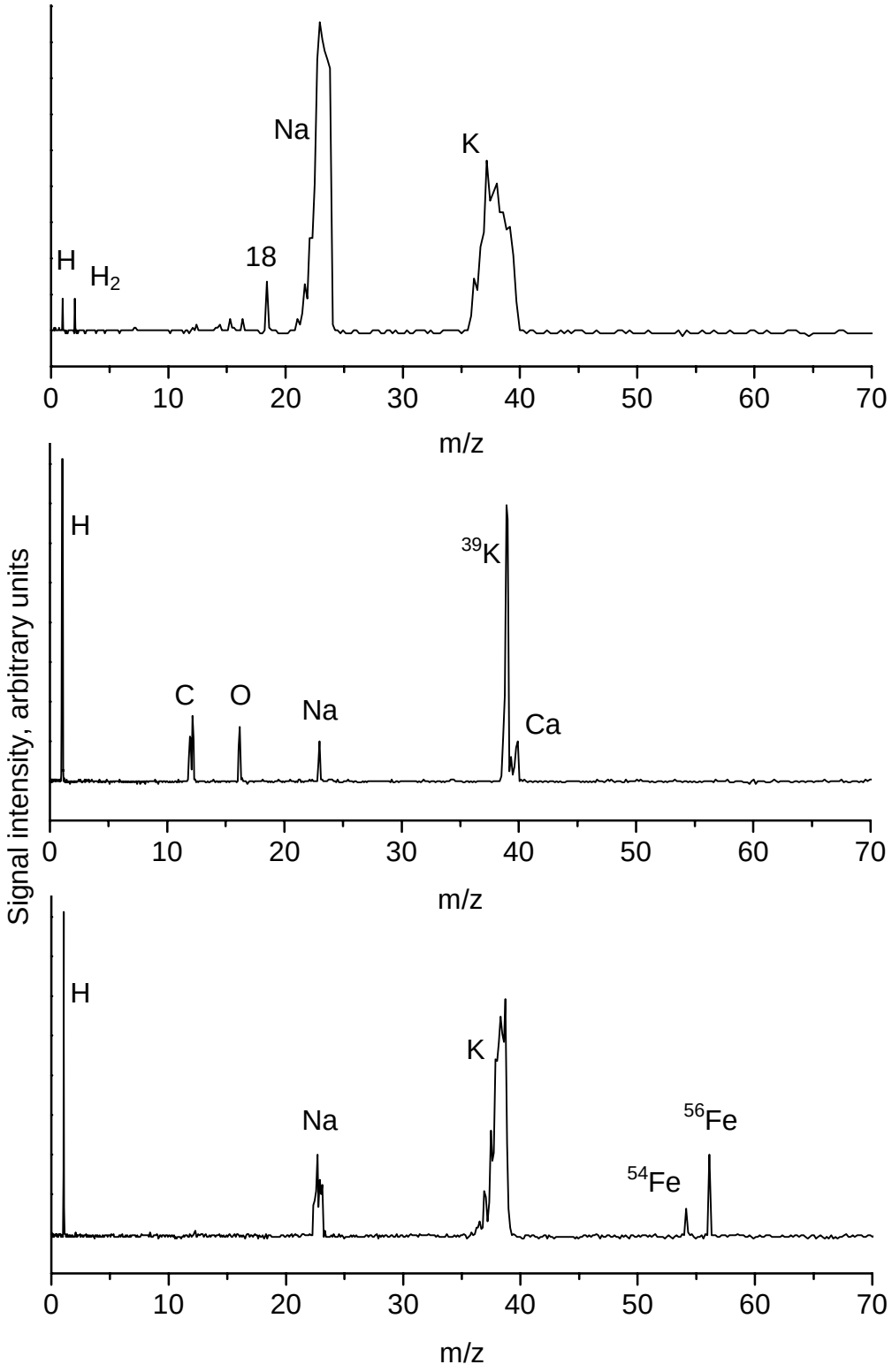

Figure 4.12. Spectra from three 2.5-μm iron particles impacting at 2.1 km/s. Despite identical impact parameters, the spectra produced are very different.

atomize and ionize species with such high bond dissociation and ionization energies [22]. Although the energy required to produce free H^+, C^+, and O^+ is much higher than the impact energy, their presence may be explained by the theory proposed by Novikov [27] and discussed by Sysoev [28, 29] and McDonnell [30]. They postulate that an electric discharge occurs between the charged particle and target surface immediately before impact. According to their model, when the charged microparticle is within approximately 1-2 μm of the surface, the high electric field causes electrons to be emitted from the target surface and strike the particle, causing electron-induced desorption and ionization. In addition, a small spot on the particle surface is strongly heated, causing thermal desorption and ionization of such species as Na and K. This model affects not only laboratory measurements with charged microparticles, but also results from dust particles in space, which are typically charged to potentials of several volts [41].

Burchell and co-workers [42] conducted an experiment in which highly charged hypervelocity microparticles passed through a thin gold-palladium foil prior to impact on a solid plate. Passage through the foil significantly reduced the particle charge, and affected velocity only minimally. Particle velocities were typically below 10 km/s. Particles with reduced charge produced fewer total ions upon impact, supporting Novikov and Sysoyev's model.

As a charged microparticle approaches an impact plate, it induces an image charge, changing the electric field in the region. Agutti [43] developed a model to estimate the capacitance between a charged particle and plate, resulting in Equation 7:

$$\frac{C}{C_0} = \ln\left(\sqrt{\frac{r}{s}}\right) + 1, \tag{7}$$

where r is the particle radius, s is the separation between the particle and the impact plate, and C and C_0 are the induced and free-space capacitance of the system. McDonnell [30] used this result to approximate the electric field, E, between particle and plate as

$$E = \frac{V_0}{s\left(\ln\left(\sqrt{\frac{r}{s}}\right) + 1\right)}, \tag{8}$$

where V_0 is the free-space surface potential on the charged microparticle. As a charged microparticle approaches the impact plate, the electric field increases until it exceeds the field desorption limit for electrons on the impact plate. At this point, electrons are emitted from the plate and strike the microparticle. Sysoev [29] estimated that electron emission begins at a distance of roughly 1-3 microns (for particles with size and charge typical of impact experiments) and continues until physical contact. Presumably, the electric field will not significantly exceed the electron-desorption limit (10^9-10^{10} V/m), although it may stay near that limit until physical contact occurs. Thus the above equations are only approximations valid within a certain range of particle-plate separation distances.

When the microparticle reaches a certain distance from the impact plate, the induced electric field will be sufficient to cancel the externally applied field. When closer than this distance, the microparticle will be accelerated toward the impact plate by the induced field. Figure 4.13 shows an estimate of the total field (using equation 8) felt by the approaching particle as a function of distance for a typical 1-micron particle with

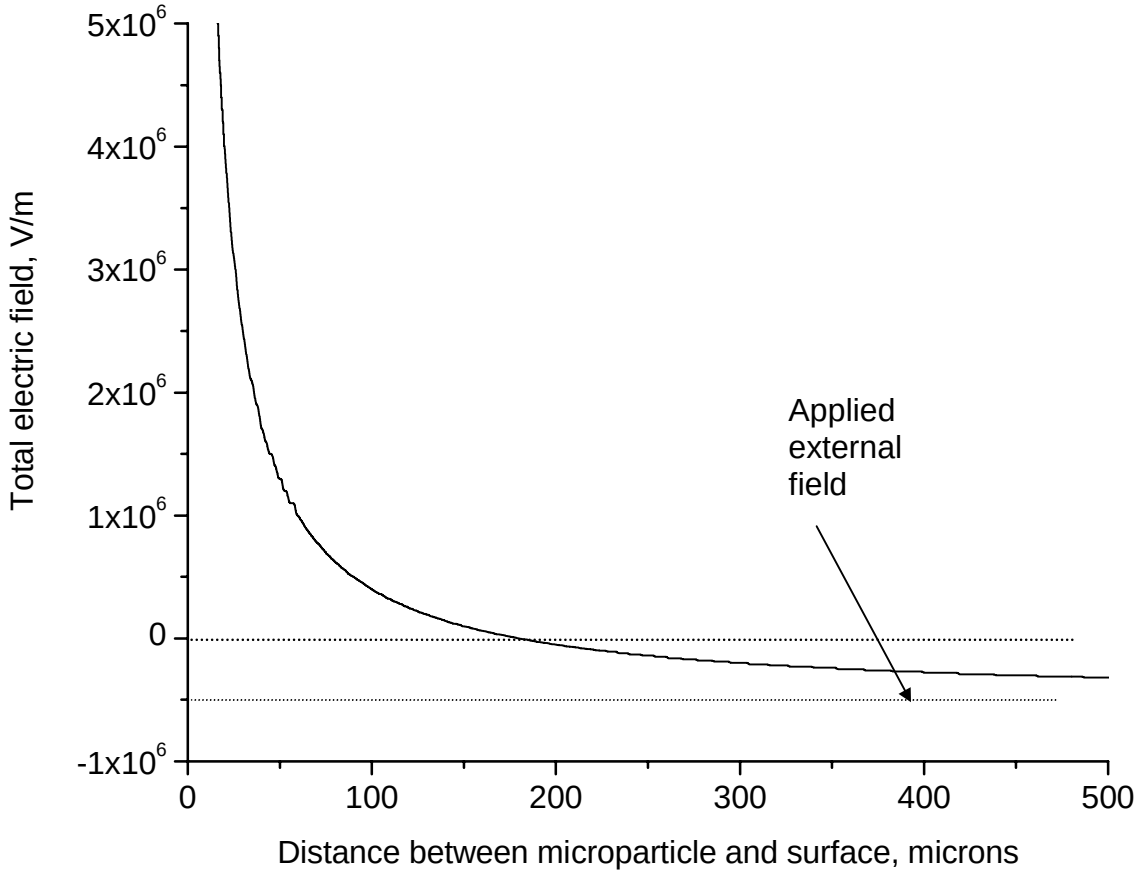

Figure 4.13. Electric field as a function of distance from target for a 1-μm, 1×10^{-14} Coulomb positively charged particle. Applied external field is 5×10^{5} V/m. Positive field is oriented toward impact plate.

1×10^{-14} C charge. At around 175 microns the field reverses direction and pulls the particle into the plate. Any impacting microparticle will thus impact the surface with a slightly higher velocity than that at which it had been traveling.

A more refined approach to this problem involves using dynamic image charge theory [44, 45]. Assuming ideal conductors, the surface charge density, σ, on the impact surface due to a point charge, q, is

$$\sigma = -\frac{1}{4\pi}\frac{\partial \Phi}{\partial z}\bigg|_{z=0} = -\frac{q}{2\pi\left(\rho^2 + d^2\right)^{3/2}}, \tag{9}$$

where Φ is the electrical potential at the surface, $\rho = 0$ is the point on the surface closest to the particle, ρ is the distance from this point along the surface, z is the distance away from the conducting surface, and d is the separation between the surface and the particle ($d = z$) [46]. Neglecting dynamic effects the acceleration on the particle due to the induced potential will be

$$a = \frac{q^2}{16\pi d^2 m \varepsilon_0}, \tag{10}$$

where m is the particle mass, and ε_0 is the permittivity of free space. As the particle nears the surface, however, the charge of the particle will be reduced by electron impact, so the acceleration function is multiplied by a decreasing function, such as an exponential decay [47]. Taking into account the electric field produced by the extraction grid (and using a superposition of solutions to the Laplace equation), the acceleration is reduced by a constant. This constant is the same as the total deceleration of the particle in the extraction region if image charge effects are ignored. Thus the particle impacts at

a velocity higher than its initial velocity, but slower than expected using simple image charge theory.

As the particle approaches the surface the electric field at the impact surface will be enhanced in some regions due to inhomogeneous surface topology. Electron emission will occur sooner than predicted using the value of the electric field calculated for an ideal, planar surface.

As electrons are accelerated toward the microparticle, they in turn induce an image charge on the particle, resulting in a greater impact energy for the electrons. The image charge on the particle is present before electron emission occurs, and increases as electrons approach the particle. To account for the finite particle size, treatment of this situation requires the full image-charge interaction potential rather than the induced dipole approximation [48], resulting in a velocity-dependent solution that can be solved numerically. The electron impact energy has been estimated for very slow electrons [49]. However, in the case of highly charged microparticles, the impact energy will be much greater. The energy with which the first electrons impact the particle surface may be on the order of 200 eV for a 1-micron particle with a charge of 10^{-14} C. In comparison, the average kinetic energy per nucleon for an impact of such a particle at 2 km/s is only 0.02 eV. For higher velocities, the impact kinetic energy increases, while the number and total energy of impacting electrons decreases. Figure 4.14 shows the relative contributions of impact kinetic energy and electron impact in ionization of iron microparticles with surface charge density of 0.005 C/m^2 accelerated to 1.5 MV. Although the magnitudes of both curves are in units of energy, the comparison is not necessarily direct. Electron impact energy affects ionization of surface species, but

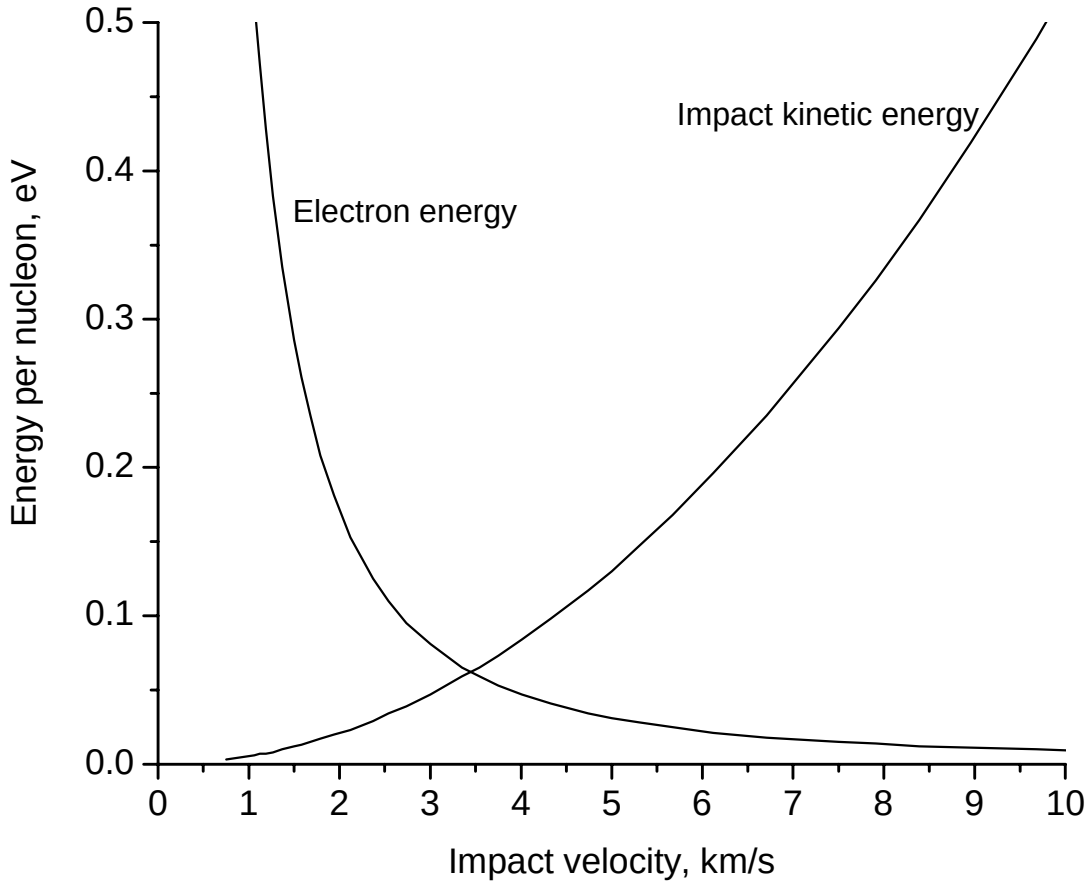

Figure 4.14. Energy dissipated in an impacting microparticle from both impact kinetic energy and from emitted electrons. The ionization efficiency, which is different for each mechanism, is not considered in this figure.

kinetic energy is proportional to the shock wave properties for the entire particle. Thus the curves in the figure show energy dissipated per nucleon. The calculations for this figure assume that electron emission begins at a separation of 3 microns for a 1-micron particle with charge of 1.5×10^{-14} C [29], and that the cube of the distance at which electron emission occurs for other particle sizes is inversely proportional to particle charge. This relation is consistent with the assumption (not used in the calculation) that electrons are emitted by the electric field where

$$E = -\frac{q}{2\pi\varepsilon_0 \left(\rho^2 + d^2\right)^{3/2}} \beta \tag{11}$$

and β is an empirical correction to account for increased electric field due to surface roughness. The calculation further assumes that electron impact energy is dissipated in the outer 10 nm of the surface [29] and that electron emission rates are exponential functions of the particle-surface separation within the emission distance. Determining which factor produces more ions at a given velocity depends on the ionization efficiency of each mechanism, which is much higher for electrons-induced ionization, but is not included in the calculation. Nevertheless, the trends in the figure are useful to illustrate the relative effects of these two ionization mechanisms in different velocity regimes. Note also that this model entirely ignores ionization of the impact plate material, which in some cases can be substantial.

The electron emission model accounts for the high energies needed to atomize and vaporize surface molecules. However, the increase of H, C, and O ions as a function of impact velocity is not explained (at least not with the simplifications used here), and may lie in the details of the electron emission rates, screening, or the impact

of positive ions on the impact surface before the particle impacts. It is interesting to note that H, C, and O ions appear frequently in spark source mass spectrometry.

Figure 4.15 shows the effect of the local electric field caused by the charged particle approaching the impact plate. Note that the ions formed prior to impact are not extracted with the uniform applied electric field, but are subject to the distortions of the induced local field. In fact, positive ions formed on the surface of the microparticle will likely be accelerated back onto the impact plate, creating more ions in a SIMS-like mechanism. These ions, in turn, are also extracted with a non-uniform field, and their fate is an uncertain one. Thus the ionization mechanism and ion trajectories associated with an impact are quite complex.

The foregoing treatment demonstrates that impact ionization is, at lower velocities, largely a surface phenomenon. In the Dustbuster experiments, accelerated particles likely had a surface coating of pump oil, which in this case consisted of tetramethyltetraphenyltrisiloxane. The O^+ peak observed could be caused by oxygen from the pump oil, by metal oxides on the particle surface, or by adsorbed gases, dissociated and ionized by field-emitted electrons prior to impact.

If ionization is enhanced at a particle surface, the quantity and type of ions formed in any given impact will not be representative of the particle composition as a whole. Impact ionization models, such as hydrocode simulations, that neglect electron-induced ionization mechanisms may lead to incorrect interpretations of real impacts involving charged particles [22]. Previous results from comet Halley [15, 16, 19], which showed an excess of H, C, N, and O in the impact mass spectra, may have seen a surface enrichment of these elements caused by sublimation of more volatile surface

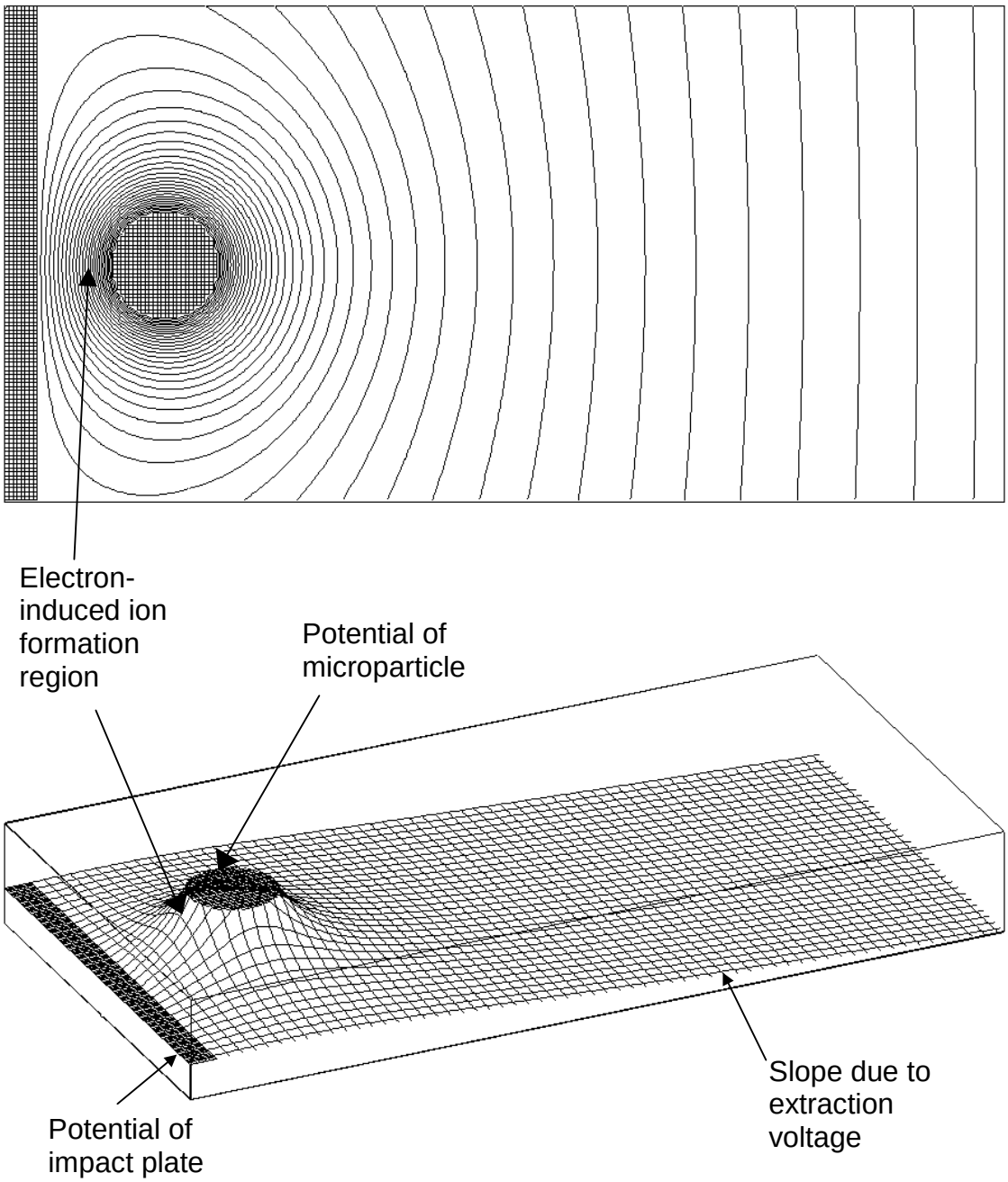

Figure 4.15. Electrostatic potential contours (above) and potential energy surface (below) for highly charged microparticle approaching a planar conducting surface. Note the nature of the potential energy surface at the point at which ions are formed during electron-induced ionization. Ions in this region are accelerated back to the impact plate.

components. The concentration of organics on the particle surfaces may or may not have been representative of the bulk cometary composition.

Both in the Dustbuster and other instruments, electron-induced ionization may also occur as particles pass through grids and come close to a grid wire. For instance, in the Dustbuster, 15% of 1-μm particles pass within 2 μm of a grid wire before they reach the impact target. Inconsistent electrical interactions may produce different mass spectra for otherwise identical particles. Similarly, field emission of electrons from the target plate will vary with the microscale topology of the impact surface. This topology may affect the quantity and nature of ions produced in an impact. Both of these effects have implications for *in situ* flight instruments. Impact cratering of a target plate, which can be extensive in some dust environments, would change the ionizing characteristics of a target plate over time. Also, particle charge measurements are necessary in order to predict the specific ionization mechanism responsible for a given spectrum.

A few other unusual observations deserve comment about the Dustbuster results. As seen in Figures 4.10 and 4.11, some spectra exhibit unusually broad Na^+ and K^+ peaks, although other ion species seem unaffected. Because the Dustbuster uses a reflectron, it is unlikely that these broad peaks are caused by differences in the initial kinetic energies of the ions. More likely, these ions are produced over a longer time scale than the other ions. For broadened peaks from slower impacts (1.5-2.5 km/s), the peak widths correspond to roughly 300 ns, while faster impacts produce less broadening. It is possible that these broad peaks arise from particles that were heated by electron bombardment while passing through the acceleration grid. Such particles would emit sodium and potassium ions all the way through the acceleration region. Computer

simulations of this situation using SIMION ion trajectory software [50] show that only those ions emitted within 300-400 μm of the target plate would have the correct energy and trajectory to reach the ion detector. The combination of being formed early and gaining less kinetic energy would result in an arrival time of about 0-300 ns earlier for these ions, consistent with observations. Of course, this demonstrates only the possibility that peak broadening is caused by thermal emission. The alkali ions might be broadened due to plasma screening, long-duration thermal ionization, or some other unusual effect. In some spectra the potassium peak may be overlapped with calcium, also producing a single, broad peak.

Charge-induced ionization may occur in one other situation of note. As microparticles in a van de Graaff accelerator are charged by the charging needle, a similar charge interaction occurs. In this case, of course, the particle is moving more slowly, and the electrons are moving from the particle to the charging needle (the opposite of the situation during an impact). Shelton [2] reported that the limiting factor in microparticle charging was not the theoretical maximum charge the particle could support. Rather, the charging was limited by the destruction of the charging needle at high voltages. If the charging needle were at a voltage higher than roughly 45 kV, the needle material would be ablated during the charging process. This is the same electron-emission ablation (and possibly ionization) that occurs during impacts. The possible effects of charging on the microparticle have not been explored. An experiment to observe ions formed during this process would be useful to further study the impact ionization process. Another useful experiment would involve deceleration of a charged microparticle immediately prior to impact. This can be accomplished by holding the

impact plate at the same potential (or nearly the same) as the potential at which microparticles are formed. In this case the impact would have insufficient kinetic energy to produce ions, so any ions formed would presumably be the result of the electrical interaction.

As electrons strike the charged microparticle, low-energy bremsstrahlung radiation should be emitted, although this has not been verified experimentally. A treatment on theoretical bremsstrahlung cross sections for electrons striking negatively charged microparticles is given by Jung [51].

4.9 Simulating cometary dust: ice particle impact experiment

Laboratory experiments on accelerated microparticles have been limited to conducting substances. Although most of this work used metal particles, a few experiments reported using metal-coated latex microspheres. However, an important component of cometary debris consists of particles composed largely of ice. Microparticle ice impacts have received little attention.

A similar phenomenon, cluster impact, has been studied in detail. Impacts of neutral water clusters produce charged cluster fragments or free ions based on impact speeds [52]. Positively charged [53] and negatively charged [54] water clusters show similar effects. Water cluster impacts typically involve aggregates with up to around 5000 molecules, corresponding to a particle size of 7 nm. Impacts of larger clusters, usually referred to as massive cluster impact, have been used to produce secondary ions for mass spectrometry [55, 56]. In this case, however, the clusters consisted of glycerol,

and were produced using an electrohydrodynamic gun (similar to electrospray). In fact, a glycerol particle source for massive cluster impact is available commercially from Phrasor Scientific (Azusa, CA). Glycerol or mixtures with glycerol are used because they neither freeze nor boil as they are exposed to vacuum. Williams and Aksyonov [57] have modified this source and produced massive clusters composed of aqueous ammonium acetate. They then accelerated these charged clusters through 8 kV and impacted them on surfaces. Dissolved biomolecules were efficiently ionized, and ammonium acetate complex ions were also observed in large abundance. High concentrations (2 M) of ammonium acetate were required to produce these results. Unfortunately, their experiment included no method to measure the impact velocity of the massive clusters.

We became interested in ice particle impacts when the Dustbuster was being considered for inclusion on the Deep Impact mission. The Deep Impact spacecraft will intercept comet Tempel 1 in July 2005. The Deep Impact spacecraft will "launch" a 370 kg impactor that will collide with the comet at a velocity of 10.2 km/s. The impact will produce a considerable amount of debris, which will be observed by video equipment on the spacecraft. We therefore began a research program aimed at understanding hypervelocity impacts of ice. These studies involved producing highly charged ice particles in vacuum, accelerating them onto the Dustbuster or other mass spectrometer, and observing the ions produced.

Several difficulties were encountered in these efforts. First was the difficulty of introducing water particles into vacuum. Second was finding a way to apply a sufficiently high accelerating voltage without suffering glow discharge problems.

Attempts to introduce electrosprayed microdroplets into vacuum through differential pumping were unsuccessful, probably because of skimmer alignment issues. Attempts to electrospray directly into vacuum were also unsuccessful due to freezing/boiling at the spray tip, and also because of glow discharge from the accelerating voltage. The use of a smaller electrospray tip and different spraying solution might have overcome this obstacle, but this course was not pursued.

Small, charged liquid droplets can be produced using a vibrating orifice aerosol generator (VOAG) [58]. The operational principal of a VOAG is illustrated in Figure 4.16. Water or another liquid is forced through a small orifice, producing a cylinder (jet) of liquid. Because the surface area of a cylinder is greater than the combined surface areas of several spheres with the same volume, the liquid jet is unstable, and tends to break up into droplets. The breakup of liquid jets was observed experimentally as early as 1833 [59], and was the subject of various works by Rayleigh [60, 61]. Rayleigh derived the natural breakup wavelength for a jet of water with diameter, D, as

$$\lambda = 4.508D. \tag{12}$$

In a VOAG, a piezoelectric element superimposes small pressure waves on the jet of liquid corresponding approximately to the natural breakup frequency. The jet of water then breaks up into highly monodisperse droplets. Figure 4.17 shows an example of monodisperse droplets produced using a 15-μm orifice with a piezoelectric frequency of 52 kHz. In this figure, droplets are observed by their disruption of a highly focused HeNe laser beam through which they pass. The laser beam intensity is measured using a fast photodiode, and the resulting signal shows the frequency of droplets formed. Droplet size is determined using the known flow rate and particle frequency.

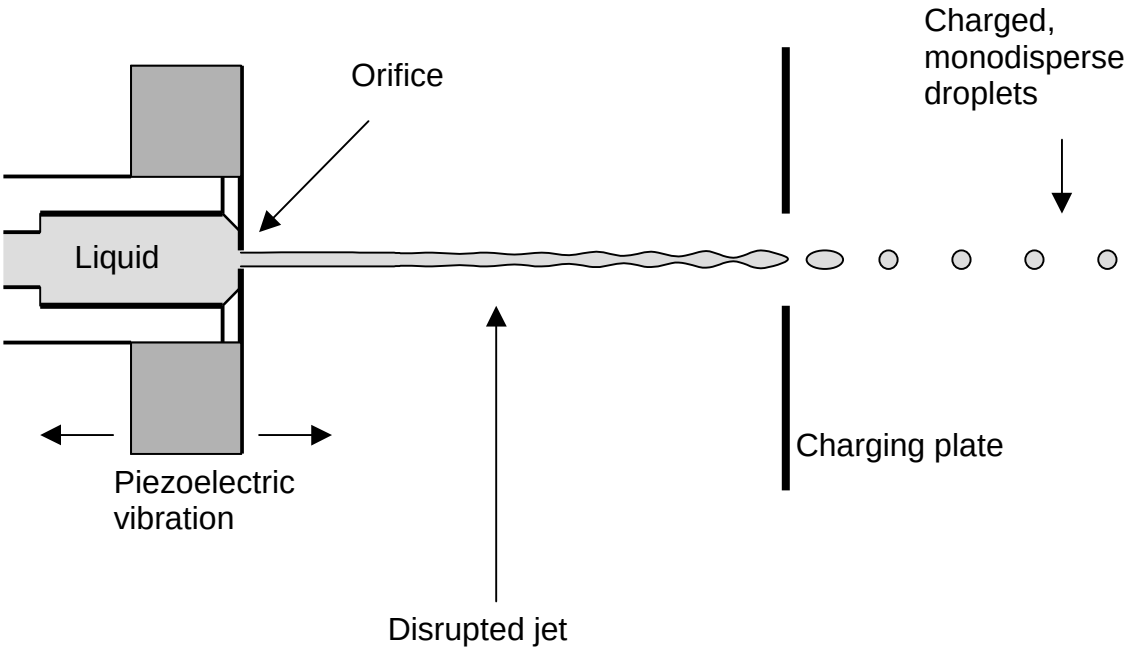

Figure 4.16. A vibrating orifice aerosol generator can be used to produce monodisperse, highly charged water droplets, either at atmospheric pressure or in vacuum.

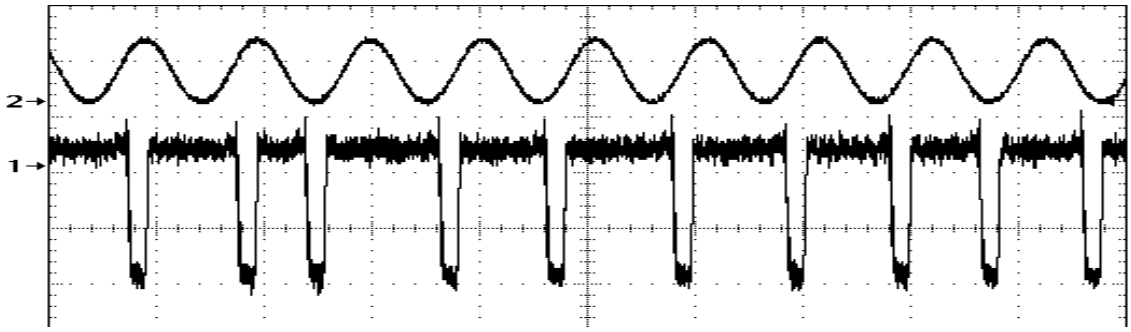

Figure 4.17. Droplets produced using a vibrating orifice aerosol generator are monitored by their obstruction (defocusing) of a HeNe laser beam. Top trace is the peizoelectric driving frequency, 52 kHz. Bottom trace is the signal on a photodiode placed in line with the laser beam. Droplets are produced using a 15-μm orifice, resulting in a particle size of 28 μm.

Droplets formed using a VOAG can be charged simply by placing an electrode in front of the orifice. Due to mechanical constraints, the orifice must be supported on the outside by a metal plate, so the electric field immediately at the orifice is very small. However, the jet of water remains intact for a few mm. The electric field at the end of the continuous jet is the important factor in the charging of the droplets. The charging plate must be placed after the point at which the jet of water breaks up into droplets so that droplet formation takes place within the high electric field.

The vibrating orifice aerosol generator has two main advantages over electrospray for producing highly charged water/ice droplets in vacuum. First of all, the liquid remains in a relatively large body, and is in contact with metal up until the point at which it enters vacuum, allowing better thermal contact with the liquid as compared with a thin column of liquid in an thermally insulating (silica) electrospray tip. The liquid is less likely to freeze before leaving the orifice. Of course, the column of water takes some time to break up, during which time the liquid could freeze and prevent droplet formation. On the other hand, the liquid is moving quickly in a VOAG (typically 5-10 m/s). The second advantage is that the liquid undergoes a sharp pressure gradient at the orifice, so boiling is less of a problem than in electrospray, where the hydrostatic pressure drops gradually near the tip and bubbles often disrupt the spray [57]. One disadvantage of a VOAG is the size range of particles possible. Droplet sizes are generally 1.5 to 3 times the size of the orifice, depending on the flow rate. Orifices are available down to 1 micron, but become more difficult to use with small sizes. In addition, a narrower liquid jet will freeze faster than a thicker jet. Droplet sizes are thus limited to a few microns.

Preliminary experiments have successfully produced 25-μm charged droplets, although no attempts to accelerate the particles have been made at this point.

4.10 Energy analyzer as a high-flux dust mass spectrometer

Despite the marginal success of the energy analyzer (Sections 4.4 and 4.5), it may have an appropriate application in another area. The PIA, PUMA, and CIDA cosmic dust mass spectrometers were designed for environments with high concentrations of dust, such as the vicinity of a comet [15, 62]. However, the large size and mass of these instruments makes them less compatible with NASA's current objectives of smaller, cheaper spacecraft. Smaller time-of-flight mass spectrometers, however, run into limitations of mass resolution. First of all, shortening the instrument can increase deviations from the paraxial approximation. Thus focused ions have greater spherical aberration. Factors related to spherical aberration, such as astigmatism and grid scatter, are also affected. The difference in flight times between ions of different mass is smaller, so focusing must be better to maintain sufficient resolution. Space-charge effects become more important, both because of the need to have narrower arrival time distributions, and also because the physical dimensions of the instrument (and ion beams) are reduced. A smaller instrument requires both faster ion detector response and faster signal amplification and recording, although these are less of an issue thanks to continuing advances in detector technology.

The energy analyzer design overcomes these limitations. Modifications to a flight instrument design might include features shown in Figure 4.18. The instrument

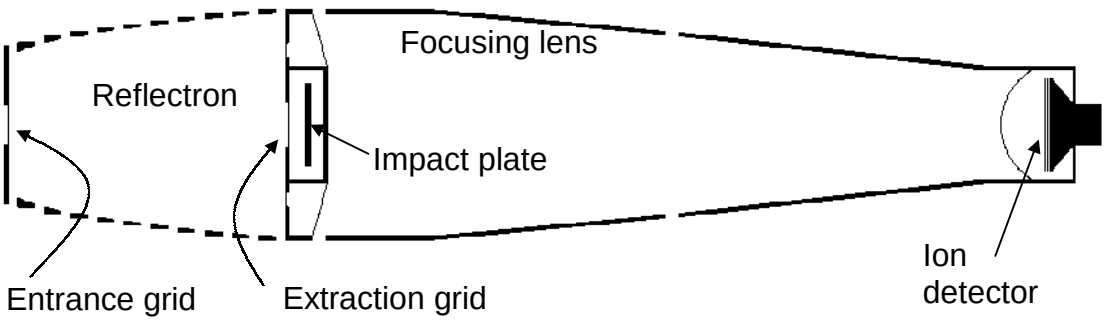

Figure 4.18. Time-of-flight mass spectrometer for high-flux cosmic dust analysis.

has a small (1 cm^2) effective impact area, so it is suitable for dust analysis in regions of the solar system with high concentrations of dust. The set of rings forms an aperture that effectively reduces the spherical aberration of the ion beam to whatever extent is needed to obtain the desired mass resolution. Of course, the narrower the window of admitted ions, the lower the instrument sensitivity. However, dust impacts typically produce a sufficiently large number of ions that even a tenfold reduction in ion transmission will still yield strong signal [5, 7, 10, 63]. By allowing a ring of ions to traverse the drift tube, space-charge effects are much less than they would be if the ions were focused into a narrower beam.

An additional feature of this instrument design is that the ion detector is completely protected from stray particles and radiation that might otherwise cause damage.

One problem encountered by the PIA and PUMA instruments is that of target cratering. The more micro-craters are produced by impacts, the less homogeneous becomes the ion extraction field. This inhomogeneity produces essentially the same effect as grid scatter: the ion beam spreads out laterally. PIA and PUMA remedied this problem by using a scrolling impact plate: a fresh impact surface would replace a plate that had become too cratered for proper ion focusing. The proposed instrument solves this problem another way: the ring aperture filters out any lateral spread, whether from the distribution of initial kinetic energies, grid scatter, or inhomogeneities in the extracting field. Thus the impact plate can become extensively cratered without affecting instrument performance.

The modified energy analyzer design has been evaluated using SIMION 7.0 ion trajectory software [50]. For simulations the instrument dimensions were as follows: length 28 cm, diameter 6 cm, sensitive area of impact plate 1 cm^2. Ions originated on the impact plate at the center, and at radii of 0.2, 0.4, and 0.55 cm. Groups of 500 ions at each location were defined to have mass of 100 amu, initial kinetic energy of 25 ± 15 eV, and a *cos* θ angular distribution about the normal. Figure 4.19 shows typical simulated ion trajectories under these conditions. Figure 4.20 shows an enlargement of ions with m/z 200 and 201 as they approach the detector. Mass resolution ($m/\Delta m$) of simulated ions was 350-400, sufficient to resolve isotopes of any element. Resolution was not reduced for ions originating away from the center of the impact plate, although the number of ions reaching the detector was reduced. Including a slight curvature to the impact plate improved this situation in simulations. For most simulations 10-15% of ions reached the detector, assuming 70% transmission for the extraction grid and 95% transmission for all other grids. Narrowing the ring aperture such that 5% of ions reached the detector resulted in a simulated mass resolution of around 600. The results of these simulations are consistent with observations using hypervelocity microparticle impacts on the energy analyzer.

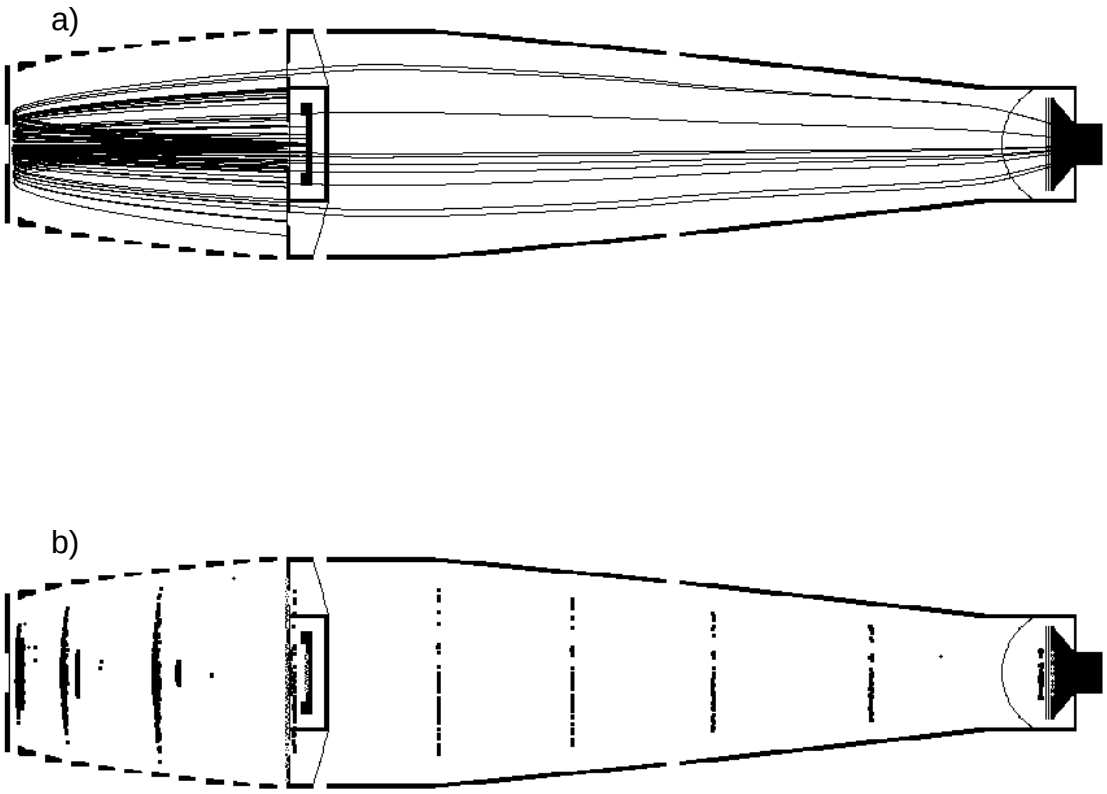

Figure 4.19. Simulated ion trajectories on proposed instrument. Diagram b) shows locations of ions at time intervals of 0.4 μs.

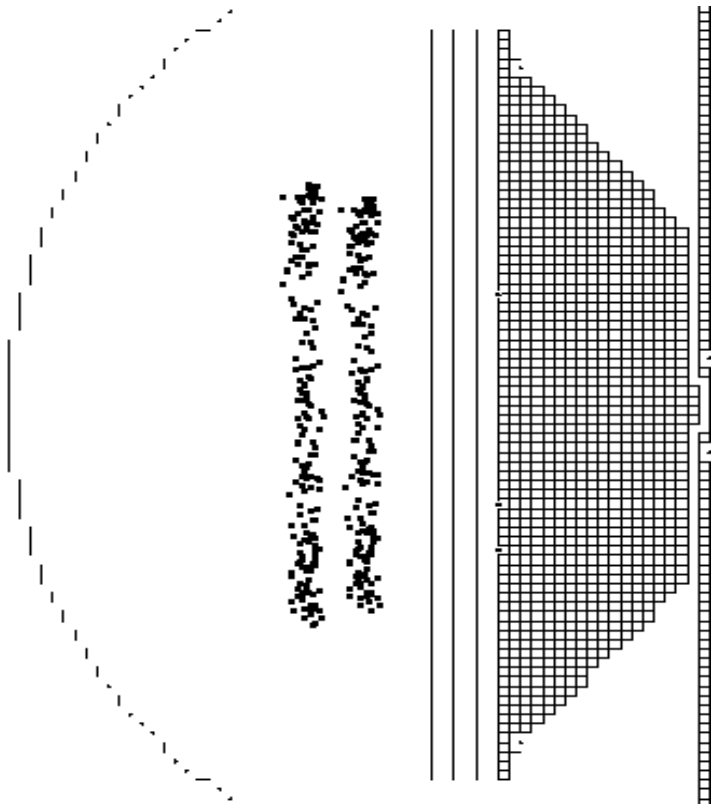

Figure 4.20. Ions of mass 200 and 201 reaching the detector of the high-flux dust analyzer.

References

1. Fair, H., *Hypervelocity then and now.* Int J Impact Engng, 1987. **5**: p. 1-11.
2. Shelton, H.; Hendricks, C. D., Jr.; Wuerker, R. F., *Electrostatic acceleration of microparticles to hypervelocities.* J Appl. Phys., 1960. **31**(7): p. 1243-1246.
3. Friichtenicht, J. F., *Two-million-volt electrostatic accelerator for hypervelocity research.* Review of Scientific Instruments, 1962. **33**(2): p. 209-212.
4. Shibata, H.; Kobayashi, K.; Iwai, T.; Hamabe, Y.; Sasaki, S.; Hasegawa, S.; Yano, H.; Fujiwara, A.; Ohashi, H.; Kawamura, T.; Nogami, K.-i., *Microparticle acceleration by a van de Graaff accelerator and application to space and material sciences.* Radiation Physics and Chemistry, 2001. **60**: p. 277-282.
5. Friichtenicht, J. F., *Micrometeoroid simulation using nuclear accelerator techniques.* Nuclear Instruments and Methods, 1964. **28**: p. 70-78.
6. Auer, S. and Sitte, K., *Detection technique for micrometeoroids using impact ionization.* Earth and Planetary Science Letters, 1968. **4**: p. 178-183.
7. Hansen, D. O., *Mass analysis of ions produced by hypervelocity impact.* Applied Physics Letters, 1968. **13**(3): p. 89-91.
8. Friichtenicht, J. F.; Roy, N. L.; Becker, D. G. *The Cosmic Dust Analyzer: experimental evaluation of an impact ionization model*. in *International Astronomical Union Colloquium #13*. 1971. State University of New York, Albany, NY: Scientific and Technical Information Office, NASA, Washington, D.C.
9. Dietzel, H.; Neukum, G.; Rauser, P., *Micrometeroid simulation studies on metal targets.* Journal of Geophysical Research, 1972. **77**(8): p. 1375-1395.
10. Roy, N. L., *Research Investigations of the Physical Interactions and Phenomena Associated with Hypervelocity Sub-micron Particles*. 1975, TRW Systems Group: Redondo Beach, CA. p. 67.
11. Sutton, G. W. and Sherman, A., *Engineering Magnetohydrodynamics*. 1965, New York: McGraw Hill.

12. Perkins, M. A.; Simpson, J. A.; Tuzzolino, A. J., *A cometary and interplanetary dust experiment on the Vega spacecraft missions to Halley's Comet.* Nuclear Instruments & Methods in Physics Research, Section A: Accelerators, Spectrometers, Detectors, and Associated Equipment, 1985. **239**: p. 310-323.

13. Kissel, J. and Krueger, F. R., *Ion formation by impact of fast dust particles and comparison with related techniques.* Applied Physics A: Solids and Surfaces, 1987. **42**: p. 69-85.

14. Kissel, J. and Kreuger, F., *Time-of-flight mass spectrometric analysis of ion formation in hypervelocity impact of organic polymer microspheres: comparison with secondary ion mass spectrometry, 252Cf mass spectrometry and laser mass spectrometry.* Rapid Communications in Mass Spectrometry, 2001. **15**: p. 1713-1718.

15. Kissel, J.; Sagdeev, R. Z.; Bertaux, J. L.; Angarov, V. N.; Audouze, J.; Blamont, J. E.; Buchler, K.; Evlanov, E. N.; Fechtig, H.; Fomenkova, M. N.; von Hoerner, H.; Inogamov, N. A.; Khromov, V. N.; Knabe, W.; Krueger, F. R.; Langevin, Y.; Leonas, V. B.; Levasseur-Regourd, A. C.; Managadze, G. G.; Podkolzin, S. N.; Shapiro, V. D.; Tabaldyev, S. R.; Zubkov, B. V., *Composition of Comet Halley dust particles from Vega observations.* Nature (London), 1986. **321**: p. 280-282.

16. Kissel, J.; Brownlee, D. E.; Buchler, K.; Clark, B.; Fechtig, H.; Grun, E.; Hornung, K.; Igenbergs, E. B.; Jessberger, E. K.; Kreuger, F.; Kuczera, H.; McDonnell, J. A. M.; Morfill, G. E.; Rahe, J.; Schwehm, G.; Sekanina, Z.; Utterback, N. G.; Volk, H. J.; Zook, H. A., *Composition of Comet Halley particles from Giotto observations.* Nature (London), 1986. **321**: p. 336-337.

17. Lawler, M. E.; Brownlee, D. E.; Temple, S.; Wheelock, M. M., *Iron, magnesium, and silicon in dust from comet Halley.* Icarus, 1989. **80**: p. 225-242.

18. Kissel, J. and Krueger, F. R., *Mass-spectrometric in situ studies of cometary organics for P/Halley and options for the future.* Advances in Space Research, 1995. **15**(3): p. (3)59-(3)63.

19. Kissel, J. and Kreuger, F. R., *The organic component in dust from Comet Halley as measured by the PUMA mass spectrometer o board Vega 1.* Nature (London), 1987. **326**: p. 755-760.

20. Hornung, K. and Kissel, J., *On shock wave impact ionization of dust particles.* Astronomy and Astrophysics, 1994. **291**: p. 324-336.

21. Hornung, K.; Malama, Y. G.; Thoma, K., *Modeling of the very high velocity impact process with respect to in situ ionization measurements.* Advances in Space Research, 1996. **17**(12): p. (12)77-(12)86.

22. Hornung, K.; Malama, Y. G.; Kestenboim, K. S., *Impact vaporization and ionization of cosmic dust particles.* Astrophysics and Space Science, 2000. **274**: p. 355-363.

23. Krueger, F. R., *Ion formation by high- and medium-velocity dust impacts from laboratory measurements and Halley results.* Advances in Space Research, 1996. **17**(12): p. (12)71-(12)75.

24. Abramov, V. I.; Bandura, D. R.; Ivanov, V. P.; Sysoev, A. A., *Energy and angular characteristics of ions emitted in the impact of accelerated dust particles on a target.* Sov. Tech. Phys. Lett., 1991. **17**(3): p. 194-195.

25. Ratcliff, P. R.; Reber, M.; Cole, M. J.; Murphy, T. W.; Tsembelis, K., *Velocity thresholds for impact plasma production.* Advances in Space Research, 1997. **20**(8): p. 1471-1476.

26. Ratcliff, P. R. and Allahdadi, F., *Characteristics of the plasma from a 94 km/s microparticle impact.* Advances in Space Research, 1996. **17**(12): p. (12)87-(12)91.

27. Novikov, L. S.; Semkin, N. D.; Kulikauskas, V. S.; Semenchuk, S. M.; Kiryukhin, V. P., *Mass spectrometry of ions emitted in collisions of accelerated dust particles with target.* Sov. Phys. Tech. Phys., 1988. **33**(6): p. 680-682.

28. Sysoev, A. A.; Bandura, D. R.; Ivanov, V. P., *Mechanism of ionization in a low-velocity collision of charged microparticles.* Sov. Tech. Phys. Lett., 1992. **18**(8): p. 486-488.

29. Sysoev, A. A.; Ivanov, V. P.; Barinova (Komova), T. V.; Surkov, Y. A., *Mass spectra formation from charged microparticles.* Nuclear Instruments & Methods in Physics Research, Section B: Beam Interactions with Materials and Atoms, 1997. **122**: p. 79-83.

30. McDonnell, J. A. M.; Aguti, E. D.; Willis, M. J. *Pre-contact microdischarge from charged particulates*. in *Proceedings of the 7th Spacecraft Charging Technology Conference, 23-27 April 2001*. 2001. Noordwijk, The Netherlands: European Space Agency.

31. Simpson, J. A., *Design of retarding field energy analyzers.* Rev. Sci. Instrum., 1961. **32**(12): p. 1283-1293.

32. Roberts, R. H., *Design details for a small cylindrical mirror analyzer.* Journal of Physics E: Scientific Instruments, 1982. **15**: p. 382-385.

33. Stenzel, R. L.; Williams, R.; Agüero, R.; Kitazaki, K. L., A; McDonald, T.; Spitzer, J., *Novel directional ion energy analyzer.* Review of Scientific Instruments, 1982. **53**(7): p. 1027-1031.

34. Kang, H. and Beauchamp, J. L., *Pulsed laser evaporation and ionization of solid metal targets. Implications for studying the gas-phase reactions of laser-generated atoms and ions.* Journal of Physical Chemistry, 1985. **89**: p. 3364-3367.

35. Cotter, R. J., *Time-of-flight Mass Spectrometry*. 1997, Washington, D. C.: American Chemical Society. 326.

36. Jyoti, G.; Gupta, S. C.; Ahrens, T. J.; Kossakovski, D.; Beauchamp, J. L., *Mass spectrometer calibration of high velocity impact ionization based cosmic dust analyzer.* International Journal of Impact Engineering, 1999. **23**: p. 401-408.

37. Jyoti, G.; Gupta, S. C.; Ahrens, T. J.; Kossakovski, D.; Beauchamp, J. L., eds. *Mass spectrometer calibration of cosmic dust analyzer*. Shock Compression of Condensed Matter, ed. Furnish, M. D.; Chhabildas, L. C.; Hixson, R. S. 1999, American Institute of Physics.

38. Odom, R. W. and Schueler, B., *Laser Microprobe Mass Spectrometry: Ion and Neutral Analysis*, in *Lasers and Mass Spectrometry*, Lubman, D. M., Editor. 1990, Oxford University Press: New York. p. 103-137.

39. Giudicotti, L.; Bassan, M.; Pasqualotto, R.; Sardella, A., *Simple analytical model of gain saturation in microchannel plate devices.* Rev. Sci. Instrum., 1993. **65**(1): p. 247-258.

40. Maechling, C. R.; Clemett, S. J.; Zare, R. N., *13C/12C ratio measurements of aromatic molecules using photoionization with TOF mass spectrometry.* Chemical Physics Letters, 1995. **241**: p. 301-310.

41. Kimura, H. and Mann, I., *The electric charging of interstellar dust in the solar system and consequences for its dynamics.* Astrophysical Journal, 1998. **499**(454-462).

42. Burchell, M. J.; Cole, M. J.; McDonnell, J. A. M., *Role of particle charge in impact ionization by charged microparticles.* Nuclear Instruments & Methods in Physics Research, Section B: Beam Interactions with Materials and Atoms, 1998. **143**: p. 311-318.

43. Agutti, E. D., *Charged Particles in GEO: The Role of Electrostatic Charge in Particulate Impacts on the GORID Dust Detector*. 1999, Masters Thesis, University of Kent, Canterbury.

44. Ray, R. and Mahan, G. D., *Dynamical image charge theory.* Physics Letters A, 1972. **42A**(4): p. 301-302.

45. Sahni, V. and Bohnen, K.-P., *Image charge at a metal surface.* Physical Review B, 1985. **31**(12): p. 7651-7661.

46. Eyges, L., *The Classical Electromagnetic Field*. 1972, New York: Dover.

47. Setterland, C. J. and Barany, A., *Theoretical study of image charge acceleration of highly charged ions in front of a metal surface.* Nuclear Instruments & Methods in Physics Research, Section B: Beam Interactions with Materials and Atoms, 1995. **98**: p. 407-409.

48. Kasperovich, V.; Wong, K.; Tikhonov, G.; Kresin, V. V., *Electron capture by the image charge of a metal nanoparticle.* Physical Review Letters, 2000. **85**(13): p. 2729-2732.

49. Jung, Y.-D., *Image charge effects on electron capture by dust grains in dusty plasmas.* Physical Review E, 2001. **64**: p. 017401.

50. Dahl, D. A., *SIMION 3D*. 2000, Idaho National Engineering and Environmental Laboratory: Idaho Falls, ID.

51. Jung, Y.-D., *Image charge effects on bremsstrahlung radiation from electron-dust grain scatterings in dusty plasmas.* Physics of Plasmas, 1999. **6**(8): p. 3396-3399.

52. Andersson, P. U. and Pettersson, J. B. C., *Ionization of water clusters by collisions with graphite surfaces.* Zeitschrift fur Physik D, 1997. **41**: p. 57-62.

53. Matthew, M. W.; Buehler, R. J.; Ledbetter, M.; Friedman, L., L*arge, energetic cluster impacts on surfaces.* Nuclear Instruments & Methods in Physics Research, Section B: Beam Interactions with Materials and Atoms, 1986. **14**: p. 448-460.

54. Andersson, P. U. and Pettersson, J. B. C., *Water cluster collisions with graphite surfaces: angular-resolved emission of large cluster ions.* Journal of Physical Chemistry, 1998. **102**: p. 7428-7433.

55. Fabris, D.; Wu, Z.; Fenselau, C. C., *Massive cluster impact ionization on a four sector tandem mass spectrometer.* Journal of Mass Spectrometry, 1995. **30**: p. 140-143.

56. Mahoney, J. F.; Perel, J.; Ruatta, S. A.; Martino, P. A.; Husain, S.; Lee, T. D., Rapid Communications in Mass Spectrometry, 1991. **5**: p. 441.

57. Aksyonov, S. and Williams, P., *Impact desolvation of electrosprayed microdroplets - a new ionization method for mass spectrometry of large biomolecules.* Rapid Communications in Mass Spectrometry, 2001. **15**(21): p. 2001-2006.

58. Berglund, R. N. and Liu, B. Y. H., *Generation of monodisperse aerosol standards.* Environmental Science and Technology, 1973. **7**(2): p. 147-153.

59. Savart, Annales de Chimie (Paris), 1833. **t. liii**.

60. Rayleigh, L., Proceedings of the Royal Society of London, 1879. **29**: p. 71.

61. Rayleigh, L., Proceedings of the London Mathematical Society, 1878. **10**: p. 4.

62. Ratcliff, P. R.; McDonnell, J. A. M.; Firth, J. G.; Grun, E., *The Cosmic Dust Analyzer.* J. British Interplanetary Soc., 1992. **45**(9): p. 375-380.

63. Austin, D. E.; Ahrens, T. J.; Beauchamp, J. L., *Dustbuster: a compact impact-ionization time-of-flight mass spectrometer for in situ analysis of cosmic dust.* Review of Scientific Instruments, 2002. **73**(1): p. 185-189.

Chapter 5

Hypervelocity Impacts of Macroscopic Bodies

5.1 Asteroid impacts on the Earth

Although the Earth is constantly bombarded with small meteorites and micrometeorites, large impacts are (thankfully) infrequent. Still, such impacts have taken place on several occasions [1]. One major impact occurred 65 million years ago at the Cretaceous-Tertiary (K-T) Boundary [2]. The fossil record of this time shows an extinction of more than half the marine and land biota, including dinosaurs, marine and flying reptiles, and numerous microscopic genera. It is believed that this mass extinction was caused by the impact of an asteroid on the Yucatan Peninsula, Mexico, known as the Chicxulub impact event [3].

The Chicxulub asteroid was approximately 10 km in diameter and impacted at a velocity of roughly 20 km/s [4]. The resulting crater is buried, but has been estimated to span nearly 300 km [5]. The geology of this region consists of a 3 km thick calcium carbonate layer containing significant calcium sulfate in the form of gypsum and anhydrite [6].

Several reasons have been put forward to explain the mass extinction associated with the Chicxulub impact. First, the ejected dust may have reduced the levels of sunlight reaching the Earth to such an extent that photosynthesis halted for a period of time [2]. Second, carbon dioxide released from carbonates upon impact may have caused global warming [1]. Third, acid rain may have resulted from the production of nitric acid as the atmosphere was heated during impact [7]. Finally, the release into the atmosphere of sulfur oxides, SO_2 and/or SO_3, from gypsum and anhydrite during impact may have caused global cooling or acid rain [3]. All of these events may have caused significant global changes and the extinction of many species.

The sulfur oxide scenario has been the subject of much interest. The amount of sulfur-bearing gas evolved during the Chicxulub impact has been estimated to be between 5×10^{16} g and 5×10^{18} g [4]. Two reaction mechanisms have been proposed [8, 9] for the shock-induced conversion from calcium sulfate to sulfur oxides in a Chicxulub-type impact:

$$2CaSO_4 \rightarrow 2CaO + 2SO_2 + O_2 \quad (1)$$

$$CaSO_4 \rightarrow CaO + SO_3. \quad (2)$$

Note that the sulfur oxide product is different in each mechanism. Theoretical treatments and experimental results are inconclusive as to which mechanism predominates under Chicxulub-type impact conditions [9]. Models to predict the consequences of sulfur oxides on the K-T extinction are complicated not only by large uncertainties in the vaporization mechanism (and hence, the species of sulfur oxide produced), but also by large uncertainties in the quantities of vapor released in the impact. As such it is not possible to say with reasonable certainty whether or not the

evolution of sulfur oxides was a major contributing factor in the K-T extinction. The importance of evolved carbon dioxide is similarly uncertain [6].

5.2 Description of mass spectrometer to study shock-induced vaporization and ionization of minerals

In order to characterize the chemical mechanisms involved in impact-vaporization of sulfur-bearing minerals, I designed a time-of-flight mass spectrometer capable of detecting vapor produced at the surface of a shocked mineral sample. This instrument will be used to study the relationship between impact parameters and the resulting sulfur oxides, providing critical experimental evidence for the role of sulfur oxides in the global climate change and mass extinction at the K-T Boundary.

In designing a mass spectrometer for analysis of shock-induced vapor, several points were given consideration. First of all, impacts would be generated using a fast projectile, which would likely disrupt the mass spectrometer vacuum system. A projectile would break vacuum, crush electrostatic grids, and short the electrical systems responsible for ion extraction and focusing. The mass spectrometer must be designed in such a way that the vaporized materials would be ionized, extracted, and analyzed faster than the projectile or atmospheric gases could interfere.

Another consideration was the ionization method. Some molecules would be ionized during the impact process itself. These could be extracted and analyzed as is. Other molecules would be evolved as neutrals, and would need to be ionized prior to extraction and analysis. In distinguishing between evolved SO_3 and SO_2 it was

necessary to take every precaution to avoid fragmentation during ionization. In addition, quantitative analysis required a method for which ionization cross-sections would be similar for all species of interest. Electron impact ionization was chosen over multiphoton ionization for this purpose.

Given the uncertainties in the duration of impact vaporization, two methods of ion extraction are possible. The ionizing electron beam could be pulsed; however, there is some uncertainty in the timing of the pulse relative to vapor formation. The other option is to use a continuous electron beam and subsequently pulse the ion extraction field. Although both options are viable, it was decided to use pulsed orthogonal extraction to sample ions. Ions then travel through a drift tube and an optional reflectron and are analyzed using a continuous dynode detector.

Figure 5.1 shows the experimental setup for these studies. Figure 5.2 shows an enlargement of the mass spectrometer section of the experimental setup. Figure 5.3 shows details of the electrodes and grids used to produce and extract ions. A projectile is launched toward the mass spectrometer. The projectile strikes a driver plate, onto which the mineral sample is mounted. As the shock wave travels through the mineral and reaches the free surface, vapor and ions are produced. One or more skimmers and apertures reduce the quantity of ejecta produced, according to the limitations of the ion optics and the ion detector. The attenuation of the electron beam, as measured by the faraday cup, will indicate the quantity of neutrals remaining. For studies of neutral species, ions formed by the shock wave are repelled by biasing the skimmers and/or apertures with +400 V. For studies of ions produced by the shock wave, the electron

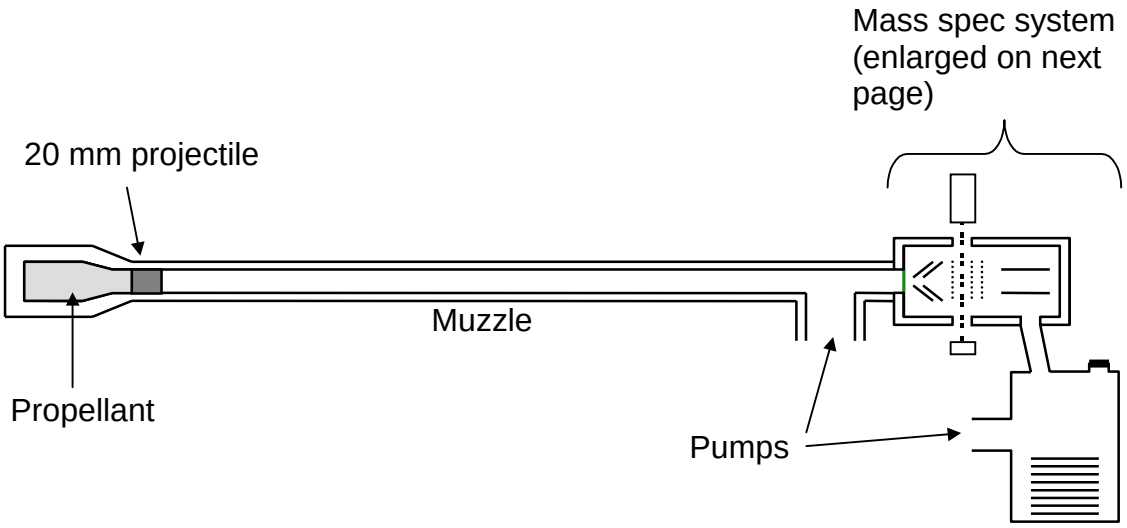

Figure 5.1. Experimental setup for shock-induced vaporization mass spectrometry experiments. Projectiles are fired from a hypervelocity gun. Other projectile sources can also be used. The projectile impacts a driver plate, which transmits a shock wave to a mineral sample mounted inside the time-of-flight orthogonal extraction reflectron mass spectrometer. Vapor molecules are ionized using an electron gun, then extracted and analyzed. Although vacuum is compromised, ions are extracted fast enough to prevent interference. The next page shows an enlargement of the mass spectrometer region.

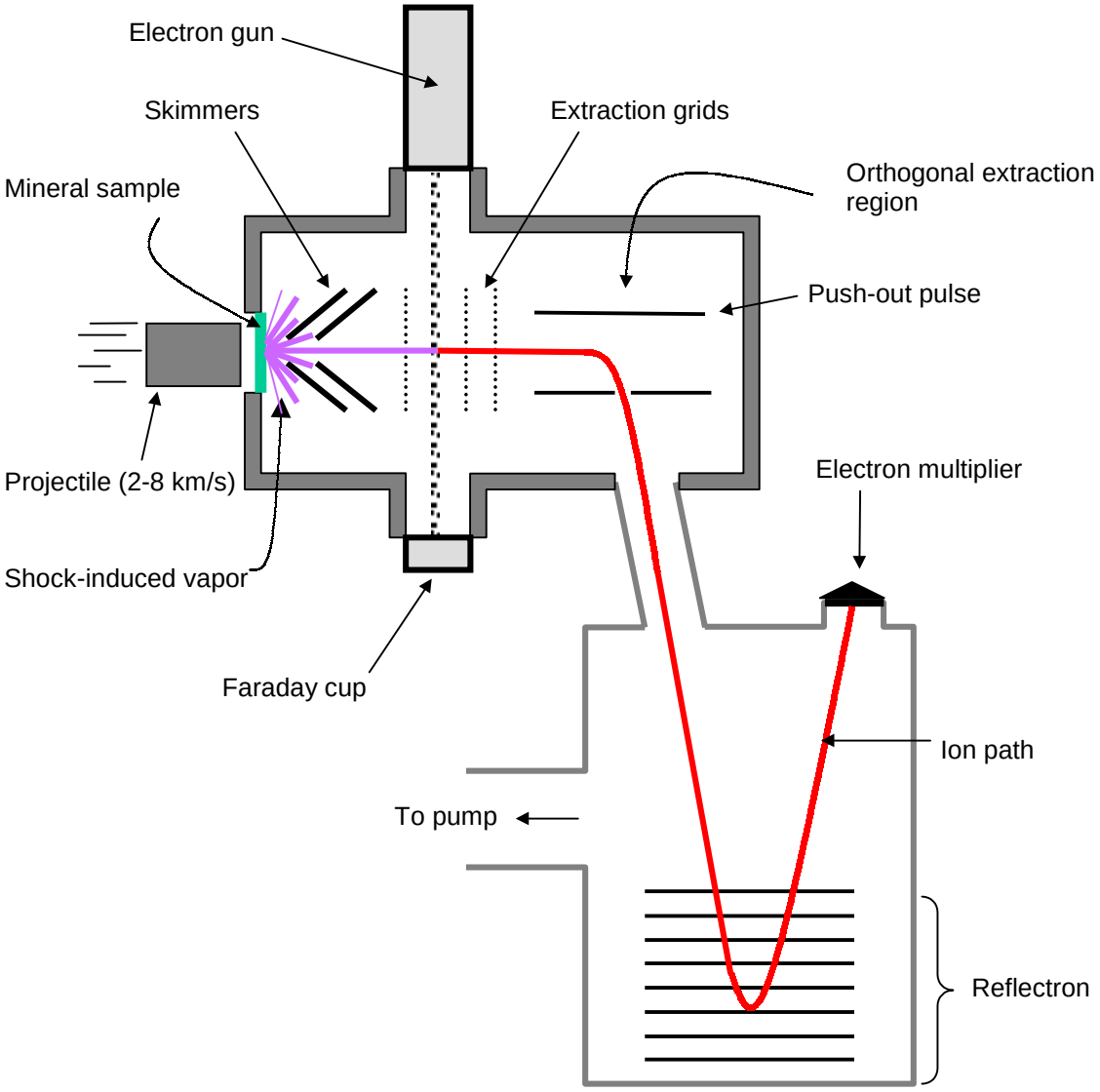

Figure 5.2. Details of the mass spectrometer system. Impact of the projectile on the mineral produces both ions and neutrals. Skimmers reduce the neutral density to an appropriate amount for electron impact ionization. Ions are collimated when they enter the pulsed extraction region. Lenses between the electron beam and the pulsed extraction region allow control over energy profile. Ions are pulsed into the reflectron chamber, where they are analyzed by an electron multiplier.

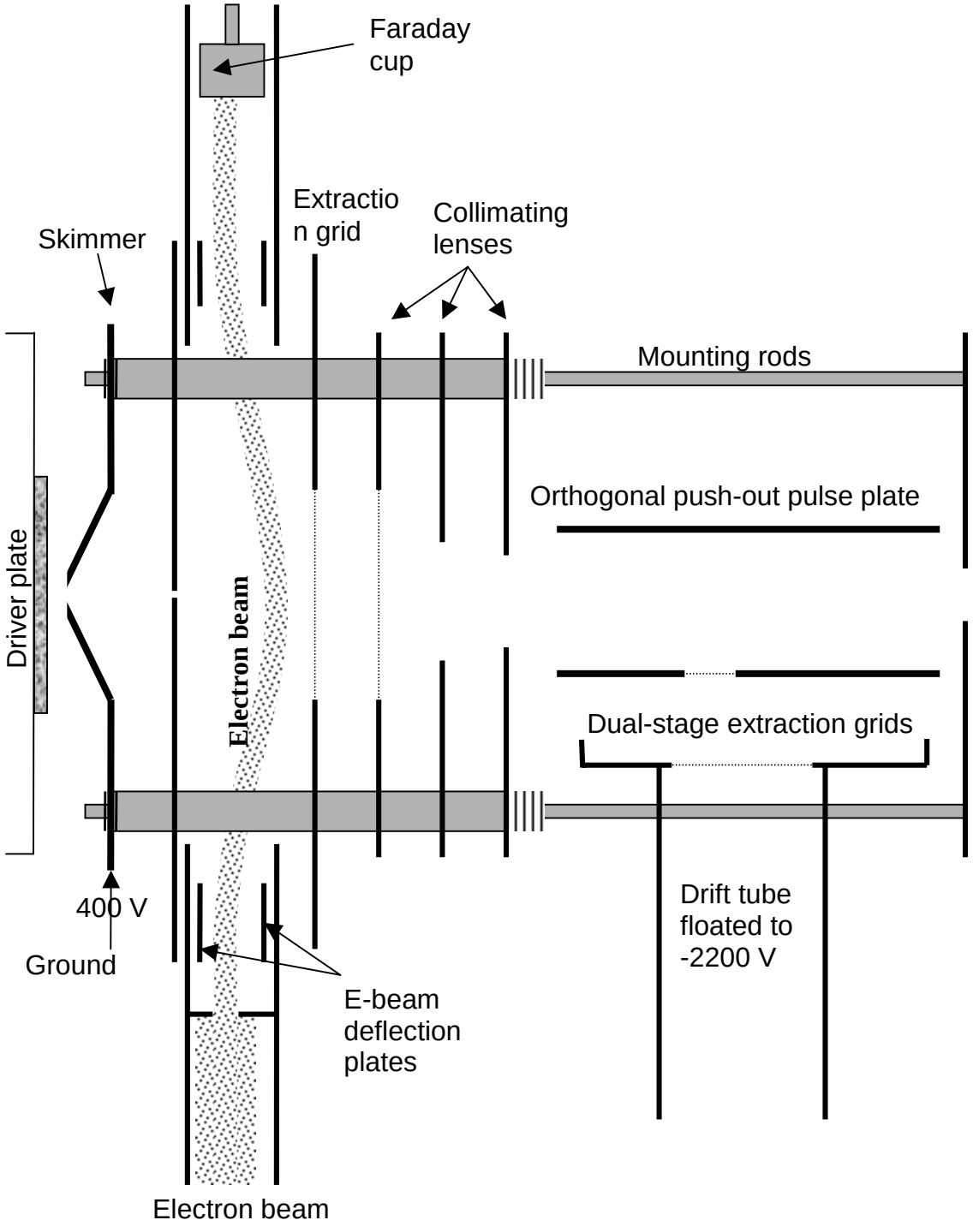

Figure 5.3. Electrodes and lenses involved in ion formation and extraction.

beam is simply turned off and the skimmer voltages are biased according to the ions being studied (negative to extract positive ions, positive to extract negative ions).

Neutral species are ionized by the electron beam, which is placed as close as practical to the mineral sample. The resulting ions are extracted by the voltage in the ionization region, and further extracted by the grid of the collimating lenses. Total ion energy at this point should be around 100-300 V. Although orthogonal extraction is typically performed using smaller voltages [10], ions in this experiment must be extracted and analyzed quickly to avoid contamination and destruction of the mass spectrometer by the projectile. For the experiment originally envisioned (20 mm projectile at several km/s), the projectile continues its forward motion after impact with the driver plate. If vacuum breaks, the inrush of atmospheric gases poses significant problems, but not for a few microseconds. In addition, as the projectile continues to move forward, electrostatic lenses, skimmers, and other components will be destroyed. The ion extraction technique presented here will be faster than these interferences. Of course, non-projectile methods of producing shock waves in minerals can be used with smaller extraction voltages, and with much fewer complications.

Mass resolution in an orthogonal extraction instrument is dependent on the degree of collimation of the ion trajectories as they travel through the orthogonal extraction region (before the push-out pulse) [11]. Collimating lenses are used for this purpose. When ions reach the extraction region, a pulse is applied to push the ions into the drift tube. Dual stage extraction at this point serves to compensate for the spread in the ion beam in the orthogonal extraction region. Ions travel through the drift tube to the

detector. A reflectron may be needed to achieve high mass resolution, but might not be needed for lower resolution experiments.

Orthogonal extraction is used only with continuous ion sources, or at least with ion sources that vary in time in a predictable way. In this case, the vapor produced at the mineral surface certainly has a strong time-dependence. Ions are formed as they reach the electron beam. However, the time history of vapor formation, the distribution of initial kinetic energies of vapor molecules, and the velocities of ions with different m/z will all affect the time-dependent homogeneity of the ions in the orthogonal extraction region. This must be taken into account when analyzing the data. It may be possible to probe the time dependence of mineral vaporization using repeated experiments. Quantitative analysis of speciation must take this factor into account. For instance, say species X is produced immediately upon impact, while an equal quantity of species Y is produced a short time later. If the orthogonal extraction pulse takes place early, more of species X is observed. If the pulse is later, species Y appears to be dominant. Studying the results from several pulse delays will give the time history of X versus Y, but a single spectrum will be misleading with respect to the total amount of each that was originally formed. Similarly, species X and species Y may be formed at the same time and with the same kinetic energy, but if species X is lighter than species Y, it will arrive in the orthogonal extraction region first. This mass effect can be taken into account only if many spectra are taken using several different pulse delay times.

Although shocked mineral experiments have not yet begun, assembly of the mass spectrometer is nearing completion. Initial experiments will use small detonation-type devices to produce the shock wave in various mineral samples. Although the

corresponding impact velocities are slow, detonation-type shocks allow repeated measurements on the same sample. Projectiles from a light gas may be used in further experiments when the required impact velocities are larger.

5.3 References

1. Kring, D. A. *Comparing the environmental consequences of impact events during the archean, proterozoic, and phanerozoic, Abstract 1511*. in *Lunar and Planetary Science XXXIII*. 2002. Houston, TX: Lunar and Planetary Institute.
2. Alvarez, L. W.; Alvarez, W.; Asaro, F.; Michel, H. V., *Extraterrestrial cause for the Cretaceous-Tertiary extinction.* Science, 1980. **208**: p. 1097-1107.
3. Gupta, S. C.; Ahrens, T. J.; Yang, W., *Shock-induced vaporization of anhydrite and global cooling from the K/T impact.* Earth and Planetary Science Letters, 2001. **188**: p. 399-412.
4. Ahrens, T. J.; Lyons, J. R.; Yang, W.; O'Keefe, D. O., *Global effects of the impcat of the Cretaceous-Tertiary extinction bolide.* Meteoritics and Planetray Science, 1997. **32**: p. A5.
5. Sharpton, V. L.; Burke, K.; Camrarge-Zanoguera, A.; Hall, S. A.; Lee, D. S.; Marin, L. E.; Suarez-Reynoso, G.; Quezada-Muneton, J. M.; Spudis, P. D.; Urrutia-Fucugauchi, J., *Chicxulub multi-ring impact basin--size and other characteristics derived from gravity analysis.* Science, 1993. **261**: p. 1564-1567.
6. Pierazzo, E. and Hahmann, A. N. *Chicxulub and climate: investigating the climate sensitivity to stratospheric injections of impact-generated S-bearing gases, Abstract 1269*. in *Lunar and Planetary Science XXXIII*. 2002. Houston, TX: Lunar and Planetary Institute.
7. Prinn, R. G. and Fegley, B. J., *Bolide impacts, acid rain, and biospheric traumas at the Cretaceous-Tertiary boundary.* Earth and Planetary Science Letters, 1987. **83**: p. 1-15.

8. Chen, G.; Tyburczy, J. A.; Ahrens, T. J., *Shock-induced devolatilization of calcium sulfate and implications for K-T extinctions.* Earth and Planetary Science Letters, 1994. **128**: p. 615-628.

9. Yang, W. and Ahrens, T. J., *Shock vaporization of anhydrite and global effects of the K/T bolide.* Earth and Planetary Science Letters, 1998. **156**: p. 125-140.

10. Dawson, J. H. J. and Guilhaus, M., *Orthogonal-acceleration time-of-flight mass spectrometer.* Rapid Communications in Mass Spectrometry, 1989. **3**(5): p. 155-159.

11. Guilhaus, M.; Selby, D.; Mlynski, V., *Orthogonal acceleration time-of-flight mass spectrometry.* Mass Spectrometry Reviews, 2000. **19**: p. 65-107.

Appendices

Appendix A

Isotopes of Selected Elements

Table A.1, on the next two pages, lists all stable, naturally occurring isotopes of elements observed in the various spectra shown or discussed in this thesis. Elements are listed in order of increasing mass. Naturally occurring radioactive nuclides, such as ^{40}K and ^{180}Ta, generally have very small natural abundances, and were not included in this table. The information in this table is taken from *Nuclides and Isotopes, Fifteenth Edition*, General Electric Nuclear Energy, 1996.

Element	Nuclide	Atomic mass, amu	Natural abundance, %
Hydrogen	^{1}H	1.0078	99.985
	^{2}H	2.0141	0.015
Lithium	^{6}Li	6.0151	7.5
	^{7}Li	7.0160	92.5
Carbon	^{12}C	12.000	98.90
	^{13}C	13.003	1.10
Oxygen	^{16}O	15.995	99.76
	^{17}O	16.999	0.04
	^{18}O	17.999	0.20
Sodium	^{23}Na	22.990	100.00
Magnesium	^{24}Mg	23.985	78.99
	^{25}Mg	24.986	10.00
	^{26}Mg	25.983	11.01
Aluminum	^{27}Al	26.982	100.00
Silicon	^{28}Si	27.977	92.23
	^{29}Si	28.976	4.67
	^{30}Si	29.974	3.10
Sulfur	^{32}S	31.972	95.02
	^{33}S	32.971	0.75
	^{34}S	33.968	4.21
	^{36}S	35.967	0.02
Potassium	^{39}K	38.964	93.26
	^{41}K	40.962	6.73

Table A.1. Natural abundances and masses of stable isotopes of selected elements.

Element	Nuclide	Atomic mass, amu	Natural abundance, %
Calcium	^{40}Ca	39.963	96.94
	^{42}Ca	41.959	0.647
	^{43}Ca	42.959	0.135
	^{44}Ca	43.955	2.086
	^{46}Ca	45.954	0.004
	^{48}Ca	47.953	0.187
Chromium	^{50}Cr	49.946	4.35
	^{52}Cr	51.941	83.79
	^{53}Cr	52.941	9.50
	^{54}Cr	53.939	2.36
Iron	^{54}Fe	53.940	5.85
	^{56}Fe	55.935	91.75
	^{57}Fe	56.935	2.12
	^{58}Fe	57.933	0.28
Copper	^{63}Cu	62.930	69.17
	^{65}Cu	64.928	30.83
Molybdenum	^{92}Mo	91.907	14.84
	^{94}Mo	93.905	9.25
	^{95}Mo	94.906	15.92
	^{96}Mo	95.905	16.68
	^{97}Mo	96.906	9.55
	^{98}Mo	97.905	24.13
	^{100}Mo	99.907	9.63
Tantalum	^{181}Ta	180.948	99.988

Table A.1, continued. Natural abundances and masses of stable isotopes of selected elements.

Appendix B

Ion Definitions Used in Simulations

SIMION ion trajectory software, versions 6.0 and 7.0 (by David A. Dahl, Idaho National Engineering and Environmental Laboratory, Idaho Falls, 83415), were used extensively both in testing possible designs and in evaluating the working design. In order to make full use of SIMION's ion definition capabilities, I wrote a spreadsheet to estimate the properties of positive ions emerging from an impact-generated plasma. The ion properties generated using the spreadsheet were loaded into SIMION and used for various simulations. This appendix contains the details of the spreadsheet. It is hoped that it may be useful for anyone trying to run similar impact-ionization simulations.

SIMION requires ion definition files to be of the following ASCII format, in which each line represents an individual ion:

TOB, MASS, CHARGE, X, Y, Z, AZ, EL, KE, CWF, COLOR

TOB is the ion's time-of-birth. X, y, and z refer to the coordinates at which the ion originates. AZ and EL are the azimuth and elevation angles, respectively, along which the ions are initially moving with an initial kinetic energy, KE. Figure B.1 shows the coordinate system in which ions are defined. CWF is the charge-weighing factor, which is used in certain ion-ion repulsion calculations (default 1), and color is the color with which the ion appears on the screen.

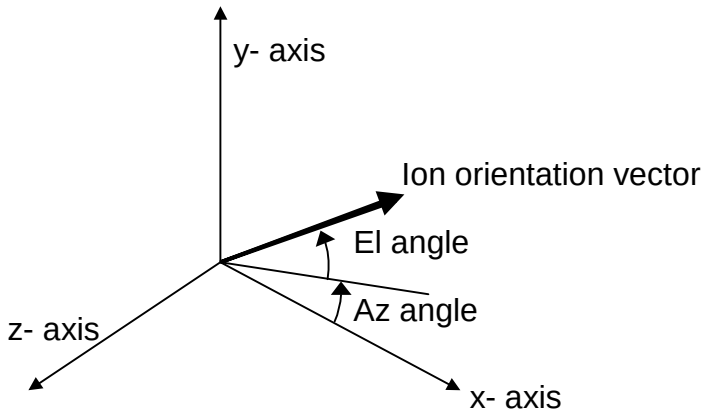

Figure B.1. Coordinate system and angular orientations of ions used in SIMION. Azimuthal angle lies along the xz plane, in the negative z direction. Elevation angle is in the direction of y.

Below is a section from the first page of the spreadsheet. This ion definition spreadsheet produces a file of ion definitions with the following properties. First, the initial kinetic energies of ions are a Gaussian-random distribution about a specified mean, with a specified standard deviation. Second, the spatial distribution of the ions can be specified as either isotropic, *cos* θ, or cos^2 θ about the normal to the target plate. Ions can originate at the same point, at varying points, or from a small distribution of points about some location. Although time-of-birth and CWF could be modified, I never needed to do so. Mass and charge are easily specified as needed for each simulation. Values in the first six columns are input directly. The values of Az, El, and KE for each ion were calculated using the process described in the following pages.

Ion definition template Page 1

Gaussian Distribution
ions come off of plate in y-z plane, directed right, parallel to x-axis

average energy 40 eV 39.72 actual energy average
stdev 25 eV 25.00 actual energy stdev

			initial ion location			off of x along z	off of x-z along y			
TOB	mass	charge	x	y	z	az	el	KE	CFW	color
0	56	1	5.001	0	0	3.532	-7.027	57.328	1	1
0	56	1	5.001	0	0	-67.596	-20.620	81.120	1	1
0	56	1	5.001	0	0	1.397	-61.068	25.415	1	1
0	56	1	5.001	0	0	77.802	29.052	36.501	1	1
0	56	1	5.001	0	0	23.623	-9.895	29.929	1	1
0	56	1	5.001	0	0	17.240	7.263	9.368	1	1
0	56	1	5.001	0	0	-7.732	22.263	26.998	1	1
0	56	1	5.001	0	0	45.324	-6.879	43.903	1	1
0	56	1	5.001	0	0	33.316	9.824	60.822	1	1
0	56	1	5.001	0	0	-66.266	-42.192	36.443	1	1
0	56	1	5.001	0	0	35.487	51.647	72.173	1	1
0	56	1	5.001	0	0	-13.153	45.889	18.502	1	1
0	56	1	5.001	0	0	-53.510	-5.973	-8.664	1	1
0	56	1	5.001	0	0	-47.595	-30.520	66.578	1	1

Below is a section of the second page of the spreadsheet, in which a set of random values in a Gaussian distribution was generated. Each value in the leftmost column is the sum of 50 random numbers, each of which has an average value of zero. The average and standard deviation for the entire column of sums are calculated and displayed at the top of the page. The kinetic energy of the nth ion is determined by the formula:

$$KE_n = KE_0 + \left(\frac{\sigma_0}{\sigma_n}\right)(N_n), \qquad (1)$$

where KE_0 is average kinetic energy specified on the first page, σ_0 is the specified standard deviation from the first page, σ_n is the standard deviation of the random sums from the second page, and N_n is the nth random sum on the second page.

Gaussian distribution generator				Page 2. Uses sum of 50 randomly-generated numbers to give a random normal distribution				
average	0.0406							
stdev	1.8012							
	1	2	3	4	5	6	7	8
-1.741	-0.378	-0.25	0.0034	0.1944	-0.072	0.177	-0.269	-0.052
2.331	0.0863	0.1353	-0.028	0.3569	0.394	0.3474	0.0121	0.2424
1.159	-0.441	0.4716	0.2117	-0.062	0.0559	0.3325	-0.49	0.0371
-0.518	0.2131	0.473	0.0592	0.1735	0.1904	-0.382	-0.464	-0.25
-3.383	0.3217	-0.32	-0.415	0.0408	-0.293	-0.189	-0.307	0.1735
-1.132	-0.439	-0.289	-0.046	-0.367	0.2571	-0.172	0.2115	-0.078
-1.533	-0.364	0.1838	-0.047	-0.287	0.481	-0.095	0.2088	0.3166
1.527	0.3773	-0.173	-0.33	-0.467	0.4798	0.4888	-0.286	-0.344
-0.412	0.3966	0.4396	-0.065	0.1112	0.0811	-0.044	-0.205	-0.295
2.833	0.0981	0.221	-0.047	-0.154	0.4053	0.0631	0.1409	0.2108
-3.165	0.3621	-0.039	-0.458	0.1486	0.2067	-0.498	-0.187	-0.037

Below is a sample from page three of the spreadsheet. This page generates the x-, y-, and z-directional components with which the azimuth and elevation angles of each ion are calculated. In the first three columns, three random numbers define a directional vector. R is the magnitude of this vector. In the next column, vectors which fall inside a positive-x hemisphere with radius 0.5 are assigned a value of 1 (eventually retained). Vectors outside this hemisphere are assigned a value of zero, and will not be used. Zero-sets are deleted, and the remaining coordinates are randomly sorted and tabulated. The az and el values for defined ions are then

$$\mathrm{Az}_n = \tan^{-1}\left(\frac{z_n}{x_n}\right) \tag{2}$$

$$\mathrm{El}_n = \tan^{-1}\left(\frac{y_n}{\sqrt{x_n^2 + z_n^2}}\right). \tag{3}$$

The resulting angles are converted from radians into degrees, which are the units used by SIMION.

isotropic distribution								Page 3 isotropic distribution		
				sphere						
rand x	rand y	rand z	R	R<0.5	x	y	z	x	y	z
0.388	0.291	-0.097	0.494	1	0.3878	0.2909	-0.097	0.0602	-0.284	-0.062
0.061	0.080	0.414	0.426	1	0.0612	0.0801	0.4137	0.2014	0.2275	-0.08
0.278	-0.387	0.420	0.635	0	0	0	0	0.2868	0.3441	-0.181
0.428	-0.204	0.048	0.477	1	0.4281	-0.204	0.0477	0.0368	0.1188	0.2317
0.138	-0.224	-0.370	0.455	1	0.1385	-0.224	-0.37	0.3012	0.1318	0.0102
0.327	0.157	0.210	0.419	1	0.3272	0.1574	0.2095	0.091	0.0955	0.2684
0.400	-0.378	-0.191	0.582	0	0	0	0	0.2717	-0.26	0.0394
0.397	0.432	0.305	0.662	0	0	0	0	0.4287	-0.162	0.1489
0.368	0.157	-0.376	0.549	0	0	0	0	0.2436	0.4002	0.0278
0.466	0.421	0.428	0.760	0	0	0	0	0.2838	0.2779	-0.022
0.169	0.115	0.443	0.488	1	0.1694	0.1148	0.4433	0.0661	-0.267	0.0205
0.342	0.052	-0.080	0.355	1	0.3423	0.0517	-0.08	0.0139	-0.087	-0.288

Below is a sample from page four of the spreadsheet, which generates a cosine distribution of ions. X-, y-, and z-components are chosen randomly, similar to the isotropic distribution. Vectors outside of the r=0.5 hemisphere are excluded. The angle θ of each vector is calculated, and if the value of *cos* θ is greater than a random number, the vector is rejected. Note that θ is being defined as the angle away from the normal (in this case, the positive x-axis), and is not the same as the Az or El angles used in the ion definition file. The calculation of the cos^2 θ distribution is similar, except that cos^2 θ is compared to the random number. The resulting list of vectors is sorted, zero values eliminated, and vectors are ordered randomly into the list used to calculate Az and El for the ions. The Az and El calculations are the same as for the isotropic distribution.

cosine distribution											Page 4
					sphere						
rand x	rand y	rand z	theta	R	R<0.5	prob	rand	P>rand	x	y	z
0.307	-0.018	0.081	15.2	0.32	1	0.965	0.317	1	0.3069	-0.018	0.0814
0.012	-0.034	-0.133	85.0	0.14	1	0.087	0.969	0	0	0	0
0.018	0.442	0.221	87.9	0.49	1	0.037	0.337	0	0	0	0
0.053	0.131	0.220	78.3	0.26	1	0.203	0.745	0	0	0	0
0.430	-0.189	0.427	47.3	0.63	0	0.678	0.429	1	0	0	0
0.487	0.338	-0.141	37.0	0.61	0	0.799	0.313	1	0	0	0
0.334	-0.062	-0.162	27.4	0.38	1	0.888	0.627	1	0.3344	-0.062	-0.162
0.143	0.067	-0.411	71.1	0.44	1	0.324	0.326	0	0	0	0
0.399	0.090	0.030	13.4	0.41	1	0.973	0.242	1	0.399	0.0904	0.0304
0.226	0.176	0.109	42.6	0.31	1	0.736	0.969	0	0	0	0
0.457	0.280	0.216	37.7	0.58	0	0.791	0.987	0	0	0	0
0.276	-0.215	0.193	46.3	0.40	1	0.691	0.078	1	0.2758	-0.215	0.1927
0.122	0.364	0.161	72.9	0.42	1	0.294	0.555	0	0	0	0

Figures B.2, B.3, and B.4 show typical populations of ions generated using the above method, and compare the angular (spatial) distributions to ideal isotropic, *cos* θ, and cos^2 θ distributions. For these plots, θ for each ion (from groups of 5000 ions) was calculated as the angle in degrees from the normal to the surface at which ions

originated. The number of ions with a given value of θ (rounded to the nearest integer) was then divided by *sin* θ to yield a surface density (effectively the density on the surface of a sphere to which the ion vectors had been projected) which was normalized. This normalized density as a function of θ is shown in the plots.

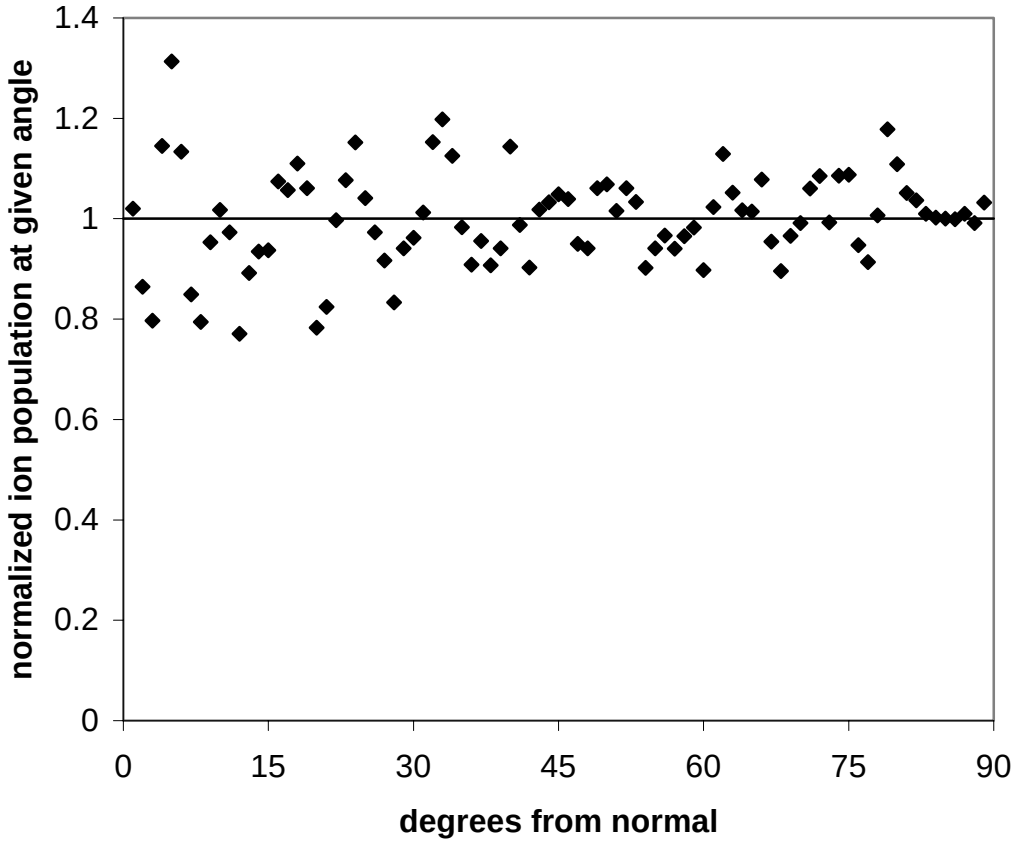

Figure B.2. Typical isotropic ion distribution as function of angle from normal.

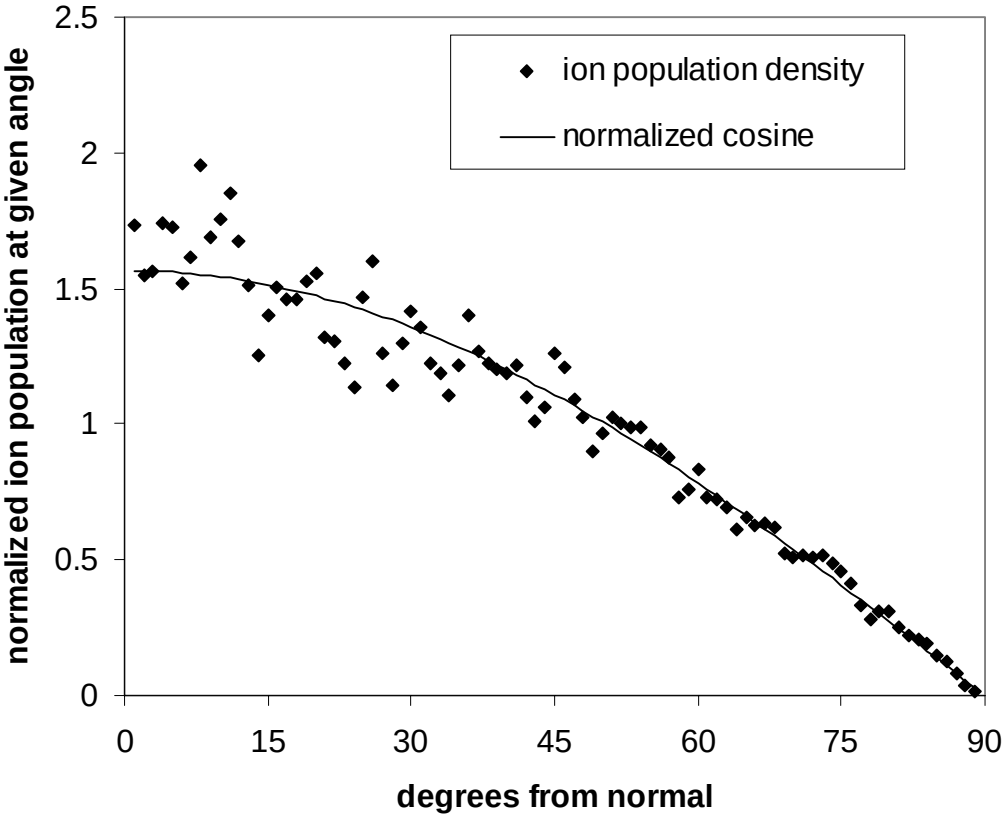

Figure B.3. Typical cosine ion distribution as function of angle from normal.

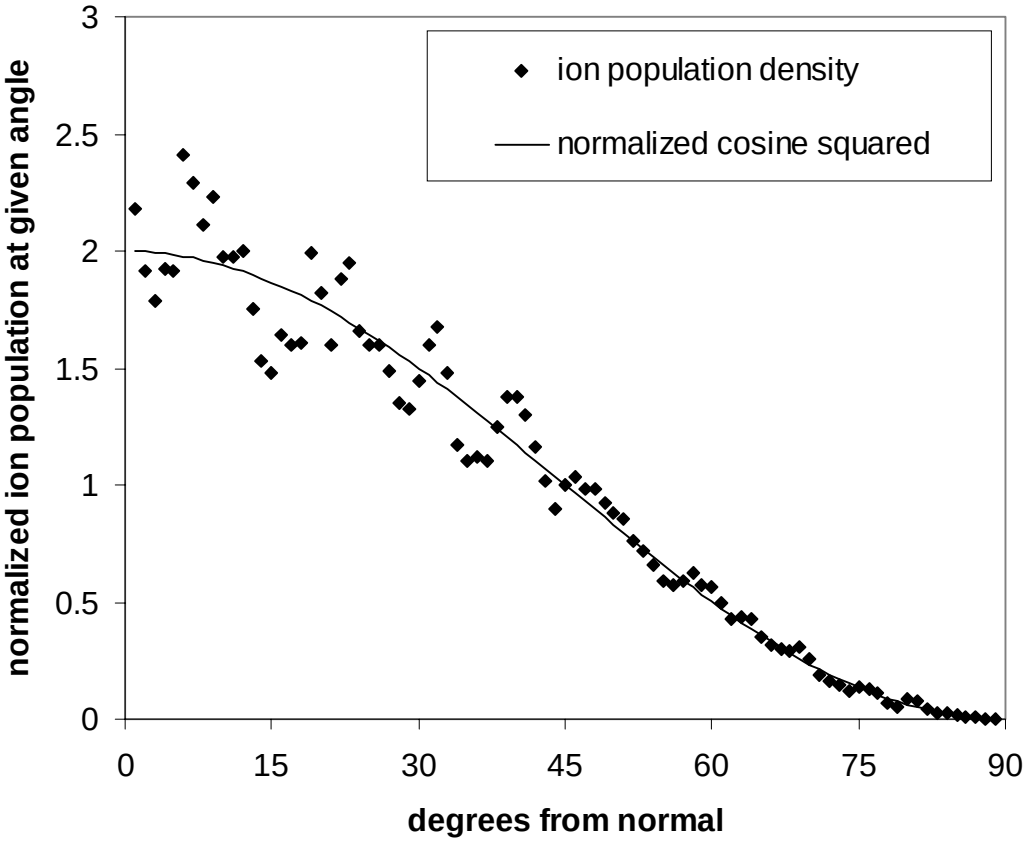

Figure B.4. Typical cosine-squared ion distribution as function of angle from normal.